Selective laser melting of Al-12Si

D I S S E R T A T I O N

zur Erlangung des akademischen Grades

Doktor - Ingenieur
(Dr.-Ing.)

vorgelegt

der Fakultät Maschinenwesen
der Technische Universität Dresden
von

Prashanth Konda Gokuldoss

geboren am 01 August 1985 in Chennai (Indien)

Gutachter: Prof. Jürgen Eckert

Prof. Nilay Krishna Mukhopadhyay

Eingereicht am:

Tag der Verteidigung:

Abstract

Selective laser melting (SLM) is a powder-based additive manufacturing technique consisting of the exact reproduction of a three dimensional computer model (generally a computer-aided design CAD file or a computer tomography CT scan) through an additive layer-by-layer strategy. Because of the high degree of freedom offered by the additive manufacturing, parts having almost any possible geometry can be produced by SLM. More specifically, with this process it is possible to build parts with extremely complex shapes and geometries that would otherwise be difficult or impossible to produce using conventional subtractive manufacturing processes.

Another major advantage of SLM compared to conventional techniques is the fast cooling rate during the process. This permits the production of bulk materials with very fine microstructures and improved mechanical properties or even bulk metallic glasses. In addition, this technology gives the opportunity to produce ready-to-use parts with minimized need for post-processing (only surface polishing might be required). Recently, significant research activity has been focused on SLM processing of different metallic materials, including steels, Ti-, Ni- and Al-based alloys. However, most of the research is devoted to the parameters optimization or to the feasibility studies on the production of complex structures with no detailed investigations of the structure-property correlation.

Accordingly, this thesis focuses on the production and structure-property correlation of Al-12Si samples produced by SLM from gas atomized powders. The microstructure of the as-prepared SLM sample consists of supersaturated primary Al with an extremely fine cellular structure along with the residual free Si situated at the cellular boundaries. This microstructure leads to a remarkable mechanical behavior: the yield and tensile strengths of the SLM as-prepared samples are respectively four and two times higher than their cast counterparts. However, the ductility is significantly reduced compared with the cast samples.

The effect of annealing at different temperatures on the microstructure and resulting mechanical properties of the SLM parts has been systematically studied by analyzing the

size, morphology and distribution of the phases. In addition, the mechanical properties of the SLM samples have been modeled using micro- structural features, such as the crystallite and matrix ligament sizes. The results demonstrate that the mechanical behavior of the Al-12Si SLM samples can be tuned within a wide range of strength and ductility through the use of the proper annealing treatment.

The Al-Si alloys are generally used as pistons or cylinder liners in automotive applications. This requires good wear resistance and sufficient strength at the operating temperature, which ranges between 373 and 473 K. Accordingly, the tensile properties of the SLM samples were also tested at these temperatures. Changing the hatch style during SLM processing varies the texture in the material. Hence, samples with different hatch styles were produced and the effect of texture on their mechanical behavior was evaluated. The results show that the hatch style strongly influences both the mechanical properties and the texture of the samples; however no direct correlation was observed between texture and mechanical properties.

The wear properties of the Al-12Si material were evaluated using pin-on-disc and fretting wear experiments. These experiments show that the as-prepared SLM samples exhibit better wear resistance than their cast counterparts and the SLM heat-treated samples. Finally, the corrosion investigations reveal that the SLM samples have similar corrosion behavior as the cast specimens under acidic conditions.

A major drawback for the wide application of SLM as an industrial processing route is the limited size of the products. This is a direct consequence of the limited dimensions of the available building chambers, which allow for the production of samples with volumes of about 0.02 m^3. A possible way to overcome this problem would be the use of the welding processes to join the small SLM objects to form parts with no dimensional limitations. In order to verify this possibility, friction welding was employed to join Al-12Si SLM parts. The results indicate that friction welding not only successfully permits to joining materials manufactured by SLM, but also helps to significantly improve their ductility.

Abstract

  This work clearly demonstrates that SLM can be successfully used for the production of Al-12Si parts with an overall superior performance of the mechanical and physical properties with respect to the conventional cast samples. Moreover, the mechanical properties of the SLM samples can be widely tuned *in-situ* by employing suitable hatch styles or *ex-situ* by the proper heat treatment. This might help the development of SLM for the production of innovative high-performance Al-based materials and structures with controlled properties for automotive and aerospace applications.

Kurzfassung

Selektives Laserstrahlschmelzen (SLM) ist ein pulverbasiertes additives Fertigungsverfahren. Dabei wird ein drei-dimensionales Computermodell, üblicherweise ein CAD (computer-aided design)-Modell oder eine CT (Computertomographie), durch eine additive Technik, also Schicht für Schicht, detailgetreu wiedergegeben. Aufgrund des hohen Freiheitsgrades, die dieses generative Fertigungsverfahren ermöglicht, können Bauteile nahezu jeder Geometrie mittels SLM hergestellt werden. Das schließt Bauteile mit extrem komplizierter Form und Geometrie ein, die sonst mittels konventionellen subtraktiven Fertigungsverfahren schwierig bzw. gar nicht herzustellen wären. Ein weiterer bedeutender Vorteil des SLM-Verfahrens liegt in den hohen Abkühlraten, die während des Aufschmelz – bzw. Abkühl-Prozesses erreicht werden. Dies erlaubt die Fertigung von Bauteilen mit sehr feinem Gefüge und verbesserten mechanischen Eigenschaften und ermöglicht sogar die Herstellung massiver metallischer Gläser. Ein weiterer Vorteil liegt im minimalen Bedarf an Nachbearbeitung der Bauteile, meist ist nur ein Glätten der Oberflächen erforderlich.

Im Fokus der Forschungsaktivitäten steht die Entwicklung von verschiedenen metallischen Materialien mittels SLM, einschließlich Stählen sowie Ti-, Ni- und Al-basierten Legierungen. Häufig dienen die Untersuchungen hauptsächlich der Parameteroptimierung oder der Fertigung von komplizierten Strukturen ohne umfassende Analysen der Gefüge-Eigenschafts-Beziehung einzubeziehen.

Demzufolge ist die Fertigung und Analyse der Struktur-Eigenschafts-Beziehung von Al-12Si-Proben, die mittels SLM aus gasatomisierten Pulver hergestellt wurden, Hauptbestandteil der vorliegenden Arbeit. Das Gefüge der mit SLM gefertigten Proben besteht aus übersättigtem primärem Al mit extrem feiner zellularer Struktur und Si, welches an den Korngrenzen der Al-Zellen angelagert ist. Dieses Gefüge führt zu einem außerordentlichen mechanischen Verhalten: die Fließ- und Bruchfestigkeit unter Zugbeanspruchung der SLM-Proben sind vier- bzw. zweimal höher im Vergleich zu gegossenen Proben der Legierung, während die Plastizität dagegen deutlich geringer ist. Die Auswirkung von Wärmebehandlungen bei verschiedenen Temperaturen auf das Gefüge der

SLM-Bauteile wurde systematisch hinsichtlich Größe, Morphologie und Verteilung der Phasen untersucht. Zusätzlich wurden die mechanischen Eigenschaften durch Veränderung von mikrostrukturellen Eigenschaften, wie die Kristallit- und Matrix-Ligamentgröße modelliert. Die Ergebnisse veranschaulichen, dass das mechanische Verhalten von Al-12Si SLM-Proben innerhalb eines breiten Festigkeits- und Plastizitätsbereiches mittels einer geeigneten Wärmebehandlung eingestellt werden kann.

Al-Si-Legierungen werden unter anderem als Kolben und Zylinderbuchsen für automobiltechnische Anwendungen verwendet. Dies erfordert eine gute Verschleißfestigkeit und ausreichende Festigkeit bei Betriebstemperaturen von 373 K bis 473 K. Folglich wurden auch die Zugeigenschaften der SLM-Proben in diesem Temperaturbereich untersucht. Durch Veränderung des hatch-style während des SLM-Vorgangs lässt sich die Textur im Material variieren. Deswegen wurden Proben mit unteschiedlichem hatch-style hergestellt und die Auswirkung der Textur auf die mechanischen Eigenschaften bewertet. Die Ergebnisse veranschaulichen, dass das hatch style die Probentextur sowie die mechanischen Eigenschaften deutlich beeinflußt; allerdings wurde kein direkter Zusammenhang zwischen Textur und mechanischen Eigenschaften beobachtet. Die Verschleißeigenschaften des Al-12Si-Materials wurden anhand von Stift-Scheibe- und Frettingverschleißversuchen beurteilt. Diese Experimente zeigen, dass die mittels SLM hergestellten Proben einen besseren Verschleißwiderstand besitzen als die gegossenen sowie die wärmebehandelten SLM-Proben. Korrosionsuntersuchungen ergaben, dass die SLM-Proben das gleiche korrosive Verhalten unter sauren Bedingungen aufweisen wie die gegossenen Proben.

Ein gewisser Nachteil für die breite Anwendung des SLM als industrielles Fertigungsverfahren ist dessen Limitation hinsichtlich Bauteilgröße. Dies folgt direkt aus der Größe der verfügbaren „Baukammer", die eine Herstellung von Proben mit Volumen von ungefähr 0.02 m^3 ermöglicht. Eine erfolgversprechende Methode zur Überwindung dieses Problems, könnte der Einsatz von Schweißprozessen zur Verbindung der kleinen SLM-Elemente sein, sodass auch größere Bauteile produziert werden könnten. Deshalb wurde die Technologie des Reibschweißens zur Verbindung der Al-12Si SLM-Proben geprüft. Die Ergebnisse zeigen, dass Reibschweißen nicht nur das erfolgreiche Fügen von Materialien, die

mit SLM hergestellt wurden, ermöglicht, sondern gleichzeitig auch deren Plastizität signifikant verbessert.

Diese Arbeit erbringt den Nachweis, dass das SLM erfolgreich für die Herstellung von Al-12Si-Bauteilen eingesetzt werden kann. Die SLM-Bauteile besitzen, verglichen mit den auf konventionelle Weise gegossenen Proben, insgesamt bessere mechanische sowie physikalische Eigenschaften. Darüber hinaus können die mechanischen Eigenschaften der SLM-Proben in einem weiten Bereich in-situ eingestellt werden, indem geeignete Parameterkombinationen angewendet werden oder ex-situ passende Wärmebehandlungen durchgeführt werden. Diese Ergebnisse bringen die Entwicklung des SLM für die Produktion von innovativen Al-basierten Hochleistungsmaterialien und Strukturen mit kontrollierten Eigenschaften für Fahrzeug- und Luftfahrtanwendungen voran.

Contents

Contents

List of figures

List of tables

Chapter 1: Introduction

1.1 Motivation

One of the most important economic sectors by revenue is the automotive industry. The focus of the automotive industry currently lies in reducing the weight of the automotive components. Weight reduction leads to several advantages like reduction in fuel consumption and carbon dioxide emission, minimization of the wear of brakes, tire etc. ([Imm95], [Col95], [Pow13a]). Even a modest weight reduction of 50 kg reduces the CO_2 emission up to 5 g/km and decreases the fuel usage by up to 2 % [Pow13a]. Taking the mass production into account, a weight reduction of ~ 10 kg for each of the 70 million lightweight engines produced in 2011 in the United States, could save 908 million liters of refined fuel or 9 million barrels of crude fuel [Pow13a]. Similarly, eliminating ~ 6 kg in the automotive transmission would save up to 350 million liters of refined fuel ([Pow13a], [Dup13a]), suggesting that *less is more* for high performance materials in the automotive sector. One of the examples for light weight construction is shown in Fig. 1.1.1, where the skeleton of the car body is made of lightweight Al-based alloys rather than conventional steels.

Fig. 1.1.1. Structure of a car, where the skeleton is made of Al-based alloys [NYT12a].

The weight reduction in the engineering components can be achieved by the usage of light metals and/or by creating lightweight structures, like cellular or octahedral structures, made of conventional high-density materials like steel. Steel is the most commonly used metal in the automobile sector [Fle13a]. Innovations in the steel industry has led to a new variety of steel called ultra-high strength steel, which can considerably reduce the weight of the components by ~ 8% without affecting the overall cost of the components [Fle13a]. This is a significant step forward in the field of steel manufacturing; however, additional gains can be attained by further reduction of weight the components.

Aluminum and other lightweight materials make in-roads in the field of lightweight manufacturing and can be processed by any conventional methods such as casting, powder metallurgy etc. [Fle13a]. The automobile giant AUDI started revolutionizing the modern lightweight materials and the industry with the Audi A8 and its Audi Space Frame (ASF) in 1994. The A8's ASF weighed a mere 249 kg that reduces the mass of the car by 200 kg, when built of steel [Fle13a]. From an average of 39 kg of Al and its alloys used in the passenger cars in 1976, the usage of Al has increased gradually to 110 kg in 1996 and is expected to grow further to 250 – 350 kg by 2015 [Mil00a].

Lightweight metal-structures possess low density, high specific compression strength, good absorption of energy, good acoustic properties etc. [Dot08a]. Owing to such superior properties, these structures find their applications in aerospace and automotive industry, reconstructive surgery, chemical industry, structural construction etc. [Löb11a]. Cellular metal structures can be produced by suitable foaming processes ([Yad09a], [Ash01a]) depending on the size and topology of the pores to be produced. However, the periodic structures, such as lattice structures or honey combs, are difficult to produce by the available conventional manufacturing processes and hence there is a need of novel processing techniques.

1.2 Aim and objectives

Additive manufacturing, such as selective laser melting (SLM), is one of the options that can be used to process light metals and lightweight metal-structures. Selective laser

melting is capable of producing parts with intricate geometries and superior properties ([ENE13a], [Pra13a]). Moreover, it has been reported that additive manufacturing through SLM can help in achieving significant reduction of the energy and materials usage ([DOE12a], [ENE13a]). In addition, application-oriented research like production by SLM of complex parts for biomedical and other industrial applications ([Löb11a], [Mul08a], [Pat09a], [Wan13a]) has also been of significant attention (Fig. 1.2.1). Unfortunately, the majority of the research is focused on the optimization of the SLM processing parameters through single tracks and density optimization through small cubical samples and only a few investigations have analyzed the metallurgical aspects of the parts produced by selective laser melting. The present research work deals extensively with the microstructural features of the parts produced by selective laser melting with the ultimate goal to correlate the properties of the samples with their metallurgical aspects.

Fig. 1.2.1. A titanium prosthetic hand produced via additive manufacturing process at the Oak Ridge National Laboratory ([DOE12a], [ENE13a]).

The specific objectives of this thesis are:

(1) Production of Al-12Si samples by selective laser melting and their complete microstructural characterization.
(2) Evaluation of the mechanical, tribological and corrosion properties of the as-prepared SLM Al-12Si parts and analysis of the microstructure-properties correlations.

(3) Comparison of the properties of the SLM Al-12Si samples with the corresponding material produced by conventional casting.

(4) Analysis of the effect of heat-treatment on mechanical, tribological and corrosion properties of the SLM Al-12Si specimens.

(5) Test of the welding properties of the SLM parts.

1.3 Structure of the thesis

A detailed theoretical background is presented in Chapter 2, describing the different types of manufacturing processes with focus on the additive manufacturing technology and selective laser melting. Details on the powder properties required for selective laser melting, the processing parameters and the potential applications of SLM are discussed along with the different systems already processed by selective laser melting. In addition, the fundamental aspects of solidification are presented. The final part of Chapter 2 is devoted to Al-based alloys with main focus on the Al-Si system. A brief summary of the experimental procedures used in the present thesis is given in Chapter 3, including the details on the processing routes and characterization techniques.

Chapter 4 includes a detailed investigation on the microstructural features of the SLM parts, the effect of texture and heat-treatment, strength modeling and high temperature tensile properties along with the effect of the hatch style on texture and mechanical properties. Chapter 5 reports the tribological and corrosion properties of the SLM samples. Chapter 6 deals with the joining of parts produced by selective laser melting using friction welding, which will help to widen the application spectrum of selective laser melting. Finally, the summary and conclusions are presented in Chapter 7.

Chapter 2: Theoretical background

The present chapter provides the theoretical background necessary for understanding the work performed in this thesis. This chapter starts with describing the various types of manufacturing processes and their advantages, followed by a detailed discussion on additive manufacturing and its potential applications. A detailed insight on the SLM process is presented along with the discussion on the important processing parameters. Advantages and potential applications offered by the SLM process are also discussed. The chapter also describes the fundamentals of solidification with focus on the equilibrium partition coefficient, solute redistribution, the different solidification modes, constitutional supercooling theory and finally the influence of cooling rate on the solidifying microstructure. A section of this chapter describes the different materials used in the SLM process and the last part discusses the basics about the need of aluminum alloys, their classification and the possible strengthening mechanisms.

2.1 Manufacturing processes
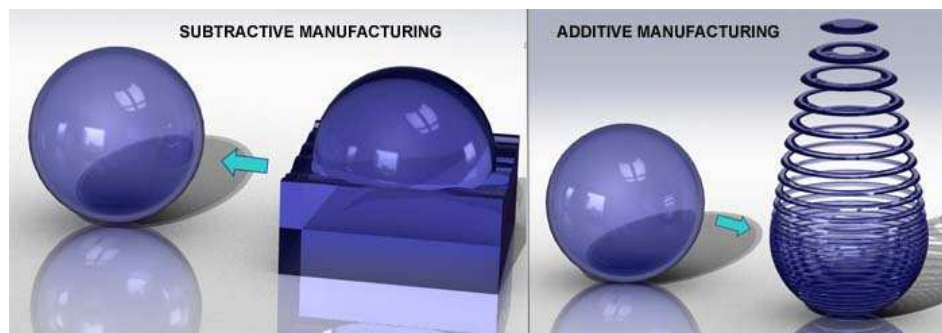
Fig. 2.1.1. Schematic illustration showing the differences between the subtractive and additive manufacturing [New11a].

The term manufacturing process is defined as the steps or the sequence of processes through which the raw materials are transformed into an industrially useful product of definite size and shape [Mac96a]. The process begins with the design aspects, followed by

the series of manufacturing processes, like solidification, consolidation, machining, heat treatment etc., and involves the tests and investigations necessary for quality assurance purposes. The manufacturing processes can be classified into two major categories (1) subtractive manufacturing (SM) and (2) additive manufacturing (AM) or solid free-form processing (SFF) [Gro07a]. A SM process can be described as a controlled way of removal of the undesired part or layer of material to form a product with the desired shape (Fig. 2.1.1). SM processing (e.g. cutting, machining, turning, drilling, reaming, tapping etc.) involves significant wastage of material and consequently it may lead to high production costs. In addition, the material wastage may further lead to environmental issues.

On the contrary, AM is defined as the process of joining materials layer by layer (Fig. 2.1.1). The joining may be caused by fusion or by binding of the surfaces or by solidification of resin / powder by melting. A three dimensional computer model is needed to define the shape and size of the component in the AM processes (generally, a computer-aided design files (CAD) or a computer tomography CT scan). AM gains the following advantages over the SM processes (Fig. 2.1.2).

Fig. 2.1.2. Advantages of the additive manufacturing technologies [Ema13a].

(1) **_Design freedom_**: Since tooling and machining are not required in the case of additive manufacturing, the design process has an extra degree of freedom and the design changes can be modified at any time with ease.

(2) **_Speed_**: Less time is required to produce near net shape components. No molds or dies are required, hence allowing the production parts of any shape and size and even structures.

(3) **_Costs_**: Since no molds and dies are required, design changes can be done without any additional cost.

(4) **_Environment friendly_**: AM is an energy efficient process that leads to minimal wastage of material during the production stage; the process is thus environment friendly and is expected to support green manufacturing.

(5) **_Convenience_**: Design and production can be carried out with minimal labor and at convenience and ease.

Subtractive manufacturing
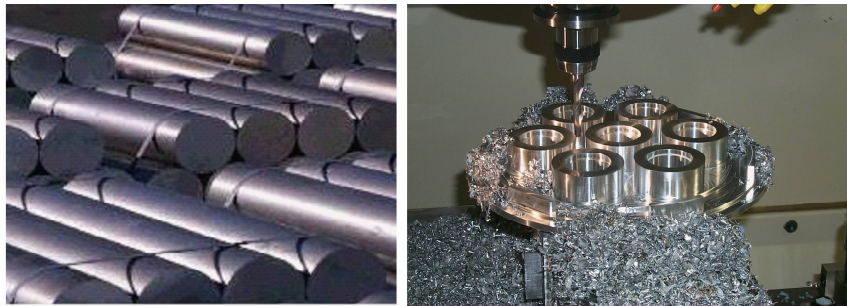
Additive manufacturing
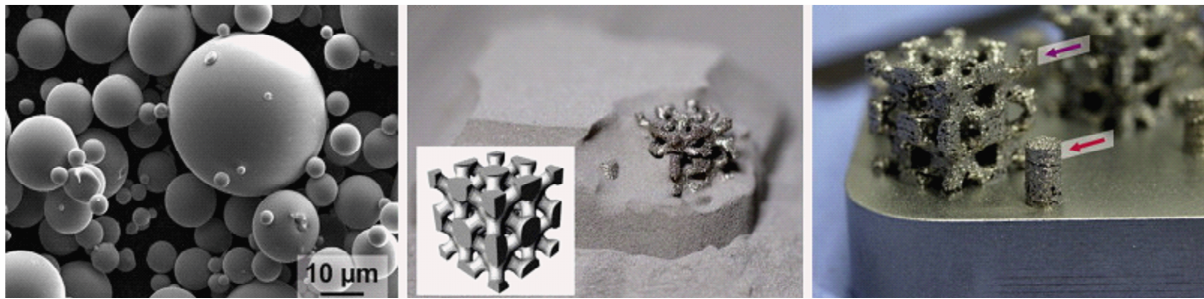
Fig. 2.1.3. Process flow showing the differences between the conventional subtractive manufacturing and additive manufacturing processes ([Fab11a], [Pau13a]).

2.1.1 Additive manufacturing technology (AM)

Additive manufacturing (AM) is defined by ASTM as the "*process of joining materials to make objects, usually layer by layer, from a 3D CAD data*" [AST12a]. Although the first reports on additive technologies like topography and photosculpture to replicate objects, date back to the 1800's ([Noo06a], [Rob12a]), the first successful attempt in the field of AM can be considered the technology developed in the 1970's. Rapid development of AM took place between 1980's and 1990's and it has seen increasing industrial applications in the last 20 years. Initial commercialization of an AM process took place in 1987 in the form of stereolithography from 3D systems [Jac92a]. Stereolithographgy is a process that uses a combination of both photochemistry and laser technology to build parts from photopolymer resins. SLA-1 was the first commercially available AM system and was known as SLA 250 machine (SLA – Stereolithography apparatus). The commercial SLA 250 was replaced by the next generation Viper SLA product from the 3D system. The first generation acrylate resins were commercialized in 1988 and this invention was a collaborative work from the 3D systems and Ciba-energy.

The development of new AM technologies slowly gained momentum in 1991, when three new AM technologies were commercialized. This included fused deposition modeling (FDM) from Stratasys [Hut01a], solid ground curing (SGC) from Cubital [Geb03a] and laminated object manufacturing (LOM) from Helisys [Lam06a]. FDM is a process which uses a plastic filament or a metal wire that is unwound to an extrusion nozzle. The nozzle is heated to melt the material and at the same time, the material is extruded from the nozzle. The material hardens immediately upon extrusion from the nozzle. SGC uses a UV-sensitive liquid polymer, solidifying the entire layers in one pass by UV light through masks created using an electrostatic toner on a glass plate. LOM is an AM process that bonds and cut sheets of material using a digitally guided laser. The next generation AM processes were commercialized in 1992, when both the selective laser sintering (SLS) from 3D systems and the solid form stereolithography system from Teijin Seiki were unveiled [Woh09a]. SLS fuses powder particles (plastics / metal / ceramic / glass) using the heat from a laser to produce a 3D component.

The next innovation shaped in the form of a multi-color 3D printer from Z Corporation [Mal04a]. 3D printers produce parts and assemblies in a similar fashion like a standard inkjet printer, however it spreads layers of plaster or resin powder and binds them together. 3D printing is faster, more affordable and easier to use than other additive technologies. Selective laser melting (SLM) got its birth and definition in the end of 1994 from the Fraunhofer Institute ILT in Aachen, Germany, and was patented immediately (ILT SLM patent DE 19649865). SLM uses a 3D computer aided design (CAD) data as a digital source of information and energy in the form of a high-powered laser beam to create 3D metal parts by fusion of metallic powder particles [Shi04a]. SLM is one of the few processes in the arena of AM that plays a key role even until date and so has received considerable attention and importance.
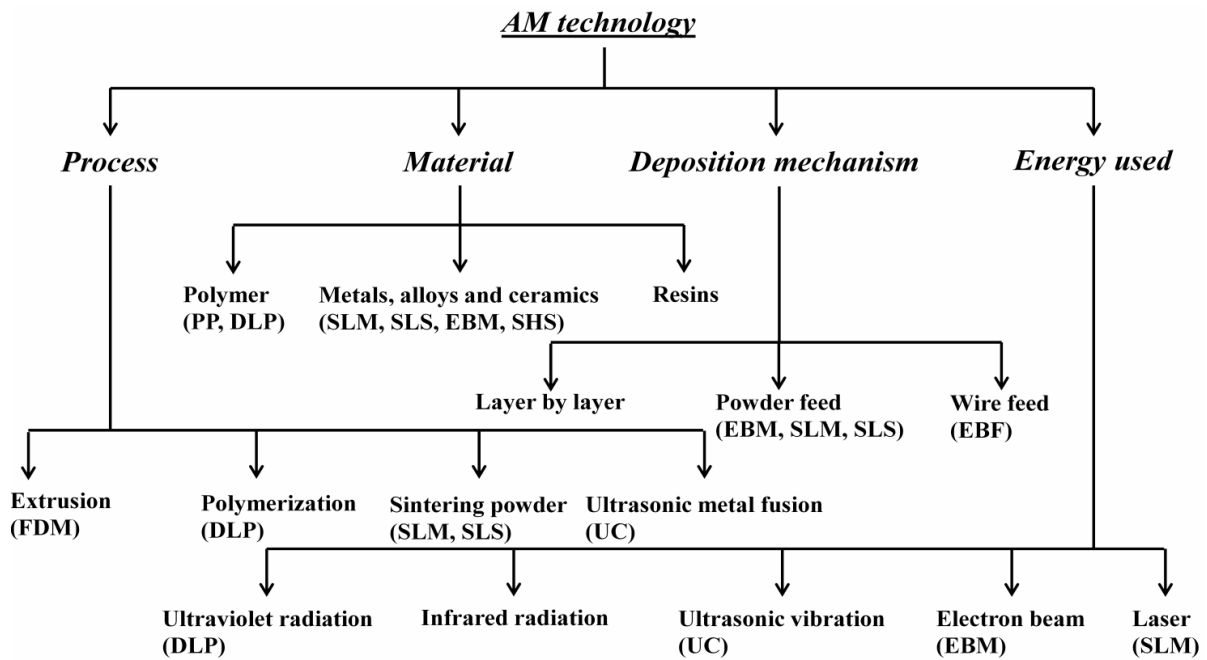
Fig. 2.1.4. Detailed flowchart showing the classification of the additive manufacturing processes based of four major groups.

The AM processes can be classified into four different categories depending on the technology used, the materials processed, the deposition mechanisms involved, and on the source of energy used during manufacturing (Fig. 2.1.4). For instance, the various AM

technologies use different processing techniques for the production of the parts / objects. The FDM technology uses the extrusion process, whereas digital light processing (DLP) uses polymerization for building 3D parts. SLS uses sintering and ultrasonic consolidation (UC) utilizes ultrasonic waves for the production of the parts. In addition, there are different types of energy sources that are used in AM; for example, DLP uses ultra violet radiation, ultrasonic waves are used in UC, electron beam is utilized in electron beam melting (EBM) process and a laser beam is used in both SLM and SLS.

2.1.2 Applications of additive manufacturing technology

As wide ranges of materials can be processed with the different AM processes with different deposition mechanisms and different sources of energy, the AM technologies find its applications in almost every field (see Fig. 2.1.5).
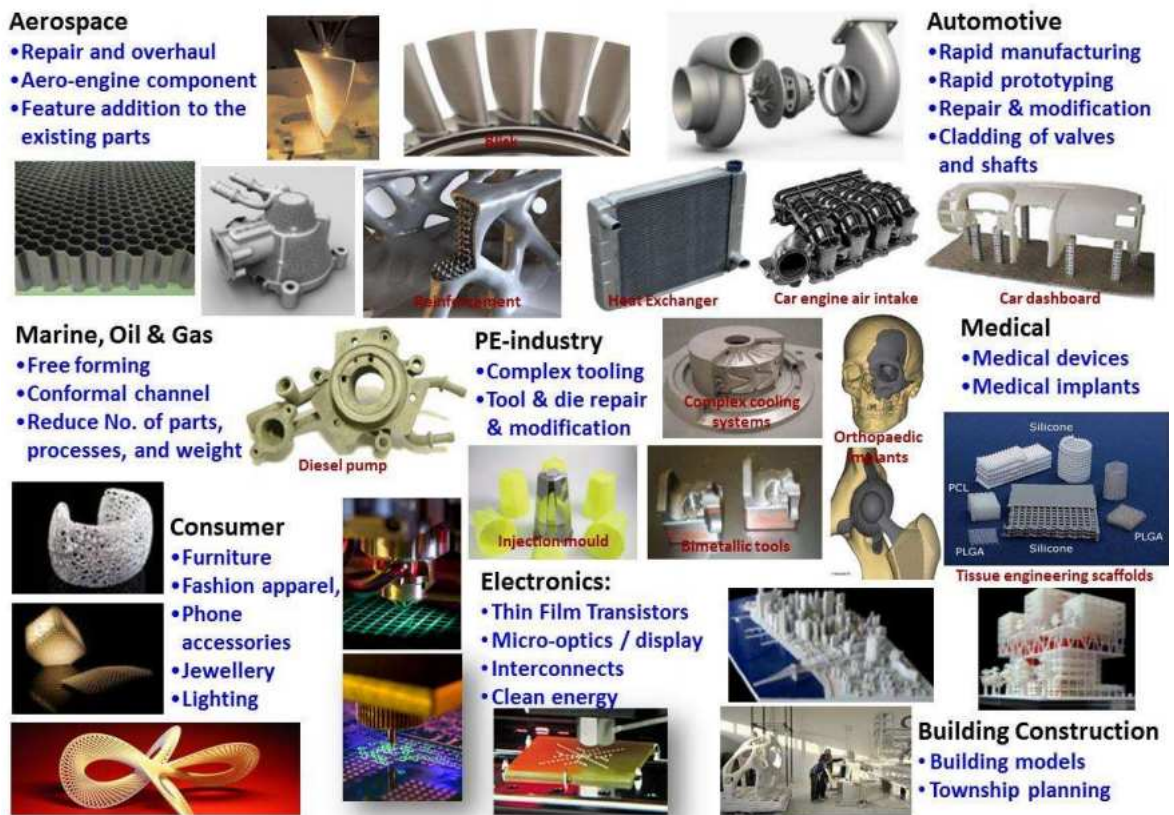
Fig. 2.1.5. Applications of additive manufacturing in different sectors [Jun13a].

(1) ***Aerospace industry***: In principle, any aerospace components can be produced by AM. However, most of the industrial applications lie in the production of jet engines, rib-web structural components, turbine engine cases, engine blades, vanes, discs etc. ([Woh09a], [Woo09a]).

(2) ***Automotive industry***: AM is particularly used in the production of gear boxes, heat exchangers, car wheels, connecting rods, pistons, valves, conformal channels etc. [Hum13a].

(3) ***Medical applications***: AM comes as a lifesaving process in the medical sector. It finds its applications for the production of orthopedic implants, surgical aids, instrumentation tools, painted organs, tissue engineering, scaffolds, artificial skins, artificial bladders, medical implants, medical devices ([Coh06a], [War09a]).

(4) ***Machinery applications:*** Rapid production of injection mold tooling, injection molds, bimetallic tools, assembling-free assemblies, complex conformal cooling systems etc. [SLM13a].

(5) ***Marine, oil and gas sectors***: Conformal channels, fuel injection swirls etc. [WLi12a].

(6) ***Electronics industry***: Fully printed thin film transistors, micro-optics / display manufacturing, 3D printed electronics, 3D printed interconnects, etc. [Sie09a].

(7) ***Consumer applications***: AM finds its applications in the consumer sectors as well as for jewelry manufacturing, fashion apparel, phone accessories, lighting accessories, etc. [Sie09a].

(8) ***Building construction***: Building architectural models and town-ship planning are some of the applications of AM in the building sector [Tho06a].

(9) ***Food industry***: AM finds here its application as a 3D food printer [Lip10a].

2.2 Selective laser melting (SLM)

As discussed in Section 2.1.1, SLM is an additive manufacturing technique that, from the data provided by a 3D CAD file, produces a corresponding 3D metal part by fusing the metallic powders layer by layer. The SLM has the potential of producing end-use parts that can be used directly for industrial applications. The production of parts by SLM involves two

essential steps (1) computational part (2) production of the actual part. The different steps that are involved in the computational part are shown in Fig. 2.2.1.
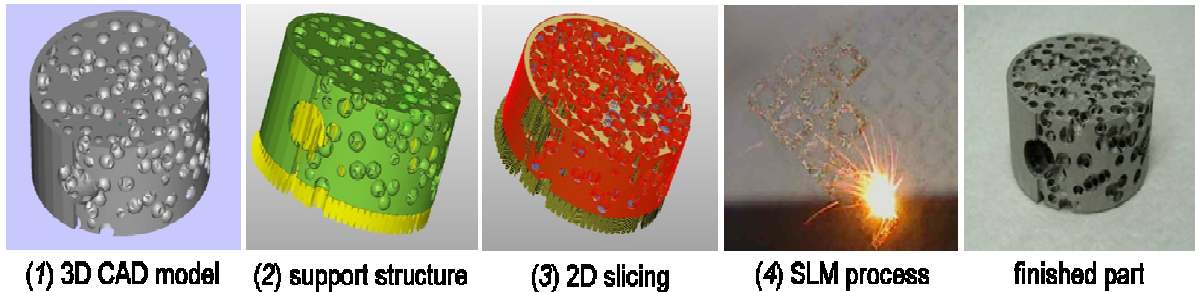
Fig. 2.2.1. Steps involved in the production of a 3D metal part using selective laser melting.

The first and the foremost step in producing a component using SLM is the creation of a 3D CAD model resembling the component to be produced. Generally, SLM produces components on a substrate plate (or base plate), which is of the same or similar material as the part to be produced. In order to remove the part easily and effectively from the substrate plate, halo structures are built before producing the actual component. Such structures (i.e. the support structures) are placed between the component and the base plate. The data for the support structures are then added to the 3D CAD model of the component. This is the absolute data, which has the complete information about the part and the support structures.
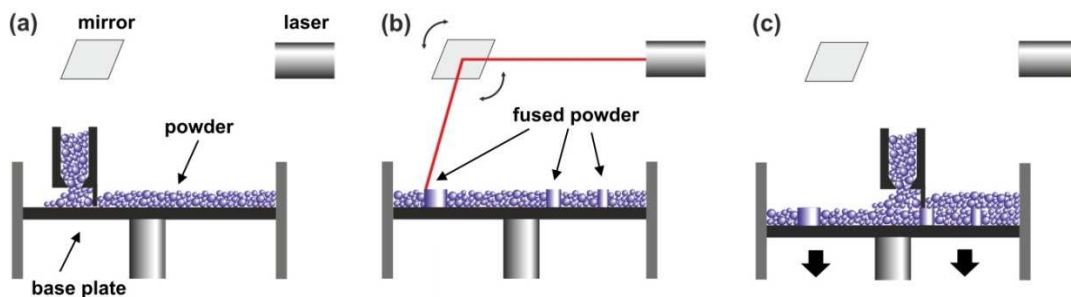
Fig. 2.2.2. Selective laser melting: the process flow diagram [Pau13a].

As per SLM's definition, the parts are produced layer-by-layer and hence the CAD data should contain the layer wise information about the component. For this, the absolute

data is sliced into layers and hence the information available at each layer is two-dimensional. This sliced data are now ready to be used for generating a 3D part using SLM (Fig. 2.2.1).

The second stage of the SLM process involves the production of the actual part, where a thin layer of powder is deposited over the base plate by a specially designed loader, as shown in Fig. 2.2.2. The loader then moves out of the path of the laser and the laser melts the powder selectively as dictated by the sliced CAD data. After the melting step, the base plate is lowered by an amount corresponding to the layer thickness; the loader then deposits the next layer of powder, which is selectively melted by the laser. This iterative process continues, until the entire part is complete. Upon completion of the part, the base plate along with the part is displaced from the chamber and the 3D part is removed from the substrate plate.

2.2.1 Powder properties

There are certain powder properties that play a decisive role during the SLM process. All the physical properties of the powder, such as density, melting point, thermal capacity, latent heat of fusion, determine the melt enthalpy. The melt enthalpy is defined as the amount of energy needed to melt the powder completely ([Atk08a], [Van07a]) and determines the heat balance of the system [Kha10a]. The thermal conductivity of the system is one of the main factors in determining the heat balance. The internal stresses introduced in a component during solidification are dependent on the thermal expansion coefficient of the system [Tip08a] and these are intrinsic properties of the metal or alloy.

Particle size distribution is a mathematical function that defines the relative amount of particles (by mass) according to their size ranges. This property defines an important powder property - the flowability of the material [Ger89a]. The ratio of the larger to smaller particles in the powder can dictate the flowability [Zhu07a]. Other factors like humidity and particles shape, can also affect the flowability. For example, spherical particles have better flowability than the dendritic and irregularly shaped particles. If the powder contains a larger volume fraction of small particles, there is a high probability that the particles agglomerate, which

may negatively affect their flowability. This is due to the pronounced van der Wall forces in the small particles, thus making the deposition process difficult ([Sim04a], [Boi01a]).

A very narrow particle size distribution can help in improving the consistency of the melt but can have detrimental effect on the packing density of the material [Lae00a]. The presence of a high volume fraction of small particles helps in reducing the energy required to melt the material and can improve the surface roughness of the SLM parts ([Kar98a], [Sea99a], [Syv00a], [Lu01a]). In addition, the layer thickness can be reduced by using a smaller particle size. It has been reported by Mazumder et al. [Maz00a] that, with increase in the layer thickness, the laser beam has to diverge by a larger distance in order to form a melt pool. In this case, the thickness of the pool at the bottom will be larger than at the top, giving rise to an asymmetry in the pool width. This asymmetry can be reduced by reducing the layer thickness, which means by reducing the particle size. This also helps in reducing the surface roughness of the parts along their sides. This shows that the particle size as well as the particle size distribution plays a significant role in the SLM process not only determining the process parameters, but also in deciding the final quality of the parts.

The other important property of the powders is their morphology. Powder morphology relates to the shape of the powder particles and it depends on the method of preparation. For example, powders produced by mechanical alloying / mechanical milling have irregular shape [Sur01a], whereas the gas atomization leads to spherically shaped particles [She79a]. Spherical particles improve the flowability during processing and, consequently, the quality of the final product produced using the AM technology [Niu99a]. Non-spherical particles lead to less compaction thereby increased porosity in the SLM parts [Maz00a] and are considered non-desirable for the SLM process.

The density of the powder is another important property in the light of the SLM process. The density can be classified into two types: the individual particle density and the packing density. The individual packing density is an intrinsic property of the metal or alloy system, whereas the packing density is dependent on the particle morphology and the size and distribution of the particles. The thermal conductivity of a powder bed depends on the number of contact points between the particles. The higher the packing density, the more

numerous will be the contact points and the higher will be the heat transfer across the powder layer. Other properties like viscosity, absorption coefficient, and surface free energy also play a role in SLM processing but are less significant than the properties discussed above.

2.2.2 Process parameters

SLM is a complex process where a large number of parameters can influence the quality of the final part. Laser power, laser spot size, scanning speed, layer thickness, hatch style and hatch spacing are some of the important parameters that have to be taken into account [Kru04a]. The quality and the properties of the SLM part need fine parameters tuning in order to optimize the melting step and the energy density involved in the process. The energy density, E_d, is the amount of energy supplied to the material during the melting step and can be expressed as:

$$E_d = [P / (v_s \; x \; h \; x \; t)] \; (J/mm^3) \qquad , \qquad (2.2.1)$$

where P is the incident laser power (W), v_s is the laser scanning speed (mm/s), h is the hatch distance (mm) and t is the layer thickness (mm) ([Kru05a]). The above equation emphasizes that the energy density is strongly dependent on the incident laser power, laser scanning speed, hatch distance and layer thickness and indicates the importance of these parameters in the field of SLM.
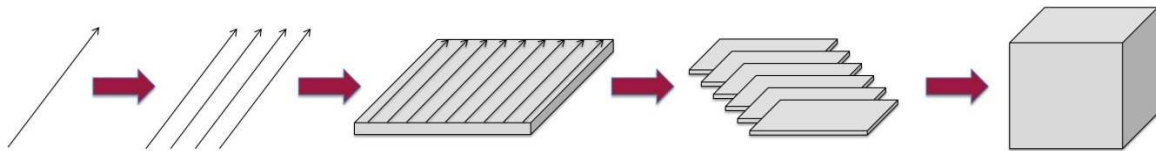
Fig. 2.2.3. Flowchart describing SLM processing from a single laser track to the 3D object.

The hatch distance is another important parameter associated with the SLM process. Fig. 2.2.3 illustrates how a 3D object is made of linear laser tracks. Consider a layer of powder deposited over a substrate plate, as shown in Fig. 2.2.4. The laser is then activated to melt the powder selectively. However, the laser does not melt the entire area of the powder in

a single step, but in the form of several tracks. The width of the tracks depends on the size of the laser beam, the laser power and the scanning speed. The hatch distance is defined as the width of a single melt track as shown in Fig. 2.2.4.
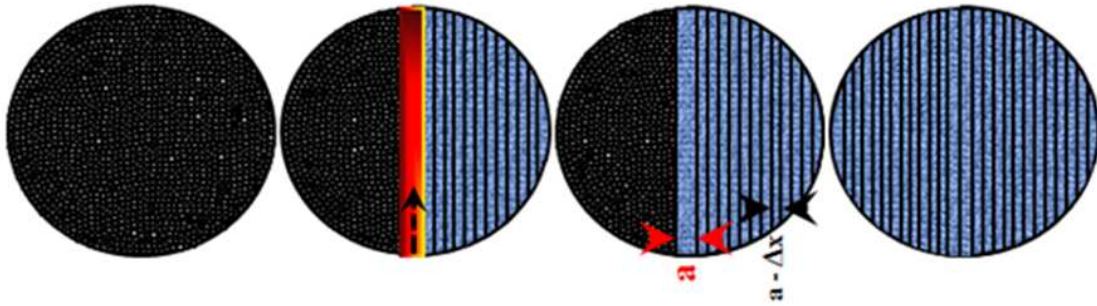
Fig. 2.2.4. Schematics showing the hatch distance and hatch overlap observed during a selective laser melting process.
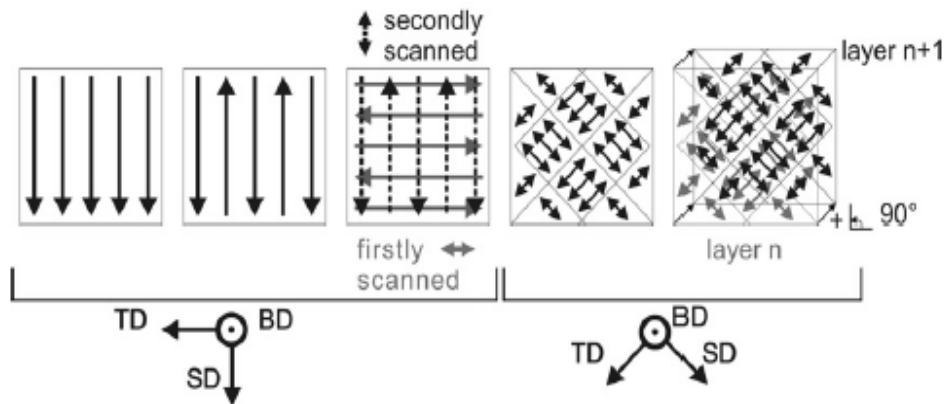
Fig. 2.2.5. Schematics showing different types of hatch styles that are employed in SLM process [Thi13a].

From Figs. 2.2.3 and 2.2.4, it can be seen that a single SLM layer consists of several hatches with hatch distance "*a*" (Fig. 2.2.4). To have a sound sample, conditions are set in such a way that there will be an overlap between two hatches called the hatch overlap - Δx and the effective track distance is the difference between the hatch distance and the over lapping distance (a - Δx). An overlap in the SLM parts is necessary to have continuity between the tracks leading to a solid sample. In most of the SLM processes, an overlap of at

least 20% is maintained to have better quality samples [Van07b]. The hatch style is another key parameter in the SLM process. The hatch style is defined as the design or pattern in which the hatches are oriented within and between the layers. The hatch style can be varied in innumerous ways and the design depends on the creativity of the user and on the specific requirements of the SLM part. Examples of basic hatch styles are shown in Fig. 2.2.5 [Thi13a]: single melt hatch style, single cross melt, double cross melt, checkerboard and finally the checkerboard layered hatch style. These hatch styles may be repeated every layer with or without the presence of hatch style rotations between the layers. The rotation of the hatch style between the layers is carried out to have a better bonding between the layers [Van07a]. All the hatching parameters, namely, hatch distance, hatch style and hatch rotations are expected to influence the properties of the final parts produced by SLM and have a distinct influence on the mechanical properties ([Thi13a], [Van07a], [Van07b]).
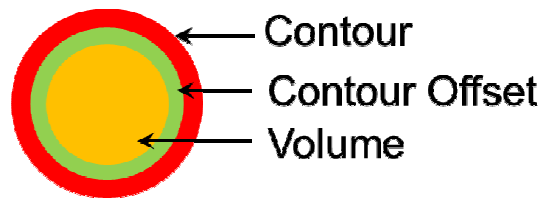
Fig. 2.2.6. Schematic illustrating the different zones identified in a SLM sample: contour, contour offset and actual volume of the part.

The contour of the SLM parts (Fig. 2.2.6) is another aspect that affects the quality of the final object. Contours are the outermost layers observed in the SLM samples (usually of 0.2 - 0.5 mm in thickness). They are used to improve the surface quality (roughness) and/or aesthetics of the parts. Generally, contours have different parameters than the bulk of the sample to achieve a smooth surface. In most of the cases, contours use the same laser power as the bulk of the sample, but have a faster scanning speed than the bulk of the sample [Yas11a]. The space between the volume or bulk of the sample and the contour is called as the contour offset. The general sequence used in SLM process is: first melting the volume of the sample, then the contour offset and finally the contour. This melting sequence can be varied according to the shrinkage of the part.

2.2.3 Potential applications

Similar to the other AM processes, SLM is widely used to prepare cellular and lattice structures [Dot09a]. Metallic cellular structures have been widely used as industrial components (heat exchangers), in chemical industries, and in the aerospace and automotive sectors. The cellular structures possess low density, high strength, good energy absorption and good thermal and acoustic properties [Dot08a]. Periodic cellular structures can be highly porous and the volume occupied by the solid material can be less than 10% ([Eva01a], [Löb11a]). The SLM technology extends the possibility to produce parts made of complex engineering materials (e.g. stainless steel, tool steel, titanium alloy and cobalt-chromium alloys) and give designers the freedom to use the cellular materials with better functionality of a product without sacrificing their mechanical properties [Cam10a]. The SLM technology is beneficial for the production of cellular structures because it provides the complete freedom in defining the geometry of the part [Kru06a] and reduces the production cycle [San06a] as well as the material usage.
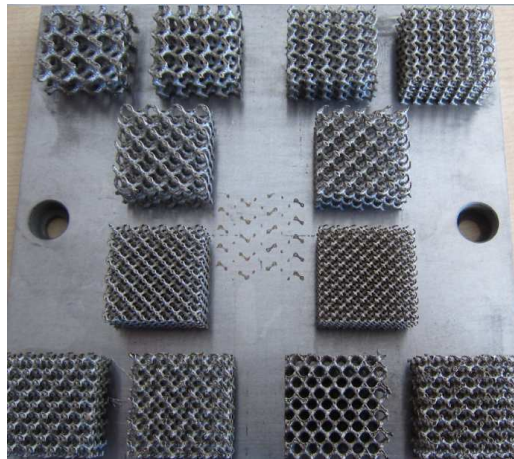
Fig. 2.2.7. Different types of lattice structures made of stainless steels processed with SLM [Hao13a].

Fundamental research onto manufacturing and computer coding has resulted in novel lattice structures that have the capability of replacing dense volumes of materials, retaining adequate stiffness and strength compared to the bulk parts (Fig. 2.2.7). Such lattice structures not only reduce the time needed for the preparation of the parts but also reduce processing

and materials costs [Reh06a]. The design optimization and the optimization of the process parameters for both lattice and cellular structures have attracted remarkable attention from industry [Bro05a]. The lattice structures developed by Brooks et al. [Bro05a] are lightweight parts with only 6% of the relative density of the equivalent bulk material. These lattice structures find their application as heat exchangers [Won07a], orthopedic implants [Mul09a], ultra-light aerospace components etc.

Another potential application of SLM is in the tooling industry, especially in the production of injection molds [Cam10a]. The cooling phase in the injection molding process determines the rate at which the components can be produced. Reduction of the time spent on the cooling phase would drastically increase the production rate and drastically reduce the production costs [Dim05a]. The cooling rate can be increased significantly by creating conformal cooling channels and to take the heat away at a maximum rate (Fig. 2.2.8). The recent advancements in the field of AM and SLM give the design freedom to produce injection molds with complex conformal cooling channels ([Sac00a], [XXu01a]) and offers a more accurate route for producing such intricate parts.
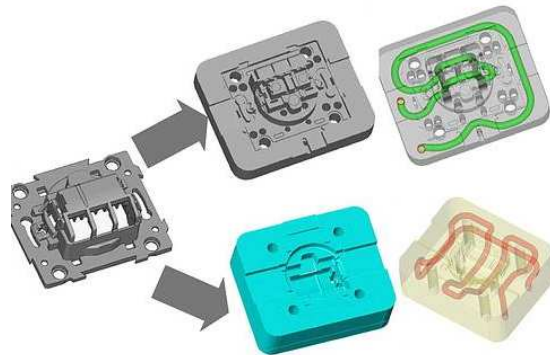
Fig. 2.2.8. Precision steel molds illustration of conformal cooling channels in the A and B halves of the mold [Tob13a].

Internal geometries with complex designs that cannot be produced by any other means of manufacturing can be generated by SLM. They are expected to lower the manufacturing costs and to increase the added performance values over conventional

processes. SLM has been used to design and produce the cross-flow heat exchangers made from stainless steel and Cu [Tso05a], and heat sinks from Al [Won07a]. SLM finds its focus also in the medical and biomedical engineering. Medical industry utilizes the advantages of SLM to manufacture surgical cutting guides, as shown in Fig. 2.2.9 [Bib05a]. These cutting guides are used to facilitate pre-surgery planning and to reduce the operational times. In the dental sector, dental crowns and bridges made of SLM are commercially available [Woh10a].

Fig. 2.2.9. The surgical cutting guide made of Ti-based alloy, fitted to the patient's body during surgery [Bib05a].
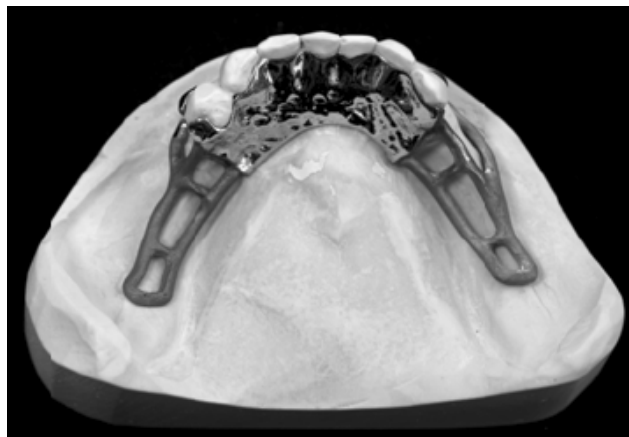
Fig. 2.2.10 Removable partial dental framework (RPDF) specimen prepared by selective laser melting [Bib06a].

Removable partial dental frameworks (RPDF) prepared by SLM (Fig. 2.2.10) are also available in the market [Bib06a]. Medical devices, such as SLM implants made of Ti and Cr,

have been successfully implanted in the human body, which has widened the scope of SLM ([Tol02a], [Ser08a]). Standards and compliance in high-value industries have become a constrain in the advancement in applying SLM to medical devices (Fig. 2.2.10). Research on SLM has shown that the surface finish of the implants can be manipulated to be selectively porous, and lattice-like structures can be added to the parts to promote osseointegration (bonding between the bones and the implant) in the implants [Ruf09a]. Several surgeries have now been successful with the parts produced from SLM [Ruf09a].

2.3 Systems examined using SLM

Scutcliffe quoted that "*there is worldwide interest in developing a standard rapid manufacturing process based on selective laser melting*" [Nan06a]. SLM is one of the newest advanced technologies. Hence, only limited research has been done on this topic and very few reports are published on the aspects of the process development and on the application of SLM as an additive manufacturing technology. The SLM process is now growing as a viable alternative process in the biomedical and aerospace markets, since it has the capability of manufacturing parts with extremely complex geometries using materials such as Ti, Al and various types of steels [Woh09a]. Widening the inventory of materials that can be processed by SLM will expand the scope of its applications.

The number of systems processed by SLM is relatively limited. Most of the research is based on Fe-based and Ti-based alloys [Pra13a]. The target lies on the effects of the laser parameters on density, surface morphology, structure formation and mechanical properties in case of pure Fe, stainless steels and tool steels ([Löb11a], [Yas11a], [XSu12a], [Yad10a], [Yad11a]). The focus of the research on Ti-based alloys is towards their application: optimization of the processing parameters and related physical and mechanical properties for exploiting the biomedical properties of Ti-based alloys, like Ti-Nb and TiAlNb alloys ([Wan10a], [Gor11a], [Zha11a], [Pat11a], [Cha11a], [Sal13a]). The other application is in the aerospace sector (e.g. Ti6Al4V), where the focus lies in parameter optimization and understanding the relation between structure and mechanical properties ([Vra12a], [Sun13a],

[DGu09a], [Thi10a]). Co-based alloys were also processed using SLM for their biocompatibility in medical applications ([Tak13a], [Xia12a], [Xin12b]).

Both Al-based and Ni-based alloys have attracted considerable attention in the field of SLM processing and alloys development. The research on Ni-based alloys (Nitinol, waspaloy, inconel and nimonic) is focused on the shape memory effect and high temperature applications ([Shi12a], [Mum08a], [Ama12a], [Zha13a], [Vil12a]). The experiments on the Al-based alloys are basically application driven, especially as lightweight materials, and are confined to only two systems: 6061 and AlSi10Mg ([Won07a], [Bra12a], [Kem12a], [Thi13a]). Not much work has been carried out on Cu-based systems. There is a recent report focusing on the thermal behavior and densification mechanism during selective laser melting of copper matrix composites [Dai13a]. Apart from few exceptions ([Vra12a], [Ama12a], [Vil12a]) limited attention has been paid on the microstructure-property correlations of SLM metallic parts and on the methods to tune and optimize their mechanical properties and this is one of the aspects where light has to be shed on.

2.4 *Solidification fundamentals*

SLM is one of the processes that involve high cooling rates during solidification ([Bou02a], [JLi07a]). The microstructure evolution as well as the solute re-distribution during solidification at extreme cooling rates plays a central role in determining the mechanical, chemical and tribological properties of materials, including objects produced by SLM. Hence, the knowledge of the fundamentals of the solidification phenomena and the modes of solidification are a necessary prerequisite for understanding and properly working with the SLM process. This section focuses on the solidification fundamentals and deals with the equilibrium partition or equilibrium segregation coefficient followed by the fundamentals on solute redistribution phenomena, when the solute has partial or negligible diffusion in the solid and complete diffusion in liquid; it presents the solidification modes and the constitutional supercooling theory and finally the effect of cooling rate and temperature gradient on the microstructure is discussed.

2.4.1 Equilibrium partition / segregation coefficient

Whenever a binary system of uniform composition solidifies from the liquid to the solid state, the ideal condition is to have a solid of uniform composition, provided that the solubility limits of the solute in both liquid and solid state remain the same and that the equilibrium solidification conditions are maintained [Sin03a]. However, the equilibrium conditions may not be achieved due to the presence of impurities or changes in the cooling rate and in the solubility limit of the solute in the solvent both in liquid and solid state. The solute atoms in the liquid are normally redistributed during solidification and the redistribution of the solute depends on both the kinetic (diffusion, super heating, under cooling etc.) as well as the thermodynamic (phase diagram) aspects [Sin03a]. The phase diagram dictates the solubility limit of the solute in the solvent both in liquid and solid state. Depending on the solubility limit of the solute, the solid may either take excess solute from the liquid or reject solute into the liquid. The equilibrium partition coefficient or the equilibrium segregation coefficient "k" is defined as the ratio of the solute concentration in the solid (C_s) to that of the liquid (C_L) at the solid liquid interface at any given temperature "T" [Sin03a]:

$$k = C_S / C_L \qquad , \qquad (2.4.1)$$
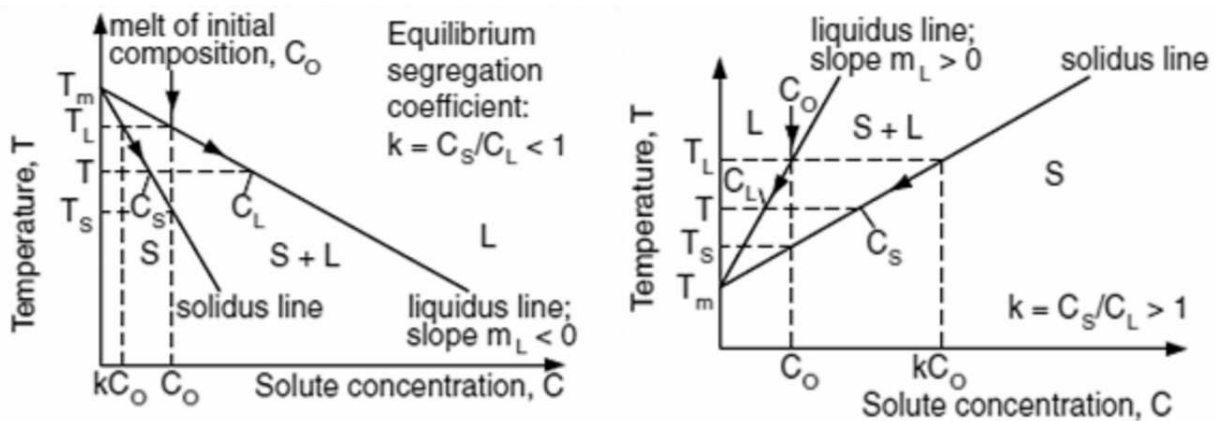
Fig. 2.4.1. Equilibrium segregation coefficient 'k' along the two extremes observed in a binary phase diagram [Sin03a].

The solubility of a solute in a solvent is strongly dependent on temperature and so the equilibrium segregation coefficient is a function of temperature. Fig. 2.4.1 shows both the conditions that are possible in a binary phase diagram where the solute solubility in the solid is less than in the liquid (Fig. 2.4.1 left) and where the solute solubility in the solid is larger than in the liquid state (Fig. 2.4.1 right). Assuming that the initial composition of the melt C_L is C_o at the melting point of the liquid T_L, according to the Eq. (2.4.1) the solute concentration of the solid will be kC_o. In the case where the solute solubility in liquid is more than the solid ($k < 1$), the solid cannot take up the same solute content as the liquid does and hence the solid rejects the excess solute into the liquid at the interface during the solidification process [Sin03a]. As the solid is growing continuously from the liquid at the same time ejecting solute into the liquid, the solute concentration in the liquid continuously rises, resulting in a continuous increase of C_S and C_L as the T of the S/L interface decreases continuously during solidification. Hence, the last solidifying solid will have the highest C_S and such a scenario results in the possibility of preferential segregation of the solute in the solid.

In the case where $k > 1$, the solid can take more solute than the liquid and hence when the solidification proceeds, the solid can absorb more solute than the liquid does [Sin03a]. As a result, the solute content in the liquid drops continuously during solidification. The solid is a resultant product of solidification from the liquid and hence the solute concentration in the solid drops continuously with solidification, and both C_S and C_L decrease as the T at the S/L interface drops with solidification. This shows that the distribution of the solute is strongly dictated by the phase diagram. Equilibrium solidification takes place when the solute can dissolve completely in both solid and liquid, with equilibrium existing between the solid, liquid and the S/L interface, resulting in an uniform solid.

2.4.2 Solute redistribution when the solute has partial or negligible diffusion in solid but complete diffusion in liquid

Consider a scenario where the solute has complete solubility in the liquid state but has partial or negligible solid solubility, as shown in Fig. 2.4.2 [Sin03a]. Solubility in the solid

state is partial or negligible and therefore the solidification process leads to a non-uniform composition in the solid. On the contrary, the solubility in the liquid state is assumed to be complete, and so the liquid has uniform composition. In such conditions, there will be no equilibrium existing between the solid and the liquid phases except at the S/L interface [Sin03a]. In addition, the solute cannot diffuse uniformly into the solid and it is consequently rejected into the liquid. As a result, C_L rises more rapidly during solidification. Since the liquid leads to the formation of a solid, the composition of the solid at the S/L interface C_S also rises more rapidly than in the case of equilibrium solidification.
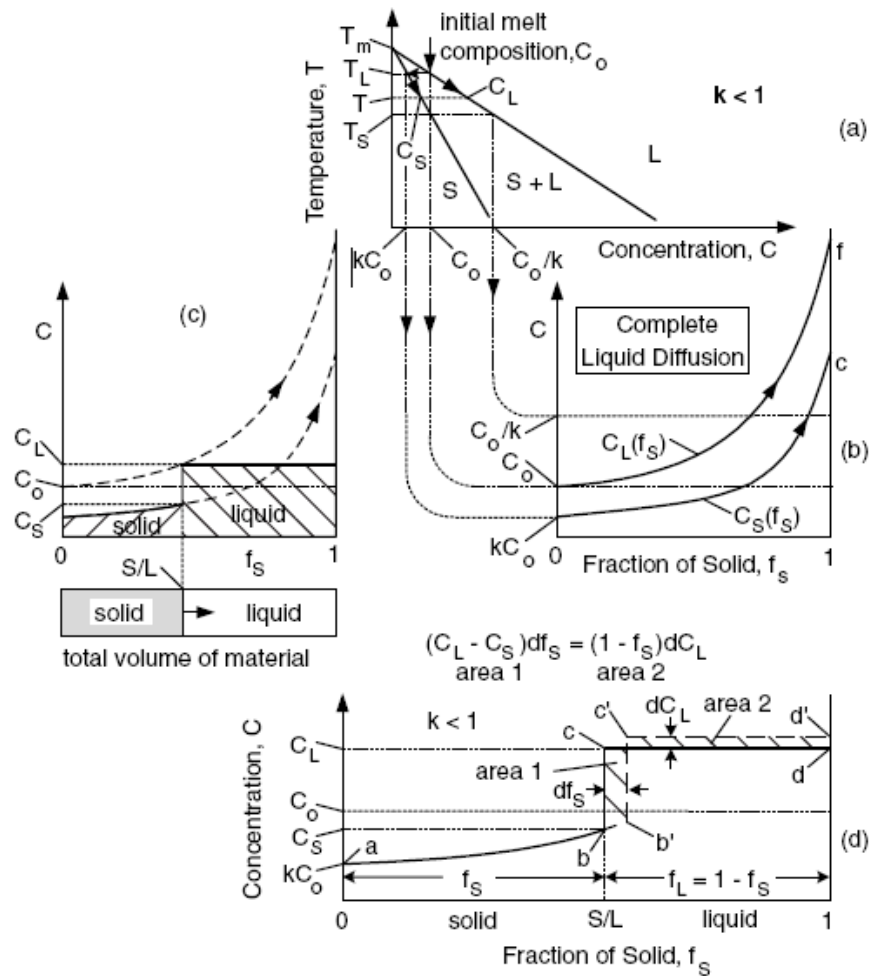
Fig. 2.4.2. Redistribution of solute during the solidification process with partial or negligible diffusion in solid and complete diffusion in liquid. (a) phase diagram (b) variation of C_L and C_S (c) composition profile in both solid and liquid and the S/L interface (d) solute conservation due to partial or negligible diffusion in solid [Sin03a].

From Fig. 2.4.2(b), when C_L rises beyond C_o/k, C_S rises beyond C_o. The solid liquid interface shown in Fig. 2.4.2(c) has the hatched areas corresponding to the solute contents in both solid and liquid state. The sum of the hatched areas correspond to the total amount of solute in the liquid state "C_o", which is the content of the solute before the start of the solidification process. This visualizes the variation of the solute concentration in both liquid and solid states. Fig. 2.4.2(d) shows the conservation of solute in the liquid state during solidification. As the total amount of the solute in the system is conserved, the area under the line abcd and ab'c'd' should remain constant, leading to a modified form of the Scheil equation [Sch01a]:

$$f_L = 1 - f_S = [(-m_L)C_o / (T_m - T)]^{1/1-k} \qquad , \quad (2.4.2)$$

where f_L is the fraction of liquid, f_S is the fraction of solid, $m_L = T_L - T_m / C_o$, C_o is the concentration of the solute in the liquid state before the start of the solidification, T_m is the melting point of the metal and k is the equilibrium partition coefficient. This equation is helpful in estimating the fraction of the solid f_S at any given temperature T below the liquidus temperature T_L.

2.4.3 Solidification modes and constitutional supercooling theory

There are several other kinetic parameters that define the solidification mode and the final microstructure. These include the travel speed of the S/L interface also termed as the growth rate "R" of the metal and the temperature gradient "G" in the liquid metal at the S/L interface, which are key parameters that can be externally varied [Sin03a]. The S/L interface of the pure metals during solidification is normally planar under equilibrium conditions. If a severe thermal undercooling is imposed on a system, the mode of solidification may be altered [Jac71a]. However, during solidification of a metal alloy, the solidification mode can be planar, cellular or dendritic depending on the solidificaiton conditions and on the system involved [Sin03a]. The four types of S/L interfaces that may be observed during solidification are shown in Fig. 2.4.3 ([Jac66a], [Mor69a], [Gia76a], [Katt67a]). There are two major theories that have been proposed to describe the breakdown of the planar S/L interface during solidification. They are the costitutional supercooling theory ([Rut53a],

[Til53a]), which deals only with the thermodynamical aspects, and the interface stability theory ([Sek67a], [Sek65a], [Mul63a]), dealing with the kinetics and the heat transfer aspects. However, this section deals only with the constitutional supercooling theory to simplfy the discussion.
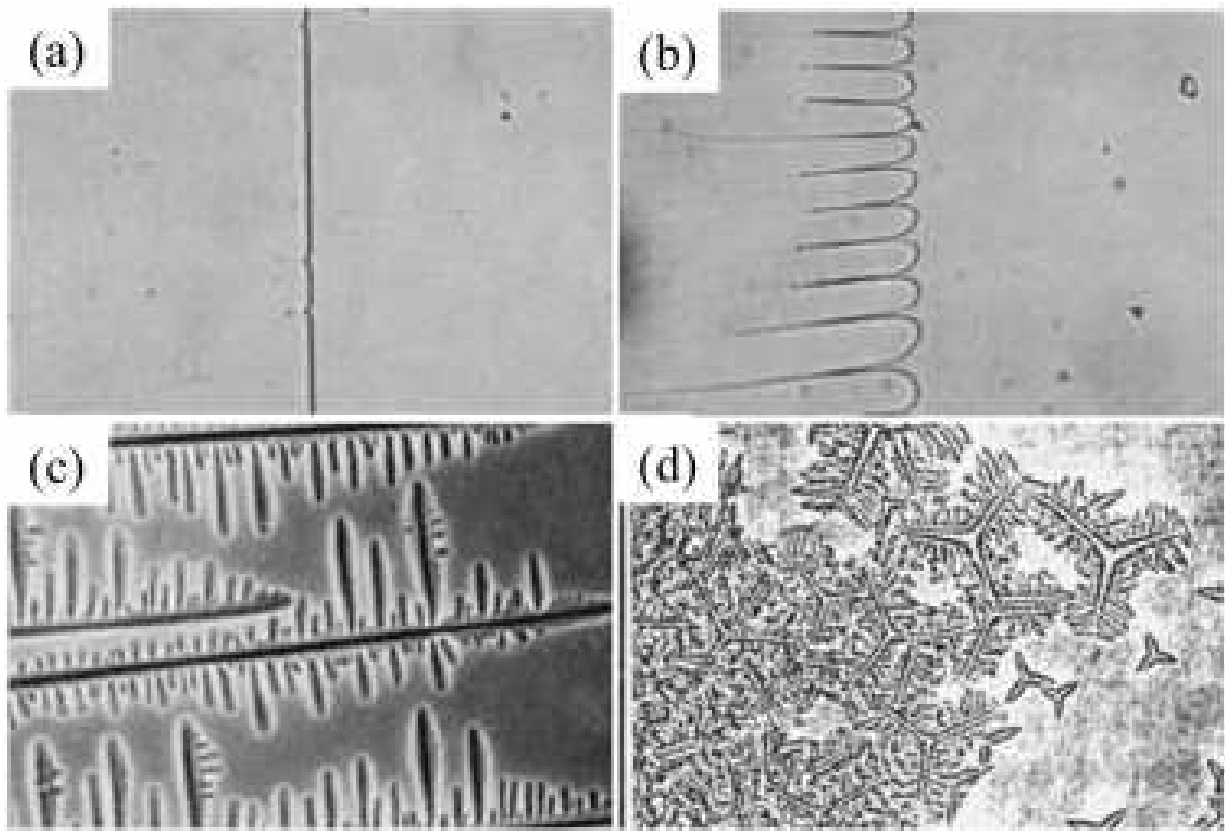
Fig. 2.4.3. The different solidification modes: (a) planar solidification (b) cellular solidification (c) columnar dendritic and (d) equiaxed dendritic solidification modes ([Sin03a], [Jac71a]).

Consider an alloy with C_o as the initial composition of the solute solidifying at a steady state with a planar S/L interface (Fig. 2.4.4). Fig. 2.4.4(b) shows the composition distribution at the solute rich boundary layer and Fig. 2.4.4(c) shows the composition distribution constructed from the liquidus line of the phase diagram [Sin03a]. The liquid phase alone remains stable when the temperature of the melt is above the liquidus temperature. In addition, when the temperature falls below the liquidus temperature a mixture of both the solid and liquid should coexist. Under the coexistence of both solid/liquid phases,

the planar S/L interface cannot remain stable anymore and should collapse into a cellular or dendritic mode (Fig. 2.4.3(b-d)).

The shaded area in Fig. 2.4.4(c) under the liquidus temperature is the region where the actual temperature of the liquid is below the liquidus temperature, which is called the region of constitutional supercooling. This region of constitutional supercooling strongly depends on the growth rate "R" and on the diffusion coefficient "D_L". This is the region where both liquid and solid coexist.
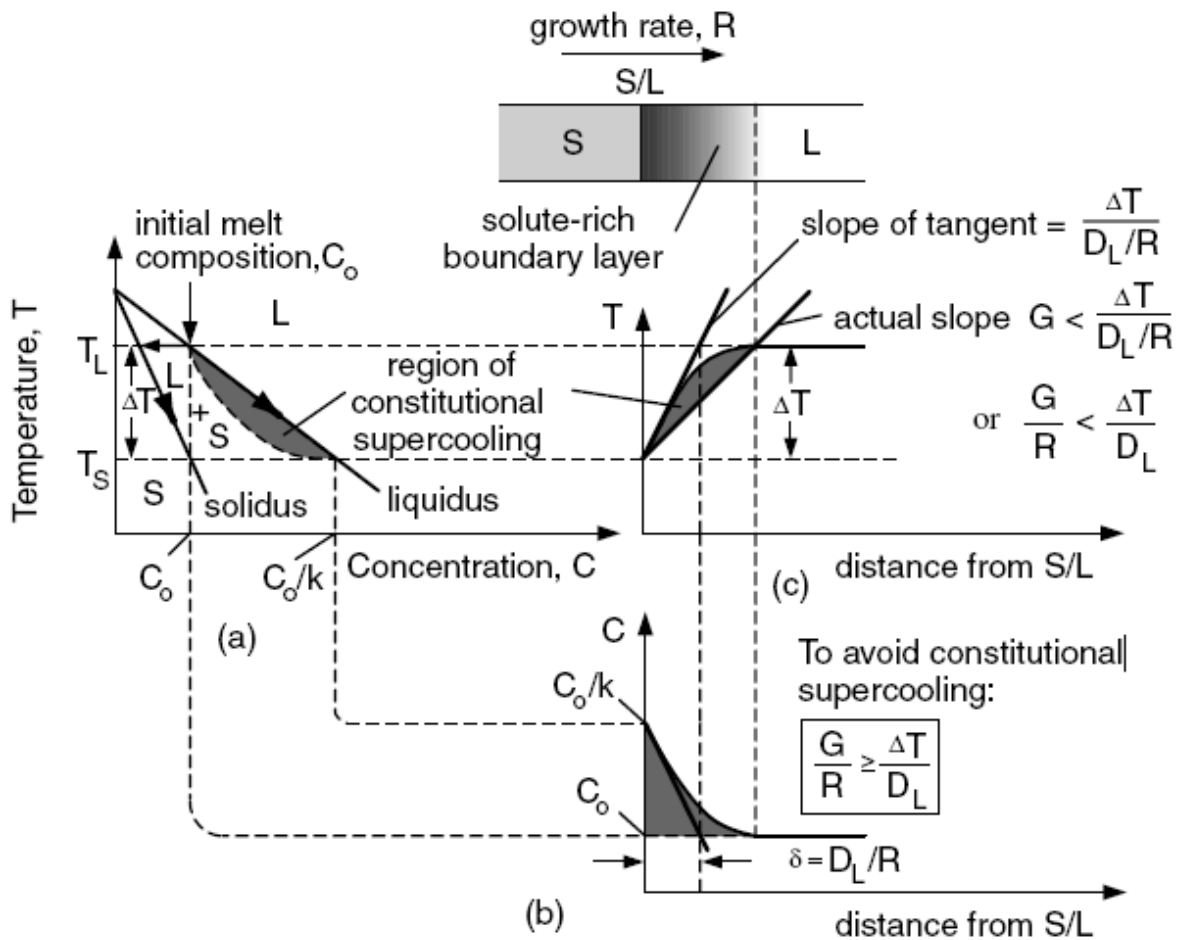
Fig. 2.4.4. Constitutional supercooling: (a) phase diagram (b) composition profile in liquid (c) liquidus temperature profile in liquid [Sin03a].

For a planar S/L interface to be stable, the S/L interface has to meet the following criterion [Sin03a]:

$$(G \, / \, R) \geq (\Delta T \, / \, D_L) \qquad , \qquad (2.4.3)$$

where G is the actual temperature gradient at the S/L interface, R is the growth rate, $\Delta T = (T_L - T_S)$ is the temperature difference across the boundary layer and D_L is the diffusion coefficient in the liquid. This equation is called the steady state equation for planar growth, and suggests that for an alloy to have a planar growth the ratio of G/R should be always equal to or greater than $\Delta T/D_L$. According to this equation, the higher the temperature gradient G and the lower the growth rate R, the easier is the formation of a stable planar S/L interface. On the contrary, high freezing range and low diffusion coefficient do not lead to the formation of a planer S/L interface ([Jac65a], [Bar61a]).
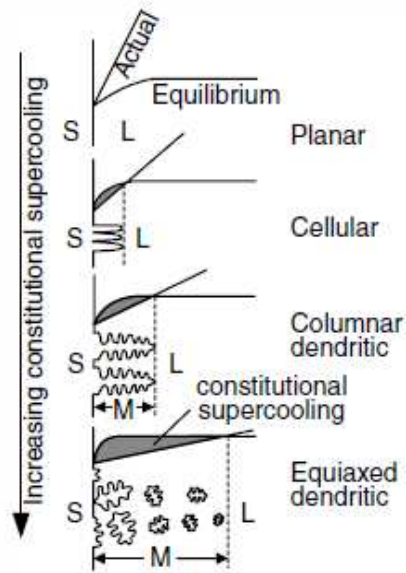
Fig. 2.4.5. Effect of constitutional supercooling on the different modes of solidification: (a) planar (b) cellular (c) columnar dendritic (d) equiaxed dendritic with S, L, M represents solid, liquid and mushy zones respectively [Sin03a].

Fig. 2.4.5 displays the changes in the solidification mode with increasing the degree of constitutional supercooling [Sin03a]. The mode changes from planar to cellular, to

columnar dendritic, and finally to equiaxed dendritic with increasing the degree of constitutional supercooling. The region where the columnar / equiaxed dendrites coexist with the liquid phase is termed as the mushy zone. It has been observed [Sin03a] that the area of the mushy zone widens with the increase in the degree of constitutional supercooling aiding the equiaxed dendrites to nucleate than a columnar dendrites to stretch over the entire mushy zone (Fig. 2.3.5(d)). However, considering only the thermodynamical aspects, a simple theory like the constitutional supercooling theory cannot accurately predict the cellular to columnar to dendritic transitions. Rather, it offers general guidelines and ideas suggesting the solidification mode.

2.4.4 Influence of cooling rate and temperature gradient on microstructure

Apart from the above discussed factors like constitutional supercooling, diffusion parameters etc., the cooling rate during solidification also plays an important role in deciding the microstructural features like the size and morphology of the phases (Fig. 2.4.6). It has been observed that the increase of the cooling rate leads to reduced solidification time, resulting in a fine cellular or a dendritic structure [Fle74a].
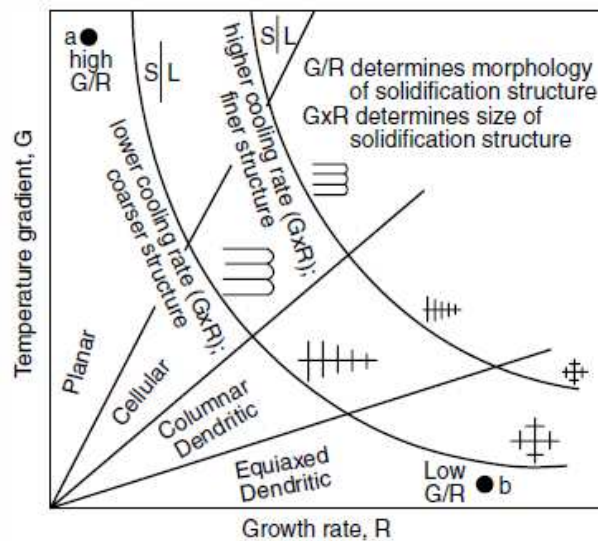
Fig. 2.4.6. Effect of growth rate and temperature gradient on the morphology and size of the solidifying microstructure [Sin03a].

The relationship between microstructure and cooling rate can be expressed as [Pla60a]:

$$d = b(\varepsilon)^{-n} \qquad , \qquad (2.4.4)$$

where d is the secondary arm spacing, ε is the cooling rate and b is a proportionality constant. This equation suggests that the slower the cooling rate during the solidification process; the larger will be the dendrite arm spacing due to the availability of sufficient time for coarsening of the phases. Fig. 2.4.6 shows the influence of the growth rate and temperature gradient on the solidification structure [Pla60a]. It can be observed from Fig. 2.4.6 that the combination of both temperature gradient G as well as the growth rate R dictates both the size of the solidification structure and the mode of solidification. The ratio G/R determines the mode of the solidification, whereas the product GR governs the size of the solidifying microstructure.

2.5 Al-based alloys

Al-based alloys have received the attention of the scientific as well as of the industrial community due to their positive combination of high tensile strength with low density [Alu89a]. For example, they have been extensively used in the automotive and aerospace industries, with the aim of replacing the majority of the heavy parts using light metals to reduce the weight of the components and, in turn, increase the fuel efficiency and decrease the energy consumption and greenhouse gas emission [Alu89a]. In addition, the reduction in mass of the vehicles offers indirect financial saving as well. For instance, the reduction of weight gives the opportunity to the manufacturers to offer the same vehicle performance with a smaller engine and such a smaller engine leads to an overall cost reduction [Mil00a].

Ever since Al and its alloy were first used in the transportation sector, they have made an impressive contribution in reducing the mass of the vehicles. The demand for aluminum in the transportation sector has shown an increasing trend. In 2005, about 30 % of aluminum used globally was used in the transportation sector. In 2000, each automotive vehicle contained between 100 and 120 kg of aluminum and is increased between 110 and 145 kg in

2006 [Alu07a]. Depending on their application (e.g. bumper or motor block), each kilogram of Al and its alloy replacing the conventional steel or cast iron can save between 13 to 20 kg of greenhouse gas emissions [Alu07a].

Even though the commercially pure aluminum is very soft (tensile strength of about 50 MPa) [Roo90a], the strength of Al can be increased by proper addition of alloying elements and by the utilization of the versatile strengthening methods, like solid-solution hardening, work hardening and precipitation hardening, according to the specific application [ASM95a]. The Al-based alloys can be classified into two major categories: casting and wrought compositions ([ASM95a], [Mil98a], [Alu89a]). A wrought alloy is formed by mechanical working like forging, hammering etc., whereas cast alloys are produced from the molten metal by solidification in a mold of definite shape and size. Both categories can be further subdivided based on the property development mechanism. Depending on the alloying elements and on the phase development, many alloys respond to thermal treatments. These thermal treatments include solution heat treatment, quenching, and precipitation, or age hardening.

The alloys that respond to thermal treatments are termed as heat-treatable alloys ([ASM95a], [Mil98a], [Alu89a]). Most of the wrought compositions rely on work hardening through mechanical working as strengthening mechanism [ASM95a] and are termed as work hardening or non-heat treatable alloys. Both wrought and cast Al alloys are identified by a unique four-digit numerical designation, where the first digit indicates the alloy group, as shown in Table 2.5.1 ([ASM95a], [Mil98a], [Alu89a]). For the wrought Al alloys, the second digit indicates the modifications of the original alloy or the impurity limits. For the cast Al alloys, the second and third digits identify the Al alloy or indicate the minimum Al percentage. The last digit, which follows the decimal point, indicates the product form: for instance, XXX.0 indicates castings, and XXX.1 and XXX.2 indicate ingot. Commercial alloys are strengthened either by thermal treatment or by work hardening. The degree of strengthening can be expressed by a suffix to the alloy code. The most widely used systems uses the following letters to indicate the nature of the treatment ([ASM95a], [Mil98a], [Alu89a]):

Table 2.5.1. Basic designation for wrought and cast Al-based alloys ([ASM95], [Mil98], [Alu89]).

	Wrought alloys		Cast alloys
Alloy group	**Major alloying elements**	**Alloy group**	**Major alloying elements**
1XXX	Commercial purity / low alloy	1XX.0	99% minimum Al
2XXX	Cu	2XX.0	Cu
3XXX	Mn	3XX.0	Si with added Cu and/or Mg
4XXX	Si	4XX.0	Si
5XXX	Mg	5XX.0	Mg
6XXX	Si, Mg	6XX.0	Unused series
7XXXj	Zn	7XX.0	Zn
8XXX	Other elements	8XX.0	Sn
9XXX	[Unused series]	9XX.0	Other elements

F = as-fabricated (no specific treatment - the properties of the as-fabricated sample depends on the forming method used). This is applied to products shaped by cold working, hot working, or casting processes in which no special control over thermal conditions or strain hardening is employed.

O = annealed. This designation is applied to the wrought products that are annealed to obtain lowest-strength temper and to cast products that are annealed to improve ductility and dimensional stability.

H = strain-hardened (wrought products only). This designation is used to indicate the strengthening of the product by strain hardening with or without supplementary heat treatment.

W = solution heat-treated. This designation implicates an unstable temper condition applicable only to alloys whose strength naturally changes at room temperature over a duration of time after solution heat treatment. The designation is specific only when the period of natural aging is indicated.

T = thermally treated to produce stable tempers other than F, O, or H. This designation is applied to products which are thermally treated, with or without supplementary strain-hardening, to produce stable tempers.

The numbers following the H or T indicate the amount of strain hardening and the exact type of heat treatment used or any other special aspects that are associated with the processing of the alloy. For example, the high-strength Al alloy '7075-T6' contains Zn, Mg and Cu as major alloying elements and is characterized by a specific temper treatment 'T6' (solution heat-treated and then artificially aged) [ASM95].

2.5.1 Al-Si alloys

Al-Si is one of the widely used foundry alloys because of its good castability [Alu89a]. Apart from its lightweight, the low melting temperature of the alloy is an added advantage. Al-12Si alloy is one of the most important cast alloys among the family of the Al-Si alloys [Rag98a]. Al-Si exhibits a eutectic phase diagram with a eutectic temperature of 577°C at 12.6% Si (Fig. 2.5.1). At the eutectic temperature, both the Al and Si can form solid solutions with a maximum solubility limit of 1.65% Si in Al and 0.17% Al in Si [Van67a].

Both hypoeutectic and hypereutectic alloys show some response to heat treatment and the response can be improved by alloying with small percentages of Cu and Mg [Pol95a]. Rapid cooling of the Al-Si system refines the eutectic structure leading to a transition from the plate-like to rod-like form of Si in the eutectic mixture, even leading to a cellular microstructure at times [Bir07a]. The refinement of the Si phase can also be caused by small additions of external agents like Na or its salts in the melt state, which is often termed as an alloy modification process. Na either depresses the eutectic temperature or slows down the growth rate of Si by poisoning, causing the transition in the Si morphology leading to its

refinement ([Fre73a], [Wan00a]; [Wan00b]). Generally, a Si content of maximum 20% is used for both automobile and aerospace applications ([Fre06a], [Wan00a]) with alloy modifications carried out by the addition of external elements in to the melt. The advantage of Al-Si alloy is its high fluidity, imparted by the presence of Si, leading to better casting conditions. Al-Si alloys also possess very good weldability, corrosion and wear resistance combined with low thermal expansion coefficients ([Rag98a], [Nie10a], [Sae07a]).
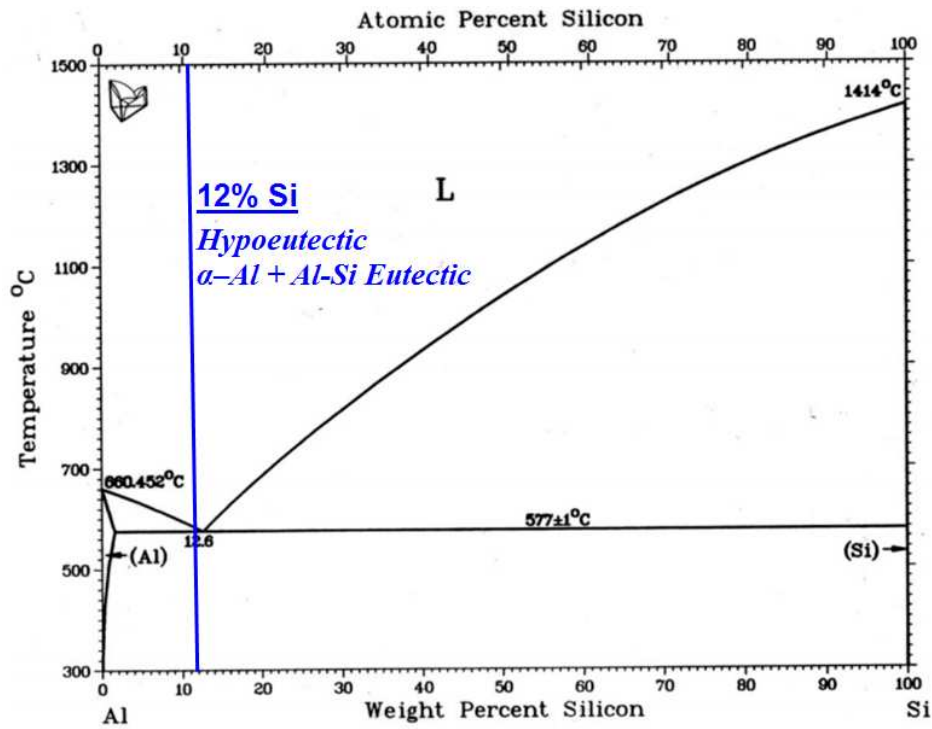
Fig. 2.5.1. Equilibrium phase diagram of Al-Si alloy with an eutectic reaction at 577ºC (after [Mur84a] and altered accordingly).

Aluminum castings have been widely used in the manufacture of various automobile parts such as pistons, cylinder liners, cylinder heads, intake manifolds and transmission parts like rear axle, differential housings etc. (Figs. 2.5.2 and 2.5.3). Daimler-Benz automotive engines use Al-Si alloys for the cylinder liners [Lea99a]. The manufacturing cycle for the cylinder liners includes the use of processes like spray forming, seamless tube extrusion etc. The latest trend is to use Al-Si as a key material for heavier parts like engine blocks. Replacing the heavier blocks made of cast iron with Al-Si results in (1) reducing the weight

of the engine, (2) reducing the fuel consumption, (3) reducing the hydro carbon emissions up to 30%, (4) increasing the power of the engine and its efficiency, (5) reducing friction and piston wear and (6) increasing the machinability and the recycling capability [Lea99a].
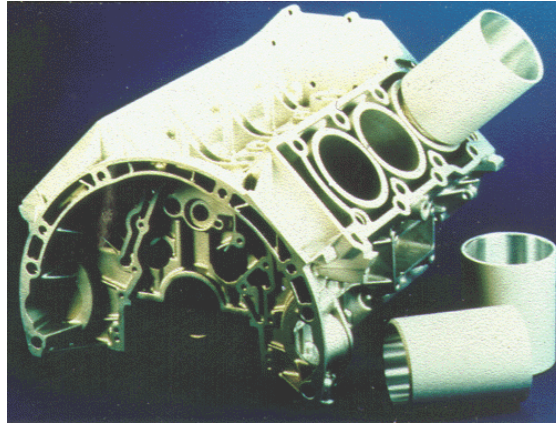
Fig. 2.5.2. A high-pressure die cast engine block with spray-formed Al/Si cylinder liners [Lea99a].

Fig. 2.5.3. Al-Si pistons connected to the crankshafts through a connecting rod [Caf10a].

The amount of Si in the Al-Si alloys decides the strength, hardness as well as the wear resistance of the pistons. Silicon also controls the thermal expansion coefficient of the piston, as the piston gets hotter during service and Al-Si alloys can be used up to 423 K – 473 K. Al-Si alloys may not be suited for high temperature applications because their mechanical properties, such as the tensile strength, show a significant drop in the temperature ranges of 573 K – 673 K [Lee00a].

The higher amount of Si present in hypereutectic Al-Si, leads to higher strength and hardness, minimizes the thermal expansion coefficient, but it decreases the ductility of the samples. However, the amount of Si has to be restricted to 20 wt.% or less since the presence of Si in high amounts makes it difficult to cast as well as to machine these alloys [Kam08a]. In addition, traces of other elements like Cu, Ni, Mg and Mn may be observed in the cast pistons and chasings in order to improve the overall mechanical behavior of the component. Owing to the above aspects, the cooling rate during solidification, alloying additions and the resultant properties like mechanical strength at room temperature as well as around the service temperatures of about 473 K and the tribological and corrosive properties are critical aspects for the Al-Si alloy processing and their applications.

Chapter 3: Sample preparation and characterization

3.1 Sample preparation

The present chapter deals with the various sample preparation and characterization techniques used in this thesis. This work is focused on the production of Al-12Si (wt.%) samples by SLM and, therefore, an extensive insight on the experimental details of the SLM process is given here. For comparison purposes, samples were also produced by copper mold casting. Consequently, some experimental details about the casting procedure are also given. This is followed by the methods used for phase and microstructural characterization, physical and mechanical investigations, tribological and corrosion tests and finally by the welding method used for joining the SLM parts.

3.1.1 Selective laser melting (SLM)

Spherical gas-atomized particles with size in the range 20 – 120 μm and a nominal composition Al-12Si (wt.%) were used as starting material for the SLM process. An SLM 250 HL device from SLM solutions with a build chamber of 250 mm × 250 mm × 250 mm was used for preparing the samples. The machine is equipped with an Yb-YAG-laser with a maximum power of 400 W and a beam diameter of ~ 80 μm. The SLM samples were prepared on an Al substrate plate. The parameters used for preparing the samples are: scanning speed 1455 mm/s for the volume and 1939 mm/s for the contour, power 320 W for the volume and the contour, layer thickness 50 µm and 73° rotating hatch style. High purity argon gas was used during SLM processing in order to avoid oxygen contamination. During the building process, the oxygen level was constantly measured by two sensors and was maintained below 200 ppm. The low concentration of oxygen is crucial as oxygen can react with the melt leading to embrittlement of the parts [Shi09a].

Tensile bars were prepared on the substrate plate. Forty-nine tensile bars were prepared each time with support structures placed between the tensile bars and the substrate plate in order to ensure good mechanical stability of the SLM parts and to guarantee adequate heat dissipation during processing. The effect of texture was investigated by producing

samples with different angle of inclination (γ = 30, 45, 60, 75 and 90°) with respect to the substrate plate. Heat treatment of the tensile bars was carried out under Argon atmosphere for 6 h at different temperatures (473, 573, 623, 673 and 723 K). In addition, hatch style variation was performed to estimate its influence on texture and mechanical properties (Fig. 3.1.1).

Single melt (SNM)   **Double melt (DM)**   **Single melt continuous (SMC)**   **Checker board (CB)**
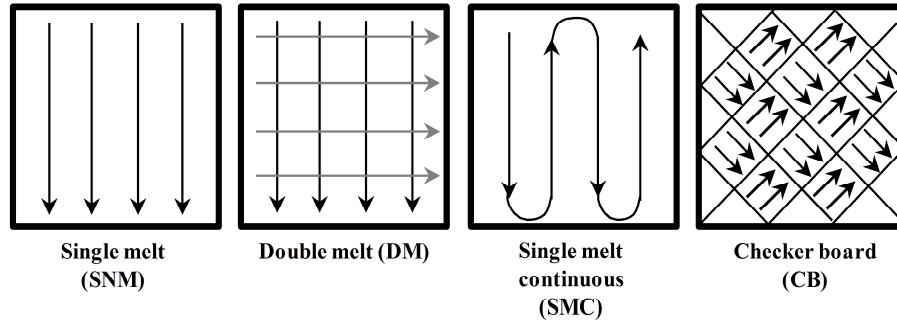
Fig. 3.1.1. The different hatch styles used in this work to evaluate the effects of texture and mechanical properties.

3.1.2 Casting

Cylindrical Al-12Si bulk samples with 8 mm diameter and 100 mm length were prepared by graphite mold casting in order to compare their microstructure and mechanical, tribological and corrosion properties with those characterizing the SLM samples. The mold is preheated to 673 K prior to casting, in order the limit the cooling rate as well as to avoid any residual porosity that may arise during the casting process. The melting chamber was constantly flushed under argon atmosphere to avoid oxidation in the melt and liquid and was heated to 973 K. For preparing tensile samples, the cast samples were machined accordingly.

3.2. Sample characterization: Phase and microstructural analysis

3.2.1 X-ray diffraction

Structural analysis was performed by X-ray diffraction (XRD) in reflection mode using a D3290 PANalytical X'pert PRO with Co-Kα radiation (λ = 0.17889 nm) in Bragg-Brentano configuration. The diffractometer is equipped with a secondary graphite

monochromator and a sample spinner and is operated at voltage and current of 40 kV and 40 mA, respectively. The diffraction was carried out with a step size of $\Delta(2\theta) = 0.05°$ and a typical counting time ranging between 15 and 60 s per step depending on the sample, where higher counting times were used for samples with small grain sizes. The Rietveld method was applied for the profile-fitting structure refinement in order to determine the structural parameters and the amount of free residual Si using the WinPlotR software package [Roi01a].

3.2.2 Optical microscopy (OM)

Optical microscopy was carried out using a VHX-2000 digital microscope from Keyence. The microscope is capable of magnifying the samples from 5 X until 1000 X using different objective lenses and is equipped with a built-in camera which is connected to a computer program with a VHX software, so that the images can be directly recorded and can be analyzed.

3.2.3 Scanning electron microscopy (SEM)

Microstructural analysis was performed using a high-resolution Gemini 1530 (Zeiss) SEM microscope with FEG-Schottky type source attached with an energy dispersive X-ray source (EDX) for elemental analysis. The EDX uses a Si(Li) detector and QUANTAX evaluation software from Bruker AXS. The microstructure of the Al-12Si samples were obtained using back scattered electrons, due to low chemical contrast between the phases Al and Si. However, for the fracture surfaces, wear scars and corroded surface analysis, secondary electrons were used to take the advantage of the large depth of focus. The operating parameters used are EHT – 5 kV, WD ~ 10 mm and aperture – 60 / 120 μm. The SEM images were used to determine the matrix ligament size (λ) of the Al matrix. 'λ' was measured by superposing several random lines on the SEM micrographs and its value was estimated from the number of matrix region intercepts per unit length of test line 'N' and the total length of the matrix (L) as $\lambda = L/N$ ([Und85a], [Scu09a]). At least ten lines were drawn in three different images and the average value is taken as the matrix ligament size 'λ'. The

microstructural features (size and density of the Si particles, dimple size etc.) characterizing the different samples before and after tensile tests were quantified from the SEM images using the *Image J* software [Ima13a]. At least three different images were used for the measurements.

3.3 Characterization of physical and mechanical properties

3.3.1 Density

The density of the samples was calculated by the Archimedes principle. The samples were first weighed in air and then immersed in distilled water, kept in water for adequate time before they were weighted again. A Mettler Toledo AX205 analytical balance with the smallest increment of 0.001 mg was employed for the density measurement. The instrument takes care of the temperature effect during the density measurement.

3.3.2 Microhardness

The microhardness measurements were carried out using a computer-controlled HMV Shimadzu Vickers hardness testing machine which is equipped with a diamond indenter in the form of a pyramid with square base with an angle of 136° between the opposite faces. A load of 0.098 N was applied for 10 sec during each measurement. The length of the imprints along the diagonal was used to calculate the hardness of the samples using a digital video measuring system. For the microhardness indentation measurements, the samples were embedded in an epoxy resin and the surface to be measured were carefully grinded (until 4000 grit paper) and polished with diamond paste (particle size < 0.25 µm). The hardness values observed is an average of more than 25 indentations in each sample.

3.3.3 Tensile test

The room temperature uni-axial tensile tests were carried out using an INSTRON 5869 testing facility under quasistatic loading with a strain rate of 1×10^{-4} 1/s. A laser extensometer from Fiedler Optoelektronik GmbH, Germany, was used to measure the strain

directly on the samples. The dimensions of the cylindrical samples used for the tensile tests are shown in Fig. 3.3.1, where, d_o = 3 mm (gauge length), d_1 = 4 mm, L_o = 17.5 mm, L_c = 21 mm, h ≥ 13 mm and L_t = 52 mm. At least three tensile samples were tested in each condition to ensure the reproducibility of the results.
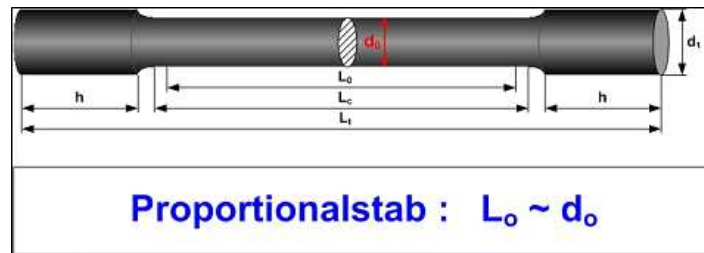
Fig. 3.3.1. Schematics of the sample used for the tensile tests.

3.3.4 High temperature tensile test

The temperature of Al-12Si automobile components like pistons and crankshafts may rise up to ~ 473 K during service conditions. Hence, the Al-12Si SLM and cast samples were tested under tensile conditions at different temperatures (373, 423 and 573 K). The Al-12Si SLM samples show structural changes when heated at high temperatures and, therefore, to avoid any structural changes during the tensile tests, the samples were annealed at 573 K before the mechanical tests. High temperature tensile testes were carried out using INSTRON 8502 with a strain rate of 1×10^{-4} 1/s. Cylindrical samples with the same proportions shown in Fig. 3.3.1 were used: the diameter was 4 mm along the gauge length and the diameter at the grips was 5 mm. Other dimensions are adjusted according to the gauge length of the sample.

3.4 Tribological properties

3.4.1 Sliding wear test

Sliding wear tests were carried out according to the ASTM G 99-05 [AST10a] standard at room temperature and in ambient atmospheric conditions using a pin-on-disc test device as shown in Fig. 3.4.1. A disc of 45 mm diameter and 13 mm thickness made of hard-

faced stainless steel is used against the Al-12Si flat head pins of 9 mm in diameter and 12 mm in height, as shown in Fig. 3.4.1. The edges of the pin were polished to 4000 grit paper to have a plane parallel surface. The tests were performed continuously at a constant load of 10 N with a sliding speed of 1 m/s for 30 min.

The wear rate was evaluated by [Pra11a]

$$Q_s = \frac{V_s}{L_s} \qquad , \qquad (3.4.1)$$

where Q_s is the wear rate, L_s the sliding distance, V_s the sliding volume loss and the subscript s indicates sliding. The volume loss was calculated from the wear loss determined by measuring the weight of the flat head pins before and after tests. The sliding distance is given by $L_s = 2\pi r_s v_s t_s$, where r_s is the radius of the wear track (22.5 mm), v_s is the speed expressed in rounds per minutes (450 rpm) and t_s is the time (30 min). Wear scars were analyzed using SEM to evaluate the wear mechanisms operating in these samples.
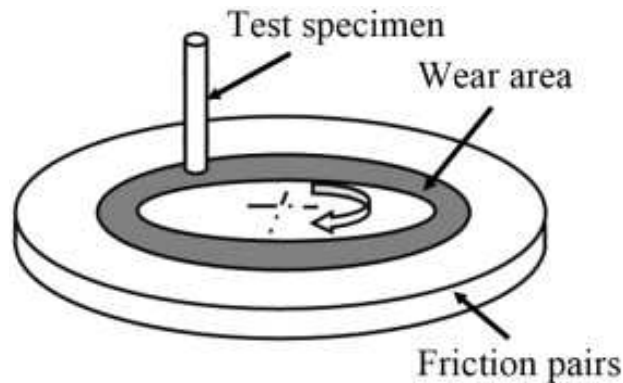
Fig. 3.4.1. Pin-on-disc sample setup showing both test specimen (pin) and counterface (disc) [Kan12a].

The sliding wear tests were carried out at Department of Metallurgical and Materials Engineering, Indian Institute of Technology – Madras, India with the help of Prof. M. Kamaraj.

3.4.2. Fretting wear test
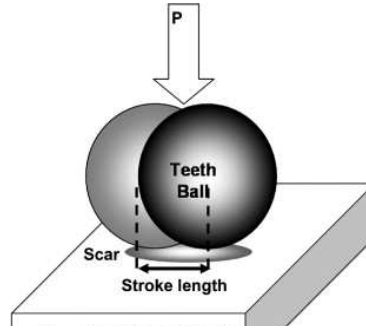
Fig. 3.4.2. Schematic illustration of fretting wear [Roy08a].

Fretting wear is defined as the repeated cyclical rubbing between two surfaces (fretting) over a period, which will remove material from one or both surfaces that are in contact between each other. Fretting wear tests were carried out using an OPTIMOL SRV, Germany device according to the ASTM-D5706-97 and ASTM-D5707-97 standards ([AST97a], [AST97b]). A steel ball (G-Cr 15) with a diameter of 10 mm is impended against a disk type fretting wear test rig (Al-12Si) with a point contact mode in this study as shown in Fig. 3.4.2. The disc used in the present case is Al-12Si with a diameter of 10 mm and 25 mm in height. The fretting wear test can be carried out with different types of strategies, as shown in Fig. 3.4.3. However, a torsional contact with an angle of α = 0° is used in the present set of experiments. A pre-load of 5 N for 30 s is applied over the ball against the Al-12Si disc after which the test was carried out at a load of 10 N for 30 min with a frequency of 50 Hz and a half-amplitude of 100 µm.

The fretting wear volume was evaluated by [Ell02a]

$$V_f = h^2(3R_f - h)/3 \qquad , \qquad (3.4.2)$$

where V_f is the volume loss, h is depth of the fretting scar and the subscript f indicates fretting. R_f is equal to $(T^2 + h^2)/2h$ and $T = (d_1 \times d_2)^{-0.5}/2$, where d_1 and d_2 are the principal diameters of the wear surface that take into account any deviation from perfect circular shape of the fretting scar. The wear surfaces of the samples after sliding and fretting wear tests were characterized by OM and SEM.
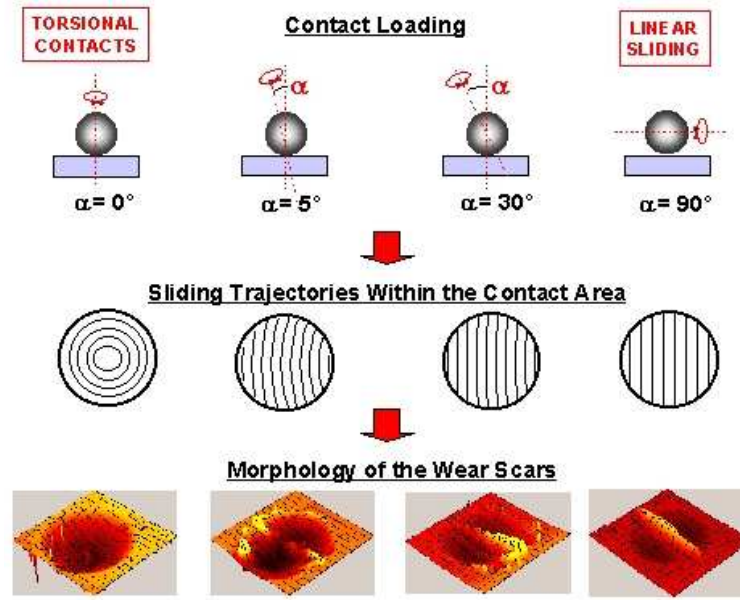
Fig. 3.4.3. Different strategies that can be utilized in a fretting wear test [Bri00a].

The fretting wear tests were carried out at the school of Mechanical and Automotive Engineering, South China University of Technology, China with the help of Prof. Z.Z. Wang.

3.5 Chemical properties

3.5.1 Corrosion behavior

Samples with dimension 3 mm × 3 mm × 2 mm were used for the weight-loss corrosion experiments. The samples were polished using SiC paper from 400 down to 4000 grit and subsequently polished using 3 μm and 0.25 μm diamond suspensions. The samples were cleaned with ethanol and the initial weight as well as the dimensions of the samples was measured. The samples were then immersed in 0.01 M, 0.1 M and 1 M HNO_3 solutions. The samples removed from the acidic solution every 24 h, subsequently rinsed with distilled water and dried in hot air. The samples were then weighted, and re-immersed in the acidic solution again for additional 24 h. The corrosion products were not removed intentionally at any of the intermediate stages. They were removed only after the last measurement for microscopic investigations. A Mettler Toledo AX205 analytical balance with the smallest increment of 0.01 mg was employed for all the weight measurements. Three independent

trials were conducted under similar conditions and the results presented here were determined by statistical analysis over the three experiments.

3.6 Welding properties

3.6.1 Continuous drive friction welding

Continuous drive friction welding (FW) is a class of solid-state welding process that utilizes the heat generated through mechanical friction to fuse materials together. The components used during the FW process can be of the same or dissimilar materials [Maa08a].

1. Motor
2. Brake
3. Rotating Chuck
4. Non Rotating Chuck
5. Rotating Workpiece
6. Non Rotating Workpiece
7. Hydraulic Cylinder
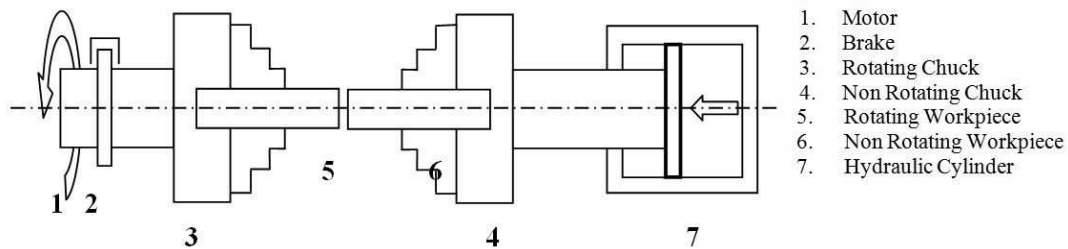
Fig. 3.6.1. Layout of a continuous drive friction welding process [Sah12a].

FW was carried out in a continuous drive friction-welding machine with 200 kN capacity. In a continuous drive friction welding method (Fig. 3.6.1) one of the two components is held stationary and the other component is rotated at a constant speed. The two components are brought together under an axial pressure P_f for a definite time called friction time t_f. The clutch is then separated from the drive, and the rotary component is brought to stop within the breaking time while the axial pressure on the stationary part is increased to upset pressure P_u for a definite upset time t_u. The parameter sequence used in a conventional continuous drive FW process is shown in Fig. 3.6.2. Surface preparation of the samples need considerable attention, since the joint strength of the sample is influenced by the surface impurities ([Yil95a], [Has87a]). The surface of the sample faces was carefully polished before welding to produce a smooth oxide free surface, but also to ensure

perpendicularity, which is very important in achieving sound welds. The important process parameters used in the present study are summarized in Table 3.6.1.
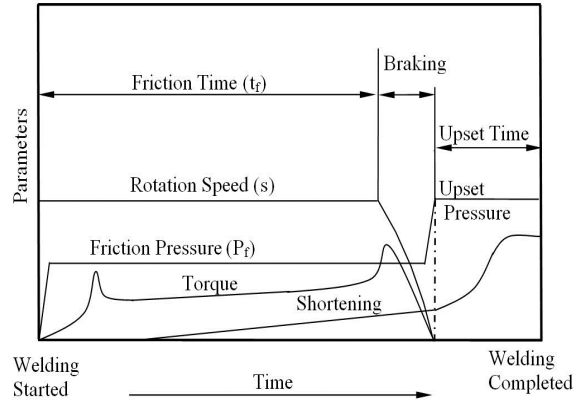
Fig. 3.6.2. Parameters for a continuous drive friction welding process [Sah12a].

Table 3.6.1. Continuous drive friction welding process parameters used in this work.

Friction pressure	*75 MPa*
Upset pressure	*100 MPa*
Burn-off length	*3 mm*
Spindle speed	*1000 rpm*

The flash generated during the FW process was then removed by machining and tensile samples were drilled from the FW rods.

The friction welding tests were carried out at Department of Metallurgical and Materials Engineering, Indian Institute of Technology – Madras, India with the help of Prof. G. Phanikumar.

Chapter 4: Microstructure and mechanical properties of Al-12Si produced by SLM: Effect of heat treatment

This chapter presents the results on the production of Al-12Si samples by SLM followed by detailed phase analysis, microstructural characterization and evaluation of the mechanical properties through hardness and room temperature tensile tests and their comparison with the corresponding cast sample. The effect of annealing at different temperatures on microstructure and resulting mechanical properties of the SLM parts is systematically discussed by analyzing size, morphology and distribution of the phases as a function of temperature. In addition, the high temperature mechanical properties of the SLM are presented. Finally, the variation of the hatch style during SLM processing and its effects on texture and mechanical properties are discussed.

4.1 Al-12Si processing

4.1.1 Characterization of SLM parts

Fig. 4.1.1 shows the OM, SEM and EDX images of the microstructure viewed along the cross-section of the Al-12Si samples prepared by SLM with angle of inclination $\gamma = 90°$ (i.e. perpendicular to the substrate plate). The microstructure is not uniform throughout the material (Fig. 4.1.1(a)), but it displays the typical laser tracks of SLM processing ([XSu12a], [Thi13a]). The tracks consist of large regions with circular cellular morphology (Fig. 4.1.1(b-c)) separated by thin boundaries with elongated columnar morphology (dashed line in Fig. 4.1.1(c)). Such a microstructure is significantly different with respect to the corresponding Al-12Si samples produced by casting. The cast sample displays a continuous eutectic structure of Al and Si along with dispersed primary α-Al (Fig. 4.1.2) characteristic of hypoeutectic compositions, in accordance with Suárez-Peña et al. [Suá06a] for Al-12Si alloys.

The boundaries in Fig. 4.1.1 correspond to regions where two different laser tracks are overlapped (i.e. the hatch overlaps), which are therefore melted two times. The cellular structure in the track cores, which experiences a single melting step, becomes finer as we

move away from the re-melted boundaries. EDX compositional analysis of the cellular structure (Fig. 4.1.1(d-f)) reveals that Si is preferentially located at the cellular boundaries, which have thickness of about 200 nm. On the other hand, the cellular morphology is rich in Al and displays a size of about 500 – 1000 nm. Such a fine microstructure has been reported for melt-spun Al-12Si ribbons [Bir07a] and can be ascribed to the high cooling rate characterizing the SLM process.
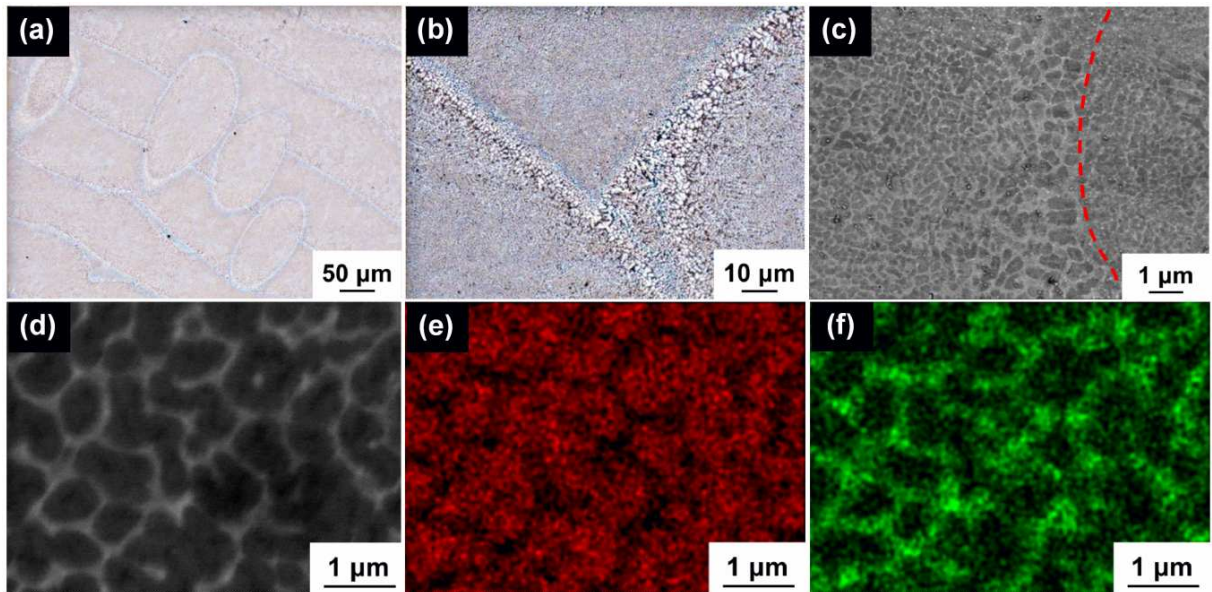
Fig. 4.1.1. Microstructure of the Al-12Si samples prepared by SLM with angle of inclination $\gamma = 90°$ (i.e. perpendicular to the substrate plate): (a and b) OM and (c and d) SEM micrographs, and (e and f) EDX composition maps.

The formation of a cellular structure requires the presence of a minimum of constitutional undercooling [Sin03a]. The solute concentration in the liquid has to be minimized and combined with an extremely high velocity of the solidification front [Sin03a]. However, during solidification of the Al-12Si, the solidifying front rejects Si into the liquid. Hence, the solute concentration in the liquid raises as the solidification front moves. In addition, the solubility of Si in Al decreases with decreasing temperature [Bos73a]. For example, in case of the Al-Si eutectic composition, the solubility of Si in Al is 1.65 wt.% at the eutectic temperature (850 K), and it decreases to 0.06 wt.% at 573 K [Bos73a]. The solubility of Si in Al can be extended by using processing routes involving high cooling rates

([Bir07a], [Bos73a], [Tod92a], [Uzu01a]). Assuming that the solubility of Si in Al is extended, the amount of Si rejected in the liquid is reduced, consequently decreasing the solute concentration in the liquid as well as the degree of constitutional undercooling. Under such circumstances, the formation of a cellular structure is preferred and is observed in the Al-12Si prepared by SLM. Since the process of cellular solidification in the present system is kinetically favored, α-Al solidifies first in a cellular morphology as a result of the high cooling rate and of the extended solubility of Si. The residual Si is then segregates along the cellular boundaries, as observed in Fig. 4.1.1(d-f).
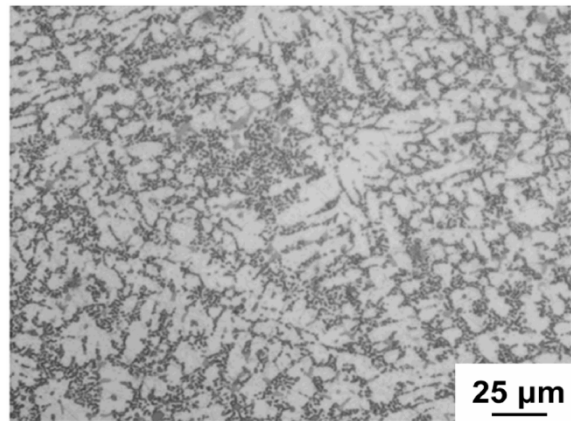
Fig. 4.1.2. OM micrograph of the Al-12Si samples prepared by casting.

The XRD pattern of the Al-12Si alloy prepared by SLM (Fig. 4.1.3(a)) shows the typical diffraction peaks of Al and Si. However, the intensity of the Al (111) and (200) peaks is reversed with respect to the same material produced by casting, implying the presence of texture in the SLM sample. In addition, the intensity of the Si peaks is rather weak, which suggests that a reduced amount of "free" Si is present in the material. This can be attributed primarily to the extended solid solubility of Si in α-Al: cellular morphology resulting from the high cooling rates observed during the SLM process [Ben09a]. The Si peaks are broad, which points to a reduced size of the Si phase. These observations have been corroborated by Rietveld peak fitting analysis [Rie69a] carried out on the XRD pattern of the SLM sample. The lattice parameter of Al is 4.0508 nm and the amount of free residual Si is ~ 1 wt.%. This confirms that the solid solubility of Si in Al can be extended by SLM processing, as already

reported by other researchers in processes involving high cooling rates ([Bir07a], [Bos73a], [Tod92a], [Uzu01a]). Finally, the crystallite size of Al and Si were found to be 118 and 8 nm, respectively, in agreement with the extremely broad diffraction peaks observed in Fig. 4.1.3(a). On the other hand, the cast sample displays an Al lattice parameter of 4.0522 nm and an amount of free residual Si of ~ 10 wt.%, in agreement with the limited solid solubility of Si achievable by conventional casting [Sou11a].
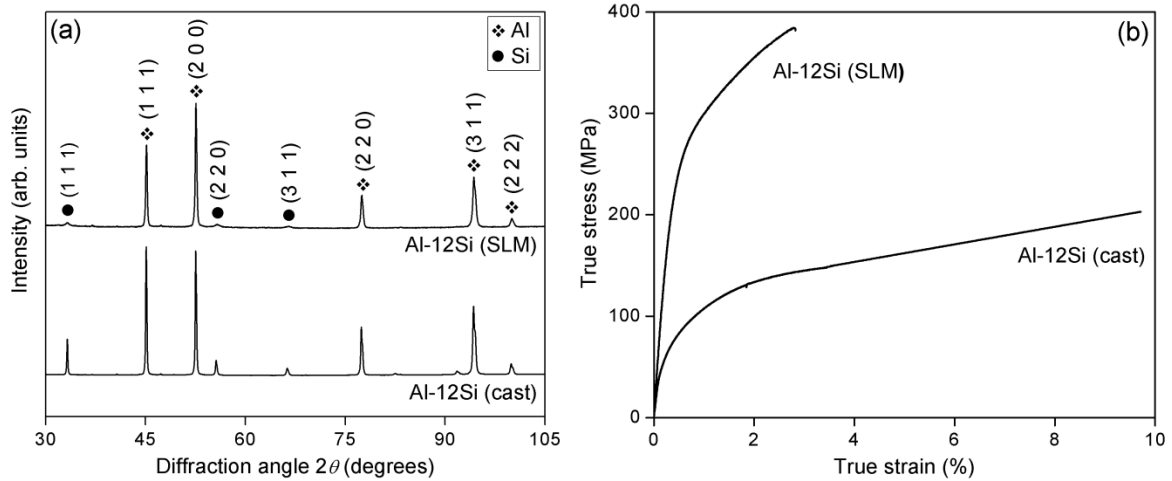
Fig. 4.1.3. (a) XRD patterns (λ = 0.17889 nm) and (b) room temperature tensile tests of the cast and as-prepared SLM Al-12Si samples.

The relative densities of the samples, measured before the tensile tests, were found to be 99.5 % ± 0.1 % for the SLM samples and 99 % ± 0.5 % for the cast samples. Fig. 4.1.3(b) shows the room temperature tensile stress-strain curves of the Al-12Si specimens prepared by SLM and by casting. The yield strength (0.2% offset) of the cast sample is ~ 60 MPa, in accordance with the results of Soumyajit et al. [Sou11a]. The strength of the cast sample increases with increasing strain up to about 200 MPa, where fracture occurs at ~ 9.5 % strain. The SLM samples display yield and tensile strengths of about 260 and 380 MPa, which are respectively four and two times higher than the corresponding values of the cast material. Such an increase of strength occurs at the expenses of the fracture strain, which is only ~ 3%; therefore significantly decreased compared to the cast sample. Such high strength and decreased ductility of the SLM samples may be attributed to the following factors: (*1*)

presence of texture, as observed in Fig. 4.1.3(a) or (*2*) microstructural effects (e.g. morphology, size and distribution of the Al and Si phases). In the following, the effect of these factors will be analyzed and discussed in detail.

4.1.2 Effect of texture

The presence of texture in the SLM samples can be ascribed to the additive manufacturing processing that takes place layer-by-layer and to the resulting cooling conditions. The (200) and (111) planes of α-Al are the planes showing texture in the Al-12Si prepared by SLM (Fig. 4.1.3(a)). The (111) plane is more densely packed than the (200). The columnar grains tend to orient towards the (200) plane, since the [100] direction is usually parallel to the long axis of the columnar grains [HHu74a]. Moreover, the [100] direction is perpendicular to the mold wall [Suw08a] and all other crystallographic axes are randomly oriented around the [100] direction. Hence, preferential orientation along the [100] direction, commonly known as fiber textures, is generally observed when the material solidifies as columnar grains ([HHu74a], [Suw08a]). In contrast, columnar growth along the [111] direction would require the growth to be against the plane, which makes such orientations difficult, especially for high cooling rates.

The texture in the SLM samples along the tensile loading direction can be altered by changing the scanning strategy [Thi13a] or by building the samples with certain angles to the substrate plate [Bra12a]. The latter strategy is used in this work. For this, tensile specimens were prepared by SLM with an inclination angle γ varying between 90 and 30° (see Fig. 4.1.4(a)). The samples built with different angles of inclination were investigated by XRD (Fig. 4.1.4(b)) and the extent of texture of the Al (111) and (200) planes was quantified in the different samples using the texture coefficient, which is given by [Mar11a]

$$T_c(hkl) = \frac{I(hkl) / I_o(hkl)}{(1/N)\left[\sum_N I(hkl) / I_o(hkl)\right]} \quad , \quad (4.1.1)$$

where T_c(hkl) is the texture coefficient of the (hkl) plane, I is the measured intensity, I_o is the standard intensity from reference and N is the number of diffraction peaks. T_c is close to unity for a randomly distributed powder samples, while T_c departs from unity when the (hkl) plane is preferentially oriented. Fig. 4.1.4(c) shows the texture coefficients of the (111) and (200) planes as a function of the inclination angle γ. The texture coefficient of both the (111) and (200) planes tends to approach unity with decreasing γ from 90 to 30º. This indicates that the texture along the tensile direction can be varied by properly changing the inclination angle γ.
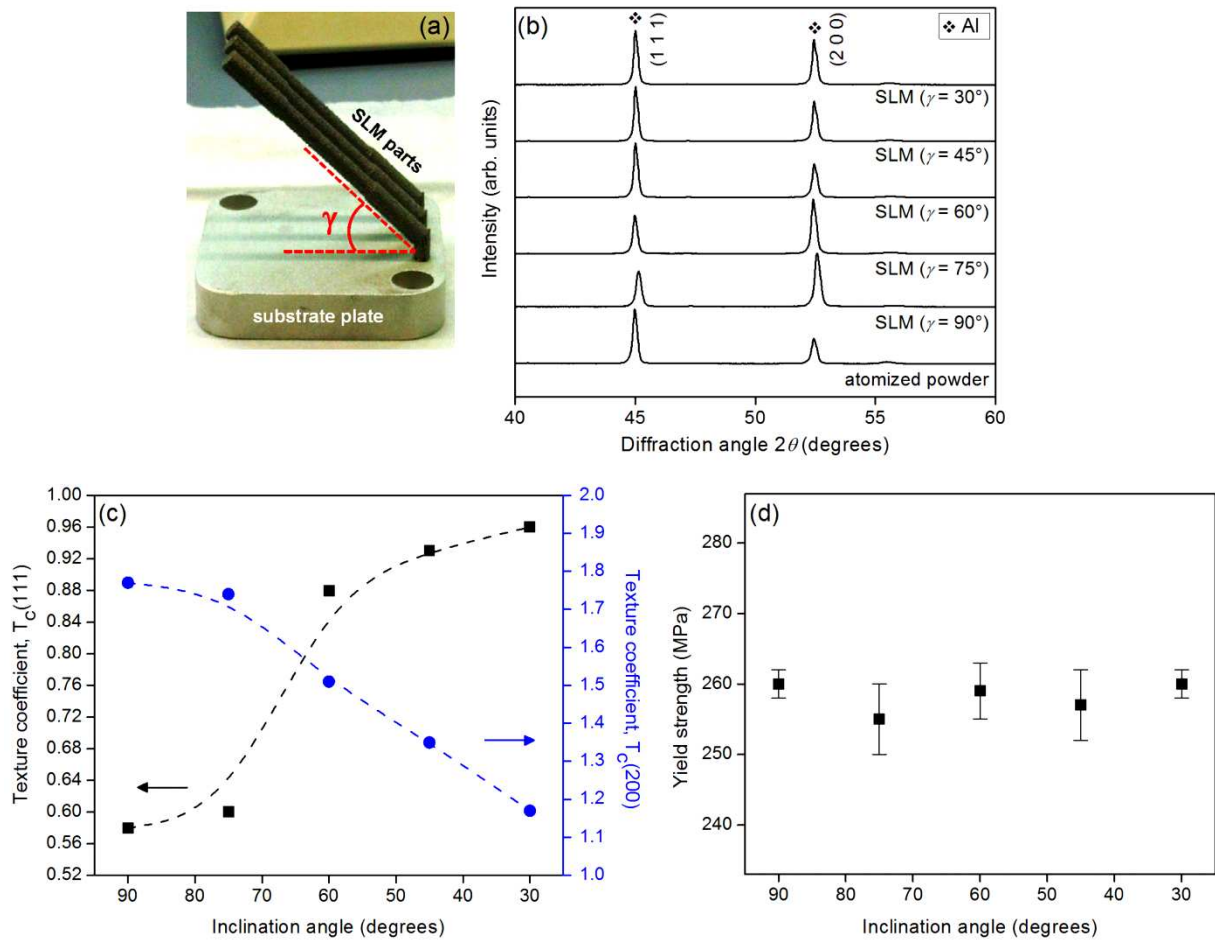
Fig. 4.1.4. (a) Inclination angle γ between SLM specimens and substrate plate, (b) XRD patterns ($\lambda =$ 0.17889 nm) for the Al-12Si samples prepared by SLM with γ varying between 90 and 30°, (c) texture coefficient of the Al (111) and (200) planes quantified using Eq. (4.1.1) and (d) yield strength (0.2% offset) of the SLM samples as a function of γ.

In order to analyze the effect of texture on the mechanical properties of the SLM samples, the samples built with different inclination angles were tested at room temperature under tensile loading. The yield strength (0.2% offset) of the samples ranges between 255 ± 5 to 260 ± 5 MPa (Fig. 4.1.4(d)), which indicates that the effect of texture on the strength of the samples is negligible and can be ruled out.

4.1.3 Effect of heat treatment

In order to evaluate the effect of the microstructure on the mechanical behavior of the samples, the SLM specimens produced with inclination angle $\gamma = 90°$ were isothermally annealed for 6 h at temperatures between 473 and 723 K. The XRD patterns of the heat-treated samples are shown in Fig. 4.1.5(a) and the corresponding structural data obtained by Rietveld structure refinement are presented in Fig. 4.1.5(b-c). The results reveal that the crystallite sizes of Al and Si increases from 118 and 8 nm for the as-prepared SLM material to 218 and 142 nm for the SLM samples annealed at 723 K (Fig. 4.1.5(b)). The lattice parameter of α-Al (Fig. 4.1.5(c)) increases from 4.05079 nm for the as-prepared SLM samples to 4.05225 nm for the sample heat-treated at 723 K. Similar results have been reported by Bose et al. [Bos73a], who observed for rapidly solidified Al-Si ribbons the increase of the lattice parameter with increasing annealing temperature. At the same time, the amount of free Si increases from about 1 wt.% for the as-prepared SLM samples to 8 wt.% for the material annealed at 723 K. This indicates that Si is rejected from the Al lattice with increasing annealing temperature and explains the corresponding increase of the lattice parameter of α-Al.

The mechanical properties of the annealed samples were investigated by room temperature tensile tests (Fig. 4.1.6(a)) and the results are summarized in Fig. 4.1.6(b). The yield and fracture strengths of the material decreases with increasing the annealing temperature. For example, the yield strength decreases from 260 MPa for the as-prepared SLM samples to 95 MPa for the samples heat-treated at 723 K. In contrast, the fracture strain remarkably increases in the same temperature range from ~ 3 to 15 %. Such a variation in the mechanical properties arises from the changes in the microstructure of the material, as it will be explained later.
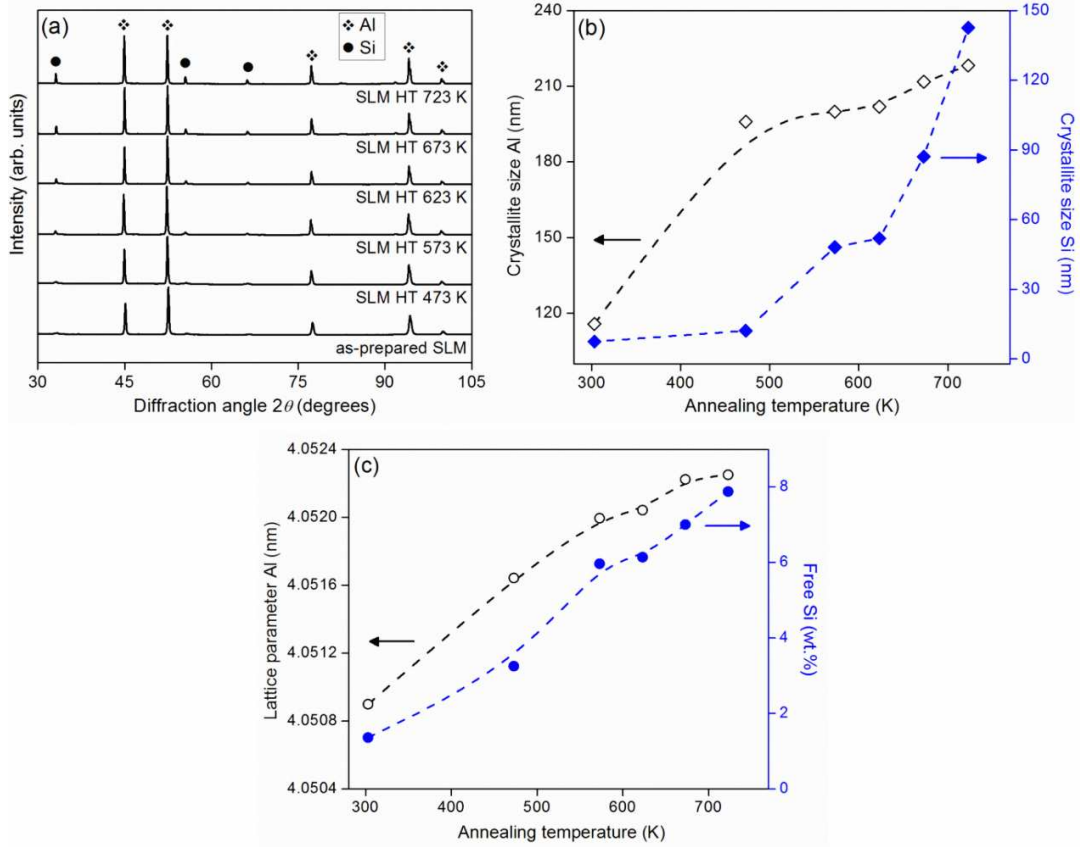
Fig. 4.1.5. (a) XRD patterns ($\lambda = 0.17889$ nm) of the Al-12Si SLM specimens ($\gamma = 90°$) isothermally annealed for 6 h at temperatures between 473 and 723 K, (b) crystallite size of Al and Si, and (c) lattice parameter of Al and free Si versus the annealing temperature.
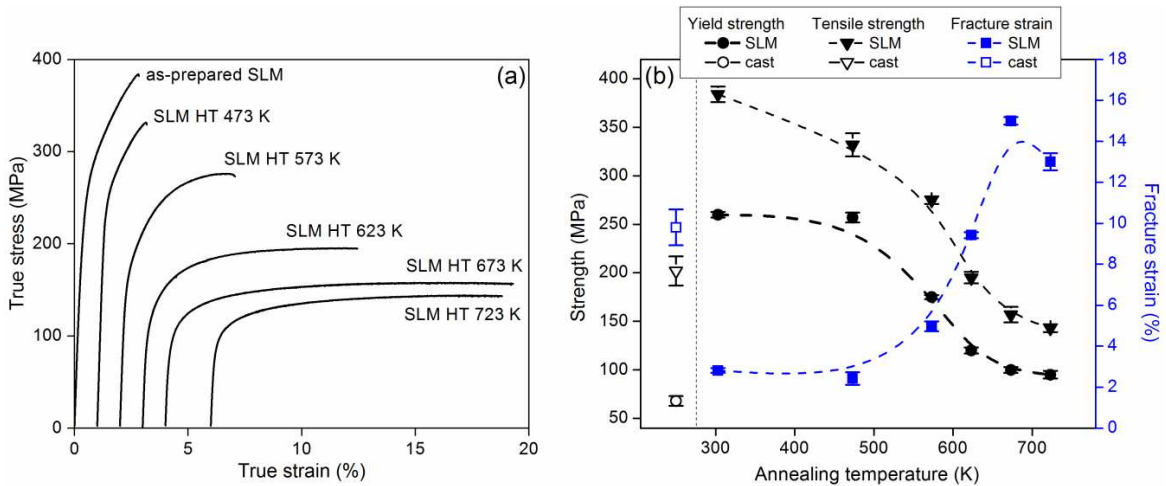
Fig. 4.1.6. (a) Room temperature tensile test curves of the SLM samples ($\gamma = 90°$) annealed at different temperatures and (b) corresponding mechanical data.

The effect of annealing on the microstructure of the SLM samples is shown in Fig. 4.1.7. The OM (Fig. 4.1.7(a-d)) and SEM (Fig. 4.1.7(e-h)) micrographs reveal that, compared to the as-prepared SLM material (Fig. 4.1.1), the microstructure becomes coarser with increasing the annealing temperature from 473 to 723 K, corroborating the results from XRD (Fig. 4.1.5). More specifically, the Si particles tend to agglomerate along the cellular boundaries and hatch overlaps, and their size grows continuously with increasing annealing temperature. Size and distribution of the Si particles in the SLM samples ($\gamma = 90°$) as a function of the annealing temperature was quantified for both hatch overlaps and track cores by image analysis of the OM and SEM micrographs.
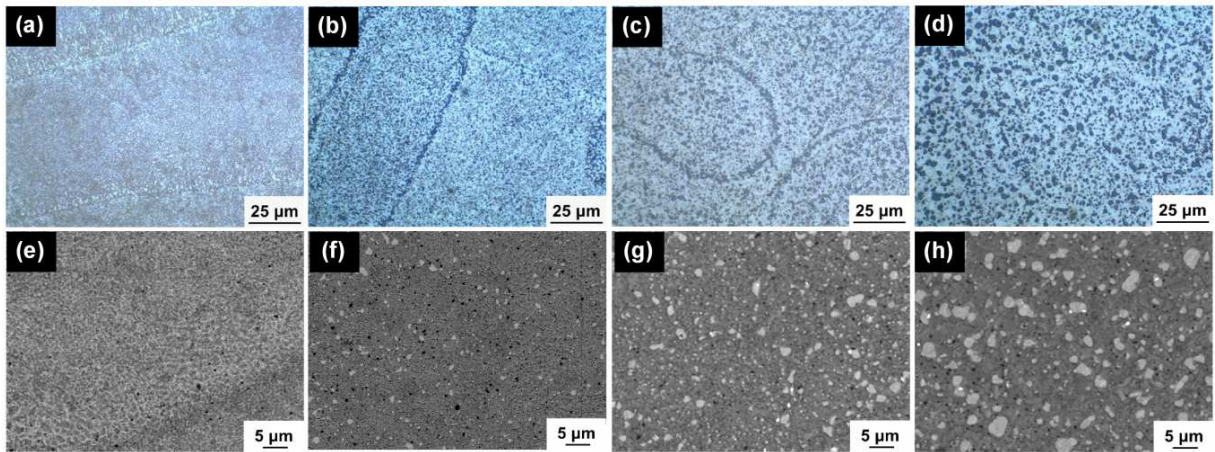
Fig. 4.1.7. OM and SEM micrographs of the SLM samples ($\gamma = 90°$) isothermally annealed for 6 h at (a and e) 473, (b and f) 573, (c and g) 673 and (d and h) 723 K.

The results, summarized in Fig. 4.1.8, shows that the average size of the Si particles increases exponentially with increasing the annealing temperature in both hatch overlaps and track cores. However, the size of the particles in the hatch overlaps is constantly larger than in the track cores. Another peculiar aspect characterizing the heat-treated samples is the heterogeneous distribution of the Si particles. The amount of Si particles along the hatch overlaps varies from 7 particles/μm^2 for the sample annealed at 473 K to 0.3 particles/μm^2 for the 723 K heat-treated sample (Fig. 4.1.8). Away from the hatch overlaps, in the track cores, the density of Si particle decreases in the same temperature range from 3 to 0.1 particles/μm^2. The decrease of the particle density with increasing annealing temperature can

be easily understood by considering the growth of the particle size as the result of the agglomeration of smaller particles. On the other hand, the reason for the heterogeneous distribution of the particles is less clear but it is most likely due to the double melting characterizing the hatch overlaps, which represents an additional, localized heat treatment, which would provide further potential for growth and agglomeration of the Si particles with respect to the track cores.
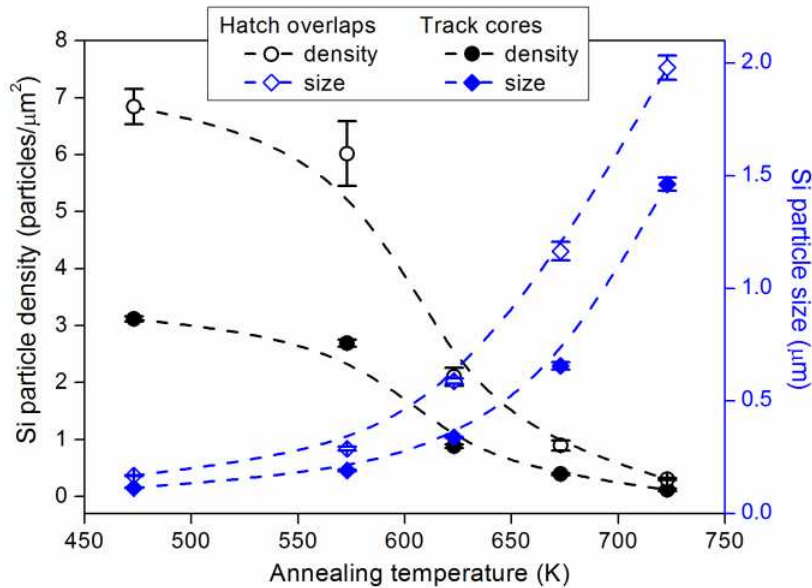
Fig. 4.1.8. Size, density and distribution of the Si particles for the SLM parts ($\gamma = 90°$) as a function of the annealing temperature quantified for both hatch overlaps and track cores by image analysis of the OM and SEM micrographs.

With this in mind, it is possible to describe schematically the microstructure evolution of the SLM samples during annealing (Fig. 4.1.9). As discussed earlier, the as-prepared SLM material displays a microstructure consisting of supersaturated Al with cellular morphology along with Si-rich areas in the cellular boundaries (red features in Fig. 4.1.9). At low annealing temperatures (473 and 573 K), Si is rejected from the supersaturated Al to form small Si particles. At this stage, the Si-rich cellular boundaries do not disappear completely. With increasing the annealing temperature, the Si particles grow, their number decreases significantly and finally the cellular boundaries are no longer visible. The density and the size of the Si particles are larger along the hatch overlaps than in the track cores, leading to a

57

composite-type microstructure consisting of soft α-Al regions reinforced with small Si particles (i.e. the track cores) surrounded by areas with a higher density of larger Si particles (i.e. the hatch overlaps).
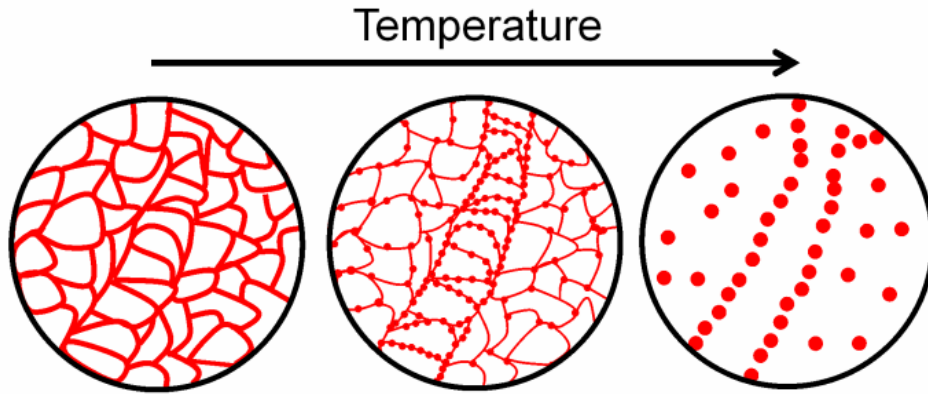
Fig. 4.1.9. Schematic description of the microstructure evolution of the SLM samples during annealing. Red features represent Si-rich areas.

The analysis of the microstructures shown in Fig. 4.1.7 permits to rationalize the fracture morphology of the different samples. Fig. 4.1.10 shows the fracture surface of the cast, as-prepared SLM ($\gamma = 90°$) and heat-treated (723 K) samples after room temperature tensile tests. The fracture surface of the cast samples (Fig. 4.1.10(a)) is rather irregular and does not apparently results from the eutectic microstructural features. The surface displays dimples (Fig. 4.1.10(b)), typical of a ductile behavior, along with cleaved and fractured Si particles (indicated by arrows in Fig. 4.1.10(b-c)). On the other hand, the fracture surface of the as-prepared SLM samples (Fig. 4.1.10(d)) shows a step-like morphology that resembles the microstructure observed in Fig. 4.1.1. Most likely, the fracture propagates through the hatch overlaps where the density and size of the brittle Si phase is higher. The size of the dimples is significantly decreased in the as-prepared SLM sample (Fig. 4.1.10(e)) with respect to the cast material.

No Si particles are observed, even at high magnifications (Fig. 4.1.10(e)), corroborating the results from XRD, where the crystallite size of the Si phase is in the nano-regime and the amount of residual free Si is only ~ 1 wt.%. The fracture surface of the heat-

treated samples (Fig. 4.1.10(g)) also displays a step-like morphology. The average step size is ~ 84 μm, which corresponds to the size of the laser tracks and suggests that the excess Si along the hatch overlaps acts as preferential sites for failure. The dimple size of the heat treated sample is about 6 μm (Fig. 4.1.10(h)), therefore larger than the as-prepared SLM samples (0.4 μm). Fractured Si particles are often observed at the ends of the dimples (marked by arrows in Fig. 4.1.10(i)) and no decohesion of the Si particle from the matrix is observed, indicating good bonding between the Al matrix and the Si particles.
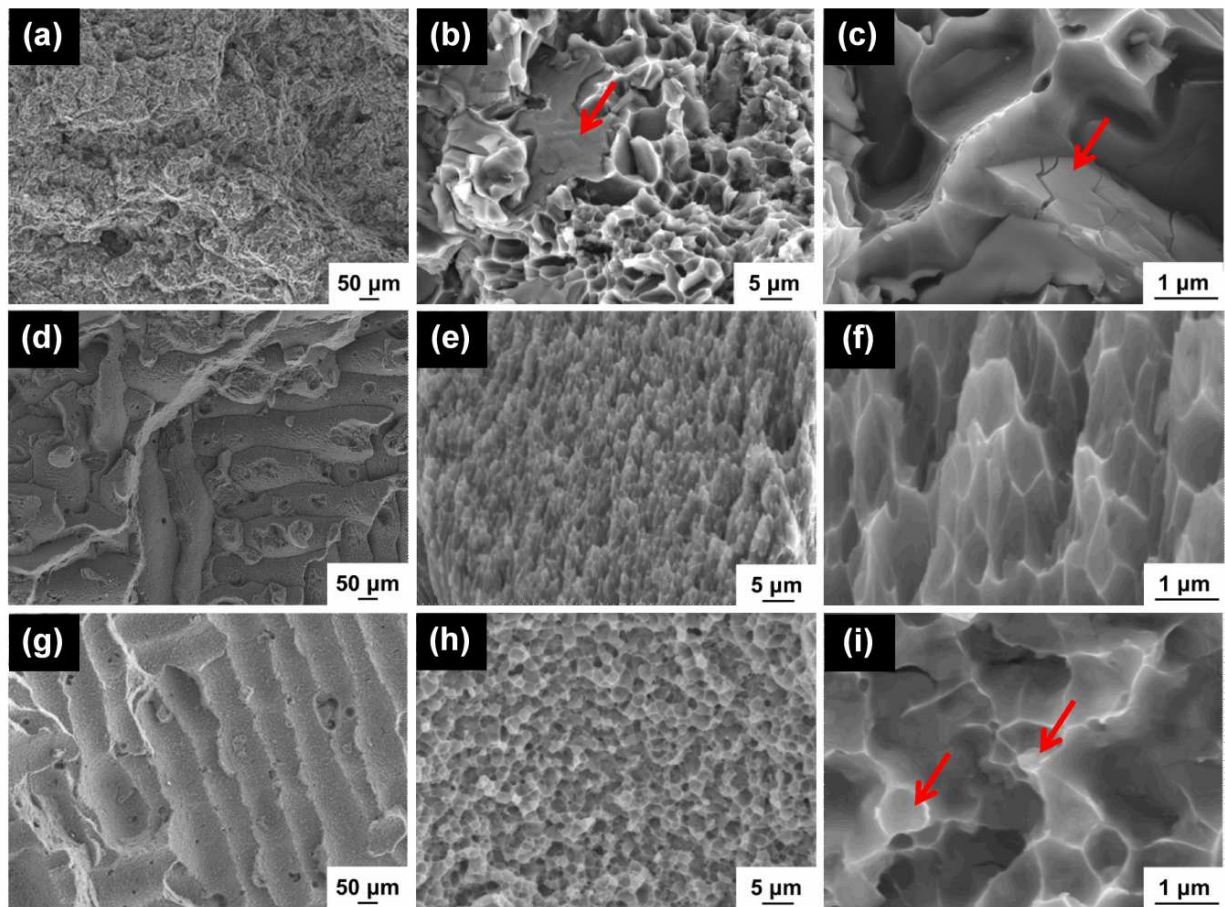
Fig. 4.1.10. Fracture morphology of the (a – c) cast, (d – f) as-prepared SLM ($\gamma = 90°$) and (g – i) heat-treated (723 K) samples after room temperature tensile tests.

Fig. 4.1.11 presents the schematic illustration showing the crack propagation path. As discussed earlier, the hatch overlaps with elongated longitudinal morphology (Fig. 4.1.1) act as soft spots for crack initiation and propagation leading to the observed stepped fracture

morphology (Fig. 4.1.10). In addition, with increasing the annealing temperature, the Si particles tend to agglomerate along the hatch overlaps and their amount is two times higher than the cores (Fig. 4.1.7 and Fig. 4.1.8). This result in crack initiation and propagation along the hatch overlaps leading to stepped fracture morphologies observed in (Fig. 4.1.10).
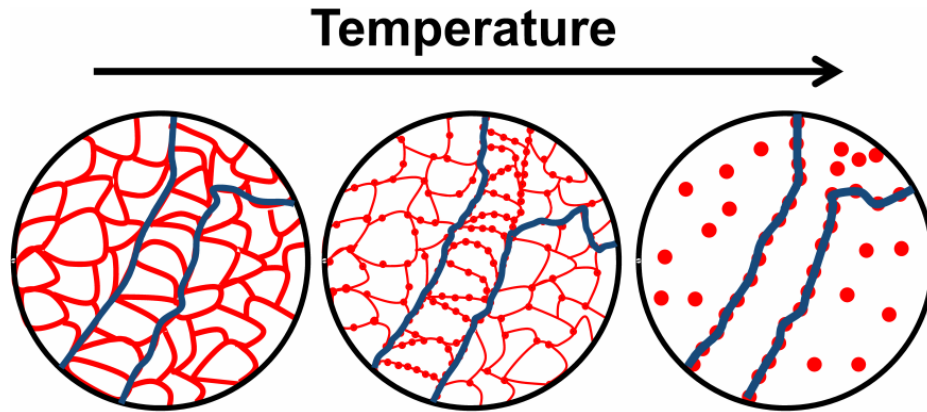
Fig. 4.1.11. Schematic illustration of the crack propagation path along the hatch overlaps of the SLM samples, where the density of the Si particles is higher in than the track cores.

4.1.4 Strength modeling

The prediction of the mechanical behavior of materials is an essential prerequisite in order to design and optimize their properties to meet specific requirements. For this, microstructural features, such as size, morphology and distribution of the different phases, are typically used to correlate the microstructure with the observed mechanical properties. Among these features, the crystallite size is one of the most important factors used to describe the strength of materials.

Strengthening induced by grain refinement is an effective approach for improving the mechanical performance of materials. The increase of strength σ resulting from grain refinement can be expressed by the semi-empirical Hall-Petch (HP) relationship ([Arm83a], [Muk06a]) as

$$\sigma = \sigma_0 + kd^{-\frac{1}{2}} \qquad , \qquad (4.1.2)$$

where σ_0 is the frictional stress resisting the motion of dislocations, k is the Hall-Petch slope associated to the resistance for the dislocation movement from one grain to another, and d is the average crystallite size [Son09a]. The size-induced strengthening results from the pile-up of dislocations at grain boundaries and from the resistance of the dislocations to slip transfer ([Arm83a], [Muk06a]).
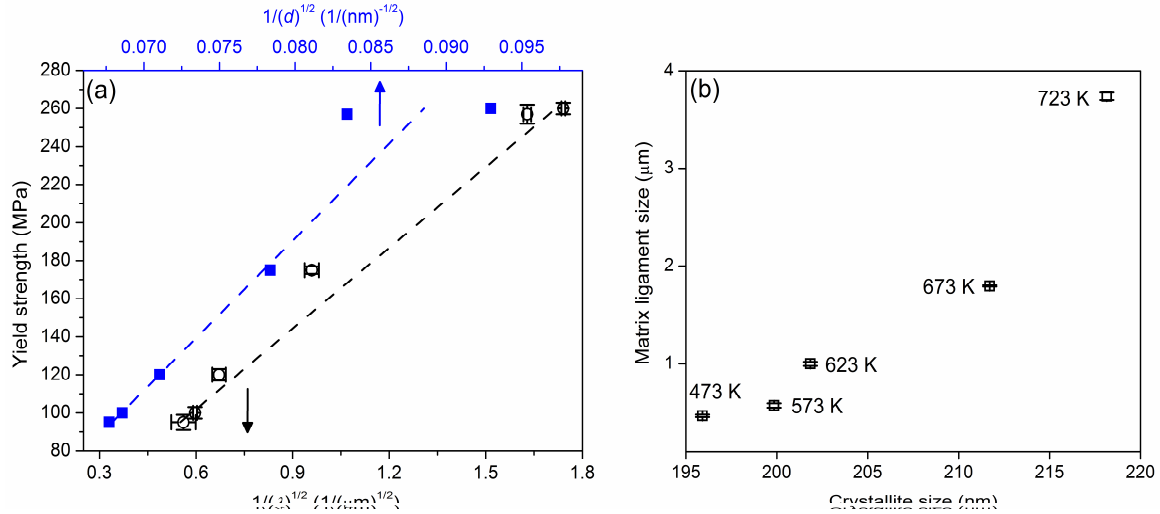
Fig. 4.1.12. (a) Yield strength as a function of the Al crystallite size (d) and matrix ligament size (λ) for SLM samples annealed at different temperatures and (b) correlation between crystallite size and matrix ligament size.

Fig. 4.1.12(a) shows the variation of the yield strength as a function of $1/(d)^{1/2}$ for the SLM samples annealed at different temperatures. The strength increases linearly with decreasing the crystallite size of Al (i.e. with decreasing the annealing temperature), in agreement with the expected Hall-Petch behavior. Interestingly, a similar behavior is also observed when the strength is plotted against the matrix ligament size λ, which, in the present case, represents the average matrix distance between the Si particles. However, while d varies in the nm range, λ is in the μm regime. Therefore, strengthening of the material apparently occurs at different length scales. Indeed, the obstacles to the dislocation movement represented by the large number of grain boundaries at small crystallite sizes (i.e. for low annealing temperatures) may combine with the large number of small Si particles at a larger length scale (Fig. 4.1.7). In addition, the growth of d and λ during the heat treatment is

most likely interdependent. This is corroborated by the results in Fig. 4.1.12(b), which shows a good correlation between the Al crystallite size *d* and the matrix ligament size *λ* for the different annealing temperatures. This offers the possibility to model the strength of the samples by using two easily accessible microstructural parameters describing different length scales of the material.

4.1.5 High temperature tensile tests

Al-Si alloys are generally used when the wear resistance is of utmost interest and the thermal expansion/contraction of the material has to be minimized at the service temperature ([Lee99a], [Lee00a]), such as in applications for engine components, where the service temperature ranges between 373 and 473 K ([Hir04a], [Alu11a]). Hence, it is necessary to know the behavior of these materials in such temperature conditions. Accordingly, the Al-12Si SLM samples were tested under uniaxial tensile conditions at 373, 423 and 473 K.
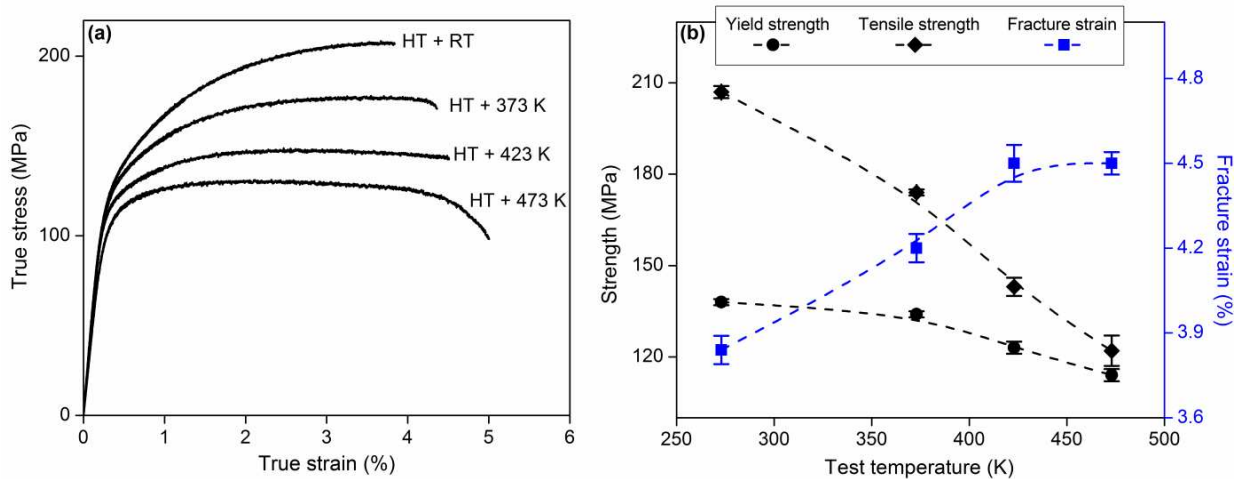
Fig. 4.1.13. (a) Tensile test curves of the SLM Al-12Si samples annealed at 573 K carried out at 273, 373, 423 and 473 K and (b) corresponding mechanical data.

The results shown in the previous sections indicate that microstructural changes take place in the Al-12Si SLM samples during annealing at high temperatures. Therefore, in order to achieve a stable microstructure and to avoid microstructural changes during the high-

temperatures tensile tests, the SLM samples were annealed at 573 K (i.e. above the testing temperatures 373 – 473 K) before the mechanical tests.

Fig. 4.1.13(a) shows the tensile curves for the Al-12Si SLM samples annealed at 573 K tested at 273, 373, 423 and 473 K, and the corresponding mechanical data are summarized in Fig. 4.1.13(b). The ultimate tensile strength of the samples drastically decreases from 207 to 122 MPa for the samples tested at temperatures 273 K and 473 K, respectively. In contrast, the yield strength of the same samples shows a marginal reduction from 138 to 114 MPa. The softening of matrix along with grain growth with increasing test temperature leads to a less pronounced strain hardening behavior [Cho11a]. However, the fracture strain shows only a limited increase from 3.8% to 4.5% for the samples tested between 273 and 473 K, suggesting that the SLM Al-12Si components at their service temperatures lose their strength without much change in their fracture strain.
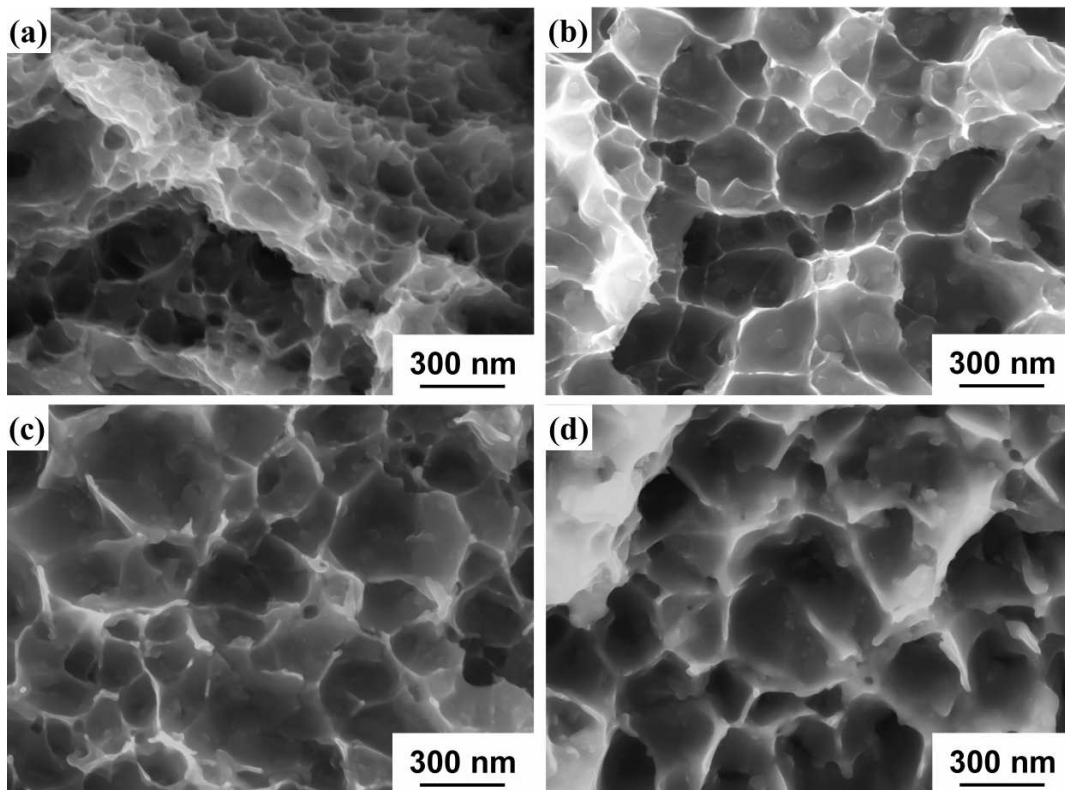
Fig. 4.1.14. Fracture morphology after tensile tests of the SLM Al-12Si samples annealed at 573 K tested at (a) 273, (b) 373, (c) 423 and (d) 473 K.
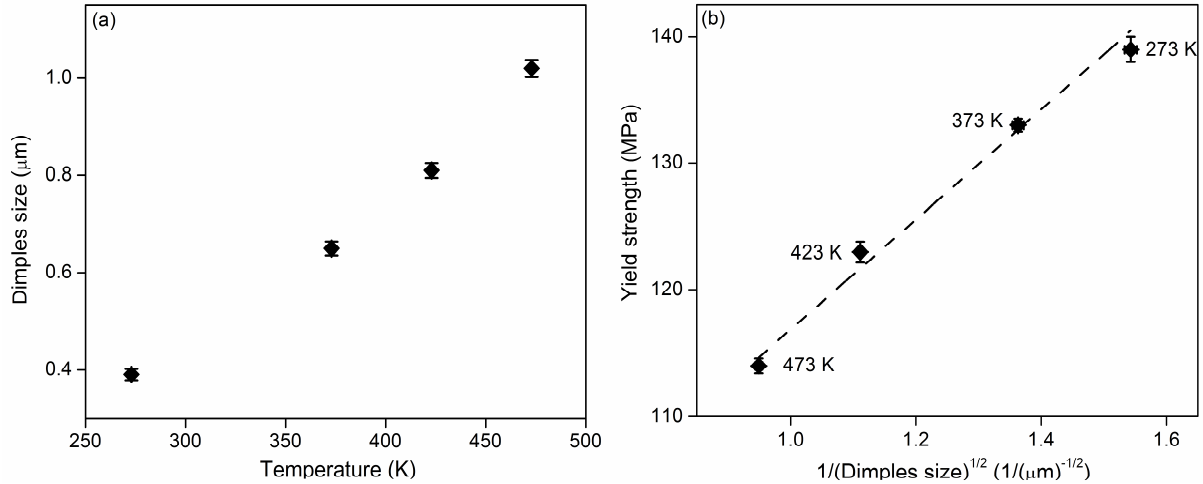
Fig. 4.1.15. (a) Variation of dimples size as a function of the tensile test temperature and (b) yield strength vs. dimples size for the Al-12Si SLM samples.

Fig. 4.1.14 shows the fracture morphology of the samples after the tensile tests carried out at various temperatures. The Al dimples already observed after the tests performed at room temperatures (Fig. 4.1.10) become larger for the tests carried out at high temperatures, in agreement with the high temperature mechanical tests of other Al-based alloys [Cho11a]. This can be ascribed to the softening of the Al matrix at high temperatures, as suggested by the tensile curves in Fig. 4.1.13. The size of the dimples increases linearly with increasing the test temperature (Fig. 4.1.15(a)). Interestingly, a linear correlation is also observed when the strength of the samples is plotted against the dimples size in the form of the Hall-Petch relationship (Fig. 4.1.15(b)). The variation of the dimples size observed here can be ascribed to the grain coarsening of the matrix resulting from the additional thermal energy supplied during testing.

4.2 Hatch style variation and its influence on mechanical properties

As discussed in Section 2.2.2, the hatch style is defined as the design or pattern in which the hatches are oriented within and between the layers. Thijs et al. [Thi13a] have used the hatch styles shown in Fig. 4.2.1 to vary the texture in their AlSi10Mg samples. In the case of the Al-12Si alloy, it has been observed in Fig. 4.1.1 (Section 4.1.1) that the hatch overlaps act as preferential sites for Si segregation and that the concentration of Si along the overlaps is two times higher than in the track cores (Fig. 4.1.8). In addition, the overlaps

show an elongated morphology, which is different from the core, where a cellular morphology is observed (Fig. 4.1.1). The results suggest that the hatch style may play a significant role for affecting the mechanical properties of the Al-12Si SLM samples.
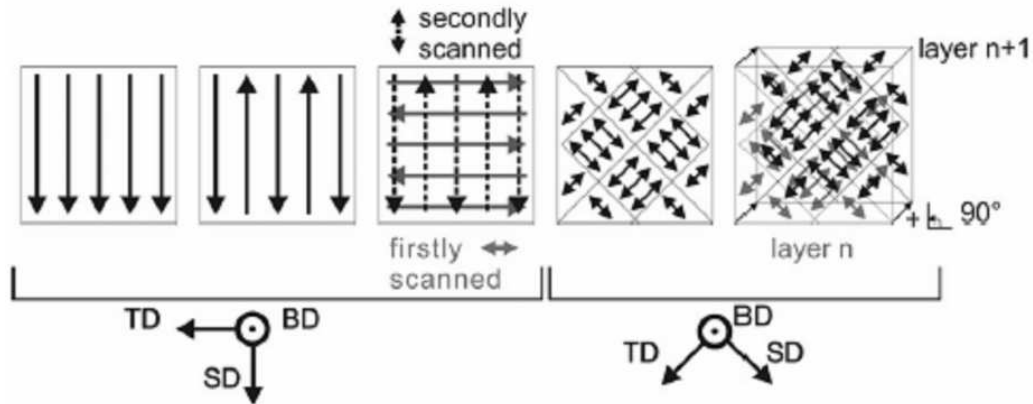
Fig. 4.2.1. Hatch styles adopted by Thijs et al. [Thi13a] to vary the texture of the AlSi10Mg samples processed by SLM.
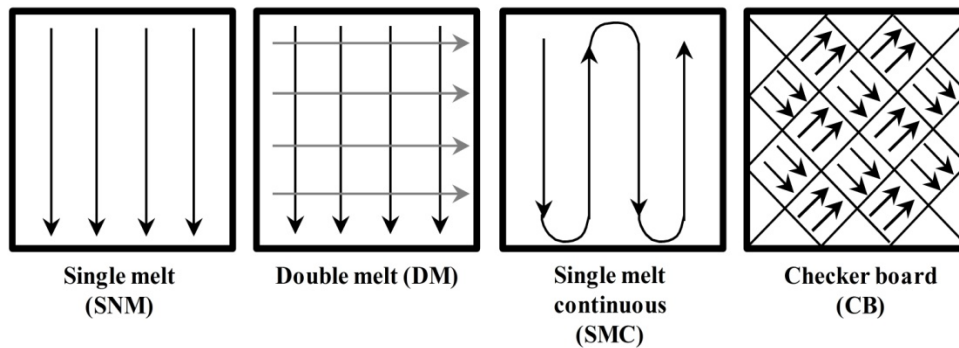
Fig. 4.2.2. The hatch styles used in the present study.

In this section, four different hatch styles are used (Fig. 4.2.2). The four hatch styles are termed: (1) single melt (SNM), which is the standard hatch style used for the production of the Al-12Si SLM samples investigated in the previous and following sections, where the powder particles are melted in a straight line fashion; (2) double melt (DM) style, which uses the single straight line melting style followed by another straight line melt perpendicular to the former; (3) single melt continuous (SMC), which melts the powder particles continuously

till the single layer is complete following a U-shaped pattern; (4) checker board (CB) hatch style refers to the melt sequence with a single layer divided into several small squares and between the squares single melt hatch style with different orientations used. The XRD patterns of the Al-12Si SLM samples produced with the different hatch styles are presented in Fig. 4.2.3(a), revealing that the various hatch styles lead to different levels of texture of Al.
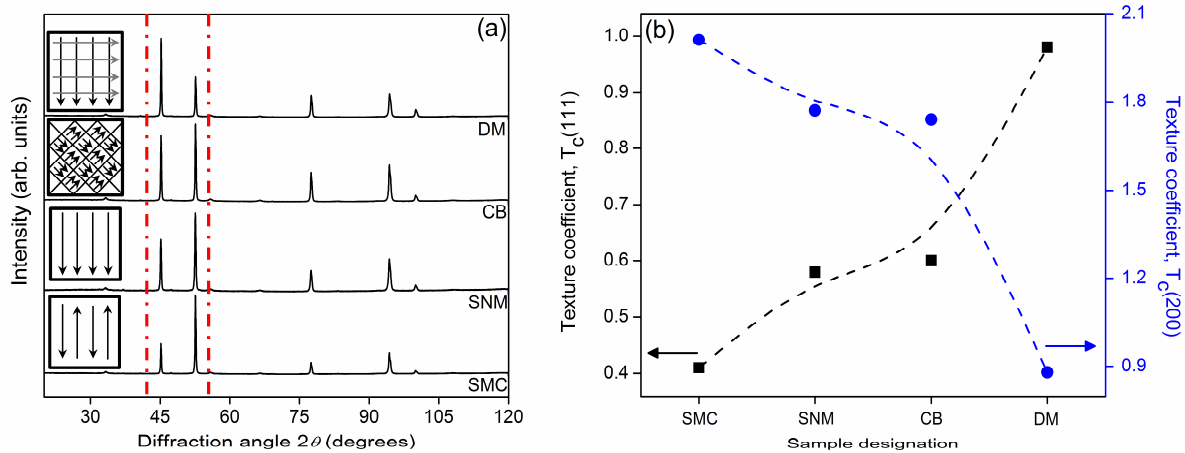
Fig. 4.2.3. (a) XRD patterns (λ = 0.17889 nm) of the Al-12Si SLM specimens produced using different hatch styles and (b) corresponding texture coefficient of the Al (111) and (200) planes quantified using Eq. (4.1.1).

The texture coefficients of the (111) and (200) Al planes evaluated using Eq. 4.1.1 are shown in Fig. 4.2.3 as a function of hatch styles. The texture coefficients show a significant variation with the change of hath style, in accordance to the report of Thijs et al. [Thi13a]. However, there are no reports about the influence of the hatch style on the mechanical properties of the SLM parts. Fig. 4.2.4 shows the variation of the room temperature tensile mechanical properties of the Al-12Si SLM samples as a function of the hatch style. No clear correlation is observed between the texture coefficient and tensile properties (compare Figs. 4.2.3(b) and 4.2.4(b)). The sample with CB hatch style displays the highest yield and ultimate strengths and the largest fracture strain among the tested materials. For example, the yield and ultimate strengths increase from 240 and 385 MPa for the specimens with the standard SNM hatch style to 290 and 460 MPa for the CB samples and the fracture strain increases from 2.8 to 4.5%. On the other hand, the samples with hatch styles SNM, SMC and

DM show similar strength levels, with a marginally increased fracture strain for the DM sample. In order to understand the reasons for the improved mechanical properties of the samples with CB hatch style, their microstructure before and after fracture is investigated.
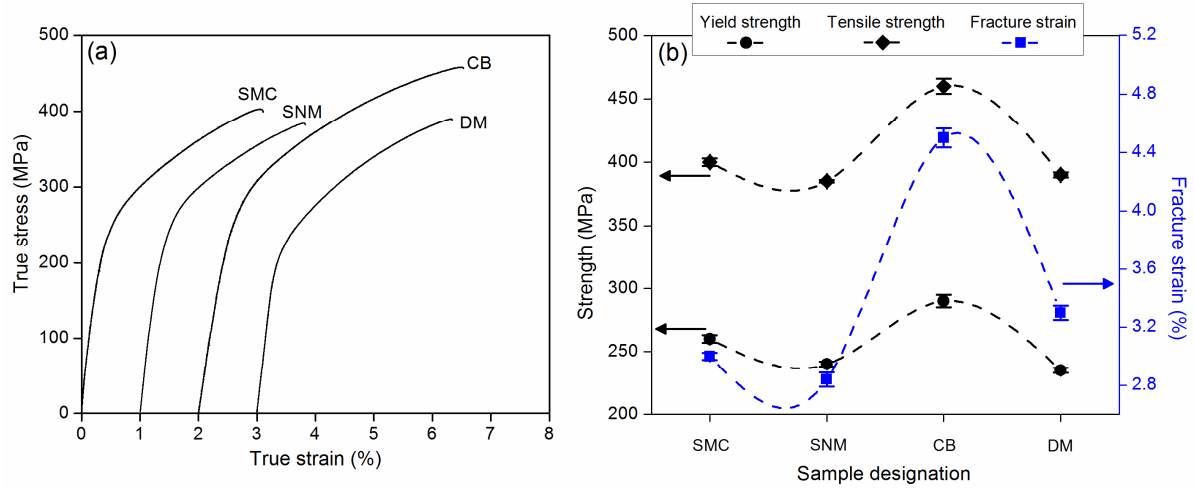
Fig. 4.2.4. (a) Room temperature tensile test curves for the Al-12Si SLM samples prepared using different hatch styles and (b) corresponding mechanical data.

Fig. 4.2.5 shows the OM and SEM images of the fracture surface after the tensile tests of the samples with hatch styles SNM and CB. The SNM sample shows the typical microstructure consisting of regular melt tracks (Fig. 4.2.5(a)). The fracture surface of this sample displays a step-like morphology (indicated by the red lines in Fig. 4.2.5(b)). On the contrary, the sample with CB hatch style shows a relatively complicated microstructure with the melt tracks running in a non-sequential way (Fig. 4.2.5(d)). This microstructure leads to a complex fracture surface (Fig. 4.2.5(e-f)), with no signs of the step-like features observed for the SNM sample.

The microstructure and the morphology of the fracture surface help to rationalize the crack propagation path in the SLM samples produced with different hatch styles. Fig. 4.2.6 shows the schematic illustration of the possible crack propagation paths in the SLM samples produced with single melt (SNM) and checker board (CB) hatch styles. The fracture propagates step-like (Fig. 4.2.5 (b-c)) in the SNM samples; on the other hand, the CB

samples show a more irregular fracture surface, resembling the morphology of the melt trucks (compare Figs. 4.2.5(d) and (f)).
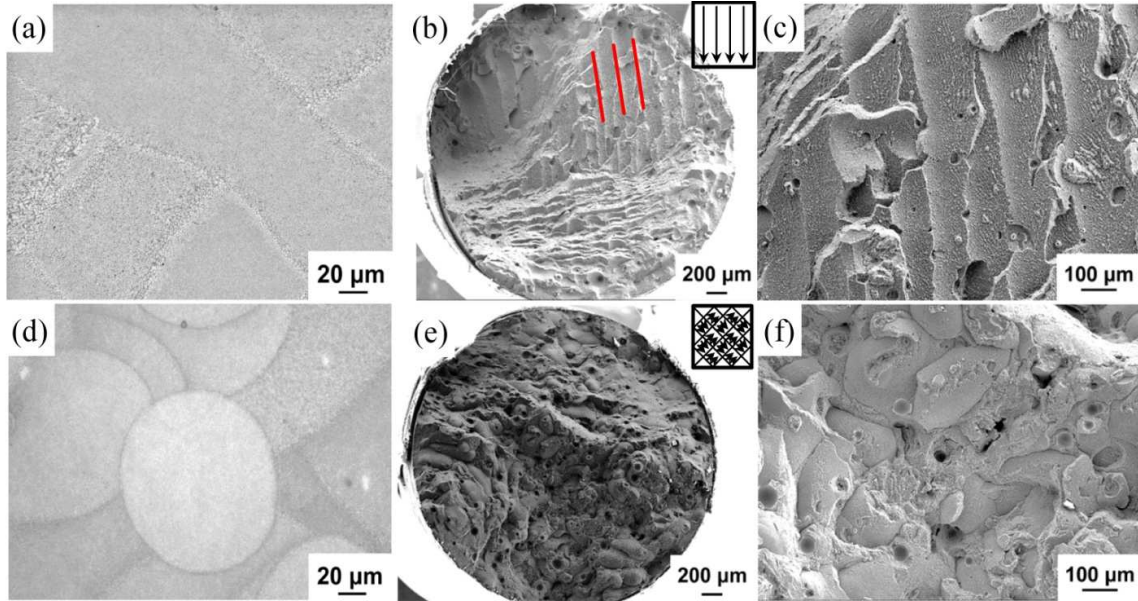
Fig. 4.2.5. (a) OM image of Al-12Si SLM sample produced using the single melt (SNM) hatch style, (b-c) SEM micrograph of the fracture surfaces (the red lines indicate the fracture propagation paths), (d) OM images of Al-12Si sample produced using the checker board (CB) hatch style and (e-f) SEM micrograph of the fracture surface.
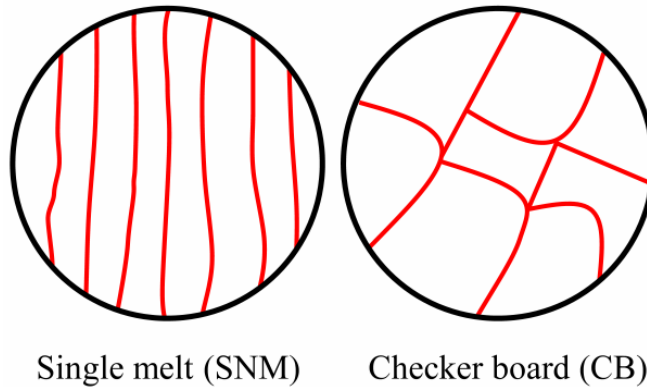
Fig. 4.2.6. Schematics illustrating the crack propagation paths in the Al-12Si SLM samples produced with single melt and checker board hatch styles.

Chapter 5: Tribological and corrosion properties of Al-12Si processed by SLM

5.1 Tribological properties of Al-12Si evaluated by sliding and fretting wear tests

The service life of an engineering component depends on several factors, such as environmental conditions, service temperature etc. ([Mid96a], [Kra12a]). Also, the tribological properties have an influential effect on the durability of the components, especially in automotive applications like pistons, cylinder heads etc. ([Eji07a], [Che08a]). It has been reported by several authors that the wear resistance of the components are directly related to the hardness of the material ([Khr74a], [Jeo03a], [Moo74a]) and that the wear resistance of materials, such as Al-Si alloys, can be enhanced by several methods, including grain refinement, surface coatings and alloying addition ([Jeo01a], [Mak12a]). The presence of hard Si particles in the Al-Si alloys leads to superior wear resistance and the amount, size, morphology and distribution have a remarkable impact on the tribological properties ([Cla79a], [Pra87a], [Pra98a], [Elm07a], [Las10a]).

The present section deals with the tribological properties of the Al-12Si produced by SLM. Sliding and fretting wear tests were carried out on as-prepared and annealed Al-12Si SLM samples and the results are compared with the same material produced by casting. The sliding wear rates are also compared with the data available in literature in order to fully evaluate the wear resistance of the SLM samples. The wear mechanisms are analyzed from the worn surface of both sliding and fretting wear tests and the factors affecting the tribological properties of the SLM samples are discussed.

5.1.1 Sliding wear

The sliding wear rate, Vickers hardness and size of the Si particles of the Al-12Si samples prepared by SLM are shown in Fig. 5.1.1 as a function of the annealing temperature along with the corresponding values of the as-cast Al-12Si material. The wear rate is at the minimum for the as-prepared SLM sample (300 K) and then it increases with increasing

annealing temperature, following an exponential form very similar to the behavior shown by the size of the Si particles in the same temperature range.
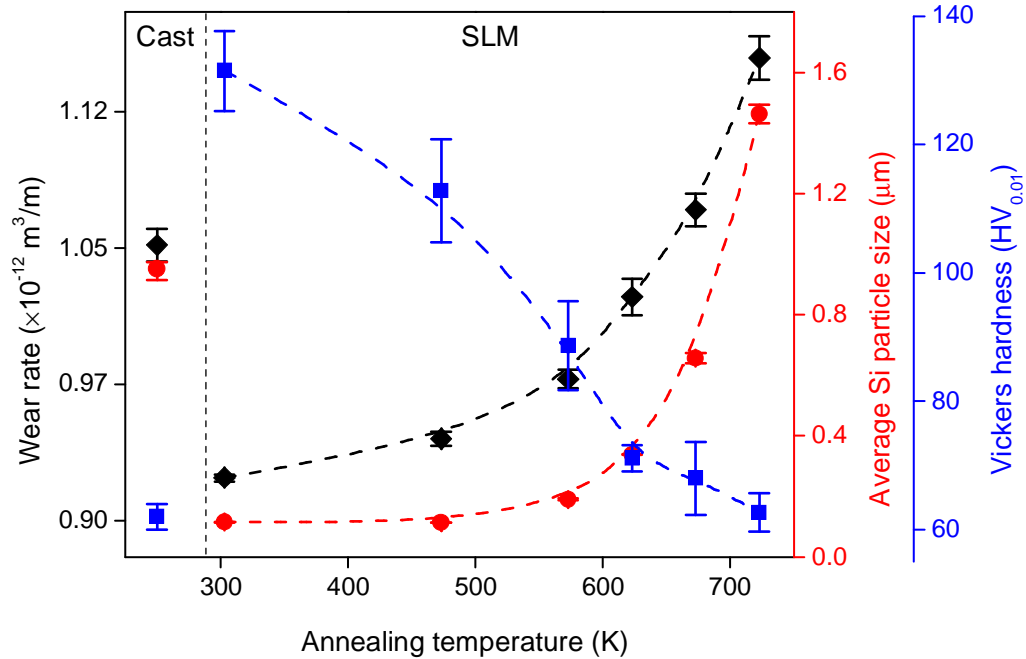
Fig. 5.1.1. Sliding wear rate (◆), average size of the Si particles (●) and the Vickers hardness (■) for the Al-12Si cast, as-prepared SLM (300 K) and SLM samples annealed at different temperatures.

Fig. 5.1.2 presents the wear tracks observed by SEM for the cast and as-prepared SLM materials and for the SLM samples annealed at 573 and 723 K after the sliding wear tests. The red arrows in the SEM images mark the sliding direction. The cast sample shows a very irregular surface morphology (Fig. 5.1.2(a)). During the sliding wear test, the pin induces a large strain level in the soft Al matrix at the contact surfaces. Due to such a strain, surface and sub-surface cracks are formed [Suh73a]. The cracks lead to the delamination of the surface, as observed in Fig. 5.1.2(a), and hence to significant material removal. In addition, oxidation of the surface was also observed by EDX composition analysis (not shown here) along with plastic deformation due to the traction of the pin surface on the hard steel counter disc [Suh73a]. The sliding of the pin against the disc promotes a strong temperature rise at the surface of the pin, leading to the preferential oxidation of the surface ([Suh73a], [Rag13a], [Dwi10a]). The abrasion of the pin surface is marked by the presence

of ploughing grooves, as observed in Fig. 5.1.2(a). These finding indicate that the wear of the Al-12Si cast sample is mainly due to the following mechanisms: abrasive component, delamination and oxidative wear ([Liu91a], [Sub92a]).
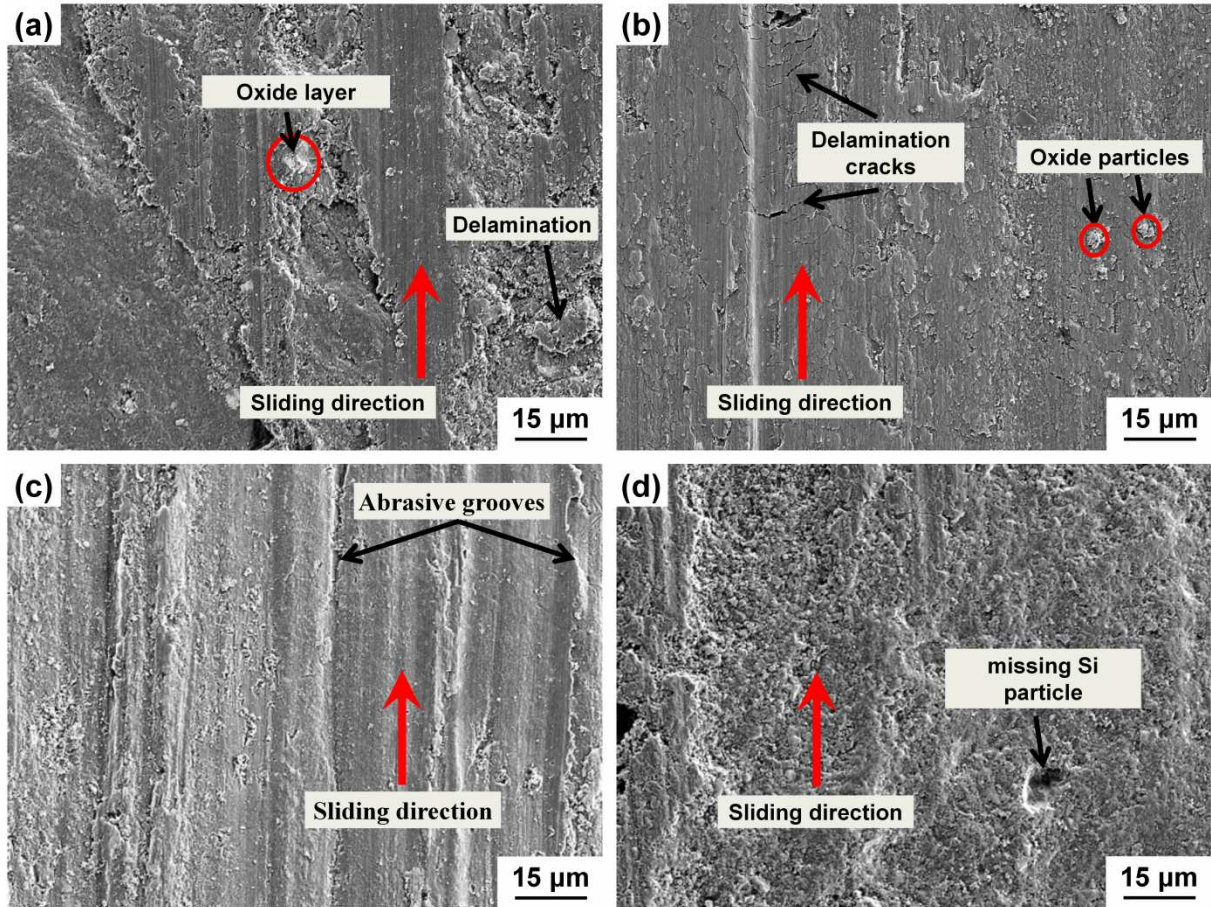
Fig. 5.1.2. SEM images of the wear tracks after the sliding wear tests for the Al-12Si samples: (a) cast, (b) as-prepared SLM and SLM annealed at (c) 573 and (d) 723 K.

The wear tracks of the as-prepared SLM sample are shown in Fig. 5.1.2(b). The wear tracks are shallow compared to the wear tracks of the cast sample (Fig. 5.1.2(a)), indicating that reduced wear occurs in this sample. The wear surface also shows the presence of oxide particles and delamination cracks but no significant delamination of the layers is observed. This is because the delamination cracks cannot transform to a delamination layer due to the higher hardness of the as-prepared SLM sample compared to the cast counterpart.

Selective oxidation is also observed along the worn surface of the as-prepared SLM sample (Fig. 5.1.2(b)). The presence of oxygen along the wear tracks suggests that the oxidative wear mechanism is prevailing in this sample. As the oxides are generally harder than the matrix, they may improve the wear resistance of the Al alloys [Dwi10a]. However, both the cast and as-prepared SLM samples show the presence of oxidation; therefore, the individual contribution of the oxides on the wear performance can be neglected in the present context. Consequently, the major wear mechanisms operating in the as-prepared SLM sample are abrasive component and oxidation wear ([Liu91a], [Sub92a], [Zha97a]).

The wear tracks of SLM sample annealed at 573 K (Fig. 5.1.2(c)) show deep abrasive grooves due to ploughing caused by the hard steel counter disc. Such wear morphology is very different compared to the as-prepared SLM material (compare Figs. 5.1.2(b) and 5.1.2(c)), suggesting different wear mechanisms operating in these two samples. Unlike the cast specimen, the SLM sample annealed at 573 K shows more pronounced abrasive grooves and plastic deformation. However, in contrast to the as-prepared SLM material, no distinct delamination cracks are observed, owing to the decreased hardness and increased ductility of the heat-treated sample. With further increase of the annealing temperature to 723 K, the specimens show more plastic deformation (Fig. 5.1.2(d)), corroborating the wear rate data in Fig. 5.1.1. In addition, removal of Si particles from the matrix has also been observed during sliding wear (Fig. 5.1.2(d)).

5.1.2 Fretting wear

The fretting wear results for the Al-12Si samples are shown in Fig. 5.1.3 as a function of the size of the Si particles. The amount of material removed (wear volume) is least for the as-prepared SLM sample. The fretting wear volume increases with increasing the Si size (and consequently with increasing the annealing temperature; compare Figs. 5.1.1 and 5.1.3). This behavior is remarkably similar to the trend observed for the corresponding sliding wear volume (also shown in Fig. 5.1.3). In contrast both the fretting and sliding wear volumes for the cast material do not follow the tendency shown by the SLM samples.

Fig. 5.1.4 shows the OM images of the Al-12Si samples after fretting tests along with the corresponding depth profiles. As a results of the rubbing of the steel ball, all samples display approximately circular wear scars with depth increasing from the edges to the center. This is due to the degree of volume loss being high at the center and gradually decreasing to zero towards the edges, which is characteristic for the fretting wear tests ([Zhu11a], [Ell02a], [Got04a]). The average diameter and the depth of the wear scar for the as-prepared SLM sample are 770 ± 50 µm and 25 ± 1 µm, respectively (Figs. 5.1.4(a) and 5.1.4(b)). Delamination of the surface along with abrasive wear acts as material removal mechanism for this material.
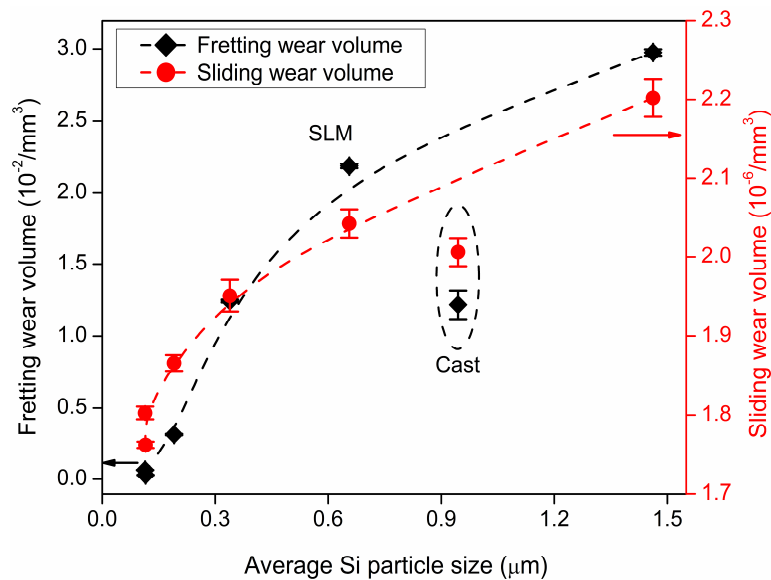
Fig. 5.1.3. Fretting (◆) and sliding (●) wear volumes for the cast and SLM Al-12Si specimens as a function of the average Si particle size.

The wear scar of the cast sample (Fig. 5.1.4(c)) shows traces of plastic deformation and delamination especially at the center of the damaged area. The diameter and the depth of the wear scar for the cast sample are 1220 ± 50 µm and 57 ± 2 µm (Figs. 5.1.4(c) and 5.1.4(d)); therefore, larger than the wear scar observed for the as-prepared SLM material. This indicates that more material is removed in the cast material, corroborating the results shown in Fig. 5.1.3.
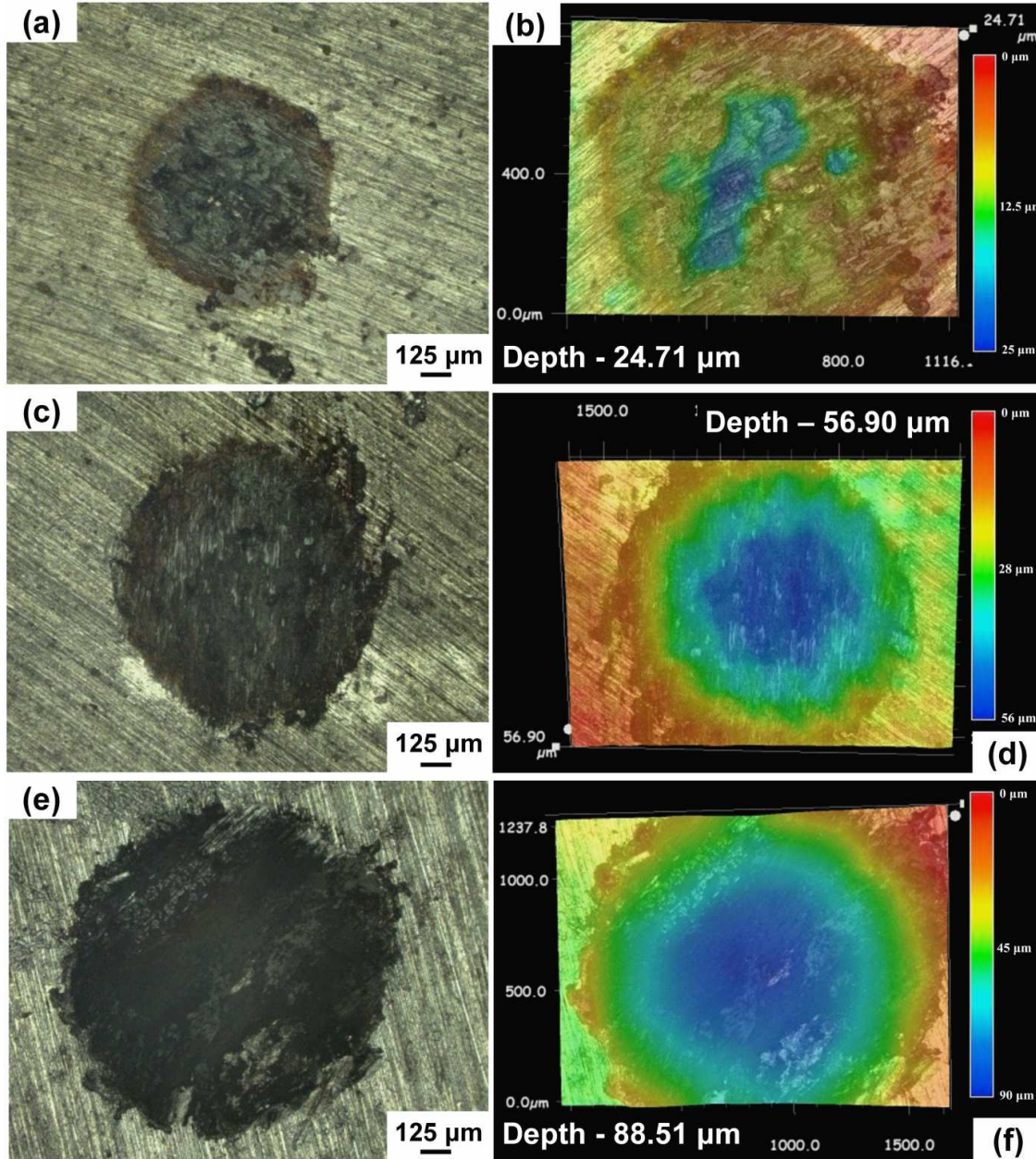
Fig. 5.1.4. OM images of the fretting wear scars and corresponding depth profiles for the Al-12Si samples: (a,b) as-prepared SLM, (c,d) cast and (e,f) SLM annealed at 723 K.

Different regions in the wear scar show different wear mechanisms: adhesive wear predominantly occurs at the center of the wear scar ([Zhu11a], [Ell02a]) along with traces of severe plastic deformation ([Tim99a], [Got04a], [Yoo11a]), whereas along the edges the main wear mechanism is found to be abrasive wear with some delamination cracks. This is in agreement with the mechanism proposed by Elleuch et al. [Ell02a], where material loss and

the elimination of the wear surface during the fretting wear process is aided by the increased adhesion between the plastically deformed material and the steel ball. The increased adhesive tendency leads to mass transfer from the wear surface due to both adhesive wear and delamination.

The wear scar of the SLM sample annealed at 723 K (Figs. 5.1.4(e) and 5.1.4(f)) shows deeper depth of penetration (89 ± 2 µm) as well as increased diameter of the wear scar (1550 ± 30 µm) compared to the cast and as-prepared SLM samples, indicating reduced wear resistance. The wear mechanism observed in the annealed sample is similar to the one operating in the cast material: plastic deformation and adhesive wear along the center and abrasive wear and delamination along the edges of the wear scar ([Tim99a], [Got04a], [Yoo11a]).

5.1.3 Wear rate evaluation and comparison

The volume loss during sliding wear (V_s) can be expressed by the Archard equation as [Arc53a]

$$V_s = \frac{kWL_s}{H} \quad , \quad (5.1.1)$$

where k is the wear coefficient, W the applied load, L_s the sliding distance and H the hardness of the material. The volume loss V_s, which is proportional to the wear rate Q_s (cf. Eq. (3.4.1)), is inversely proportional to the hardness of the material. The current system also obeys Eq. (5.1.1): the wear rate of the SLM samples increases with decreasing the hardness (Fig. 5.1.1). This is a direct consequence of the microstructure evolution during heating of the present SLM samples: the hardness decreases with increasing the size of the Si particles as a result of the annealing treatment (Fig. 5.1.5). In addition, the hardness decreases and, therefore, the wear rate of the SLM samples increases with decreasing the average density of the Si particles (Fig. 5.1.5), in agreement with previous works reporting that the good dispersion of the hard particles in the matrix leads to improved wear properties ([Kum08a], [Man07a], [Tha01a]). The same conclusions can be drawn for the fretting wear (Fig. 5.1.3).
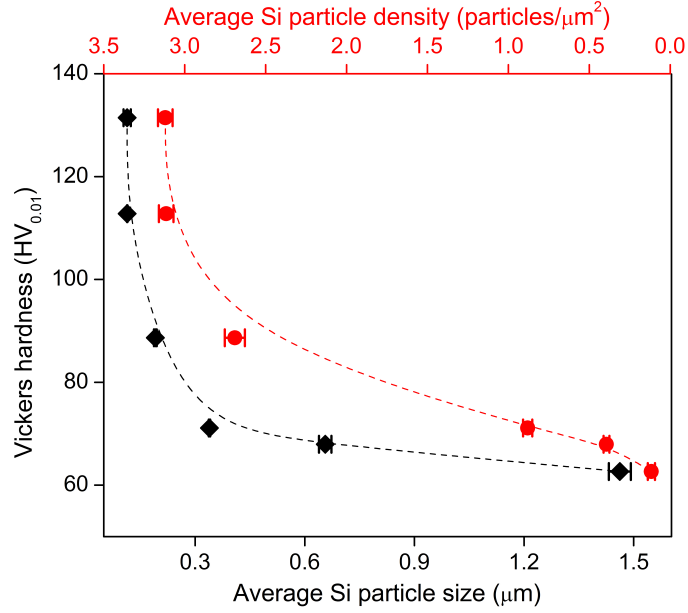
Fig. 5.1.5. Influence of the size (◆) and density (●) of the Si particles on the hardness of the Al-12Si SLM samples.
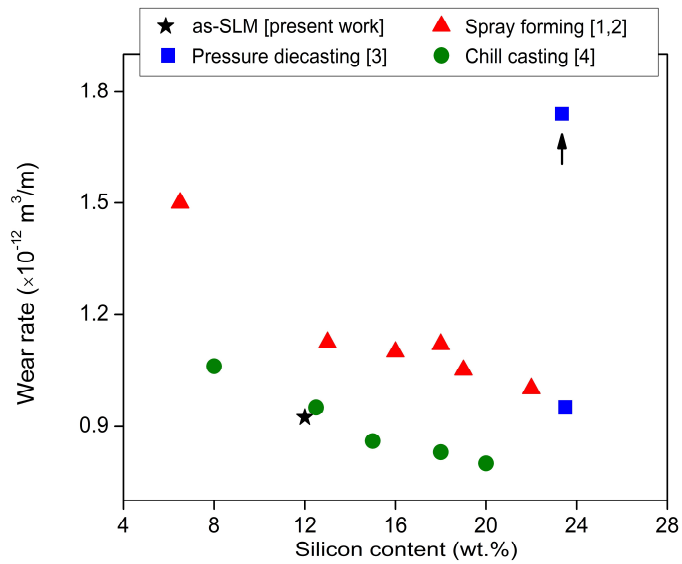
Fig. 5.1.6. Wear rates of Al-Si alloys produced by different techniques as a function of the Si content ([1] – [Rag13a], [2] – [Sri09a], 3 - [Pra98a], and [4] - [Tor94a]).

Fig. 5.1.6 compares the wear rates of the Al-Si alloys produced by different techniques, as a function of the Si content ([Rag13a], [Sri09a], [Pra98a], [Tor94a]). Similar

wear testing parameters are chosen, aiding for the direct comparison with the present materials, except for the spray-formed Al-Si samples with Si content between 13 and 22 wt.% [Rag13a], where the sliding speed is 0.3 m/s. Despite the slower sliding speed with respect to the present work (1 m/s) and the larger Si content, the wear rates of these samples are higher than the as-prepared SLM sample.

Prasad et al. [Pra98a] have estimated the wear rate of Al-23.5Si alloys produced by gravity and pressure die-casting. The wear rate of the Al-23.5Si sample produced by gravity casting (indicated by an arrow in Fig. 5.1.6) is ~ 50 % higher than the present as-prepared SLM sample, whereas the sample produced by pressure die-casting shows a similar wear rate even though the Si content is about 2 times larger.

Torabian et al. [Tor94a] have studied the sliding wear of binary Al-Si alloys with Si content ranging from 2 to 20 wt.% produced by chill casting. As expected, the wear rate of the chill-cast materials decreases with increasing the hard Si phase (Fig. 5.1.6). Like SLM, the chill casting technique can also achieve high cooling rates [Tor98a]. As a result, the wear rate of the chill-cast Al-12.5Si alloy is similar to that of the as-prepared Al-12Si SLM alloy. Except for the alloys produced by chill casting [Tor98a], all the other Al-Si alloys compared herewith ([Rag13a], [Sri09a], [Pra98a], [Tor94a]) have higher wear rates than the as-prepared SLM material. This indicates that the microstructural refinement achievable by SLM processing not only leads to a significant strengthening of the Al-12Si alloy, but induces remarkable tribological properties.

5.2 Corrosion behavior of Al-12Si SLM samples under acidic environment

The industrial applications of Al-based alloys are widespread, ranging from automobile, aerospace and marine to building and construction [Mar07a]. In some of these applications, Al-based alloys are exposed to acidic environments [Mus11a]. Hence, the knowledge on the corrosion resistance of Al-based alloys in acidic conditions becomes a prerequisite. Previous studies showed that Al-based alloys are passive in halide-free aqueous electrolytes with pH values between ~ 4.0 and 8.5 ([Son13a], [Hol14a]). In this pH range, the Al-based alloys generally form a stable passive Al_2O_3 layer. The oxide film is self-healing

and any mechanical abrasion or damage of the surface film does not lead to the corrosion of the underlying alloy [Ken01a]. However, aluminum suffers sever corrosion in mild nitric acid environments. The corrosion rate of Al in HNO_3 is of the order of 4.0 mm/y in the concentration range of 20-40 % HNO_3 at room temperature [Mus11a]. This section deals with the corrosion of as-prepared Al-12Si SLM, SLM heat-treated and cast samples in diluted HNO_3 solutions followed by a detailed investigation of the corroded surfaces.

5.2.1 Weight-loss tests

In order to determine the corrosion rate of the as-prepared Al-12Si SLM samples and the SLM materials annealed at 473, 573, 623, 673 and 723 K for 6 h, weight-loss tests in nitric acid solutions of three different concentrations (0.01, 0.1 and 1 M HNO_3) were carried out. Reference Al-12Si samples produced by conventional casting were also tested. The weight-loss curves for the as-prepared SLM specimens as a function of the HNO_3 concentration are shown in Fig. 5.2.1(a).
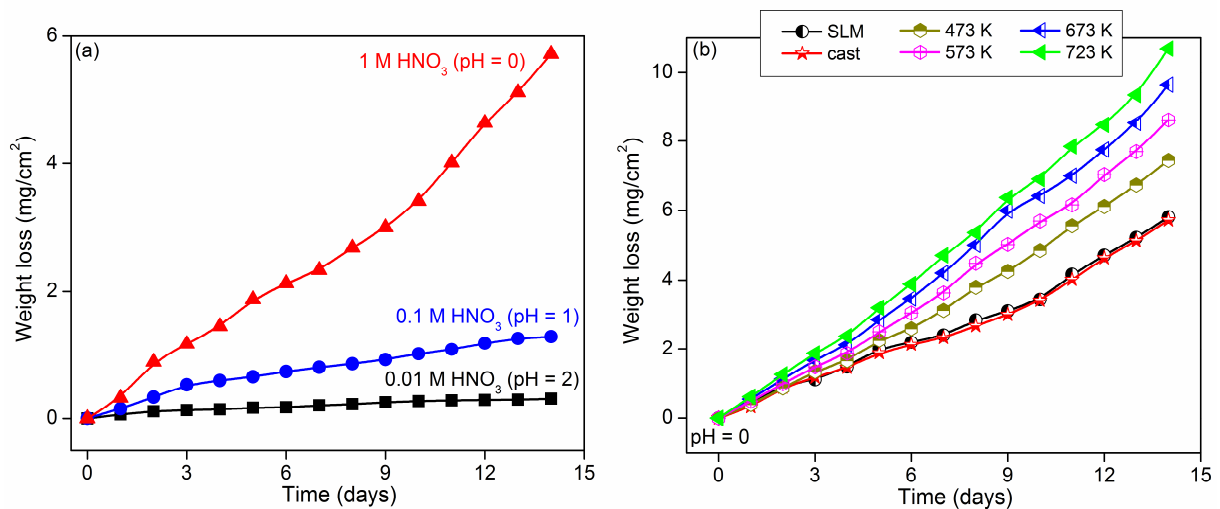
Fig. 5.2.1. (a) Weight-loss curves for the as-prepared SLM samples as a function of the immersion time for three different HNO_3 concentrations (0.01, 0.1 and 1 M). (b) Weight-loss plots for the as-prepared SLM, cast and SLM heat-treated samples as a function of time for the 1 M HNO_3 solution.

The samples show a weight-loss of 0.31 ± 0.04 mg/cm^2, 1.29 ± 0.11 mg/cm^2 and 5.72 ± 0.15 mg/cm^2 for 0.01, 0.1 and 1 M HNO_3, respectively, after 14 days of immersion (Fig.

5.2.1(a)), indicating that the weight-loss of the as-prepared SLM specimens increases by about four times for every one order of magnitude increase of the nitric acid concentration. The weight-loss curves of the as-prepared SLM samples are non-linear for all the tested concentrations: the corrosion rates are initially (within 3 days) high and then they decrease with increasing immersion time. While for the more dilute electrolytes, i.e. 0.01 and 0.1 M HNO_3, the corrosion rate remains more or less constant after 3 days, in the 1 M HNO_3 electrolyte the corrosion rate increases again after approximately 10 days.

In order to evaluate the weight-loss, the samples were periodically removed from the acidic solution. This might affect the corrosion process and, consequently, the corrosion rate. To clarify this aspect, three as-prepared SLM samples were kept continuously in a 1 M HNO_3 solution for 14 days. The weight-loss was found to be 5.49 ± 0.21 mg/cm^2, which is similar to the value observed when the same process is interrupted periodically (5.72 ± 0.15 mg/cm^2). This demonstrates that the periodic interruption of the corrosion tests has a minimal effect on the weight-loss.

Fig. 5.2.1(b) shows the weight-loss curves for the as-prepared SLM, cast and SLM heat-treated specimens in 1 M HNO_3 solution. The weight-loss curve for the as-prepared SLM and the cast specimens are very similar, suggesting that the corrosion behavior exhibited by these materials is comparable, even though the initial microstructures of these samples are different (cellular for the as-prepared SLM material and eutectic for the cast sample – see Section 4.1.1). The weight-loss gradually increases with increasing the annealing temperature for the SLM samples; a weight-loss of 10.68 ± 0.26 mg/cm^2 is observed for the material heat-treated at 723 K, which is two times the weight-loss observed for the SLM sample in the as-prepared condition.

Fig. 5.2.2 shows the cross-section of the as-prepared SLM samples exposed for 14 days to acidic solutions with three different HNO_3 concentrations. The corroded surfaces of the as-prepared SLM material display a porous-like cellular structure with pore size increasing with increasing HNO_3 concentration. This suggests that preferential corrosion of Al or Si occurs in these samples. Comparing the structure observed in Fig. 5.2.2 to the

cellular microstructure shown in Fig. 4.1.1, it can be ascertained that the remaining phase in the corroded materials is Si and that Al is corroded out under the acidic environment.
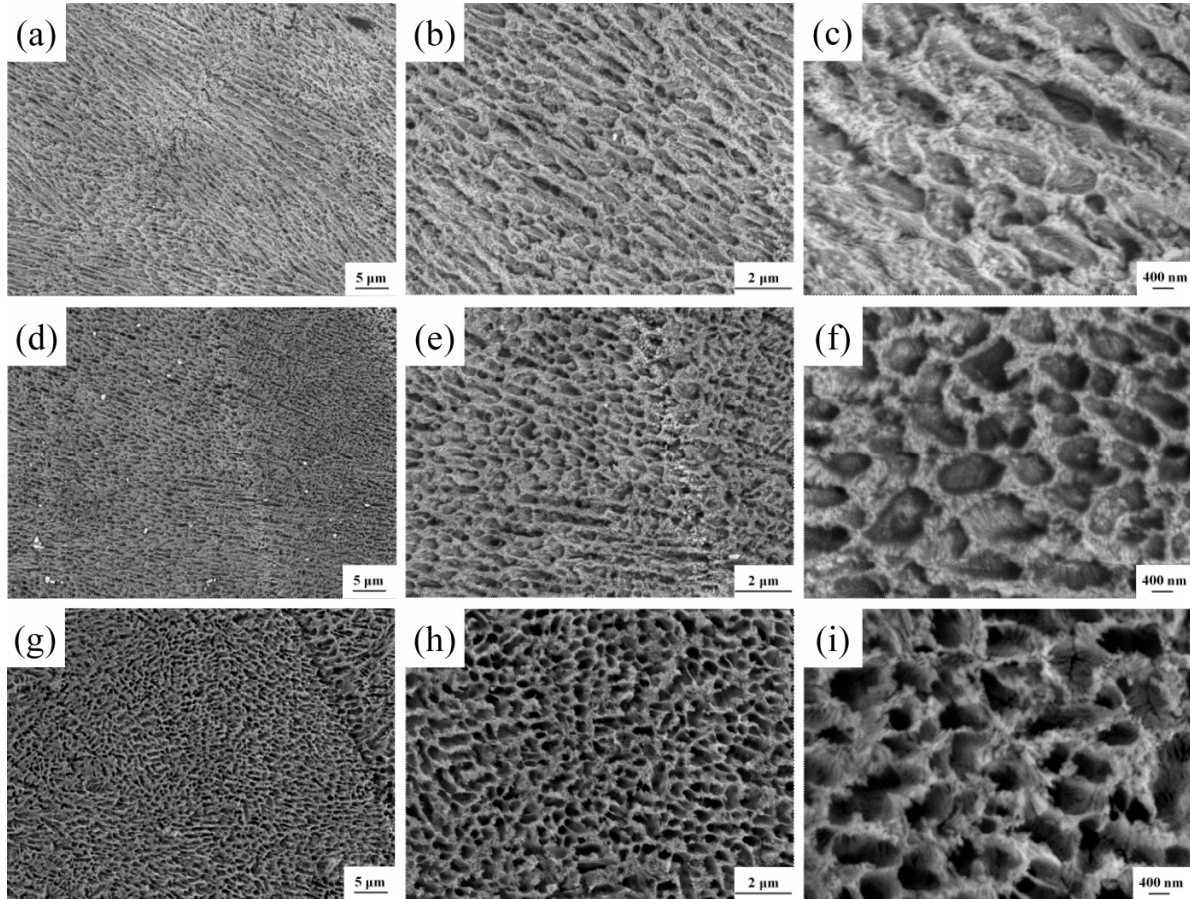
Fig. 5.2.2. Microstructure of the Al-12Si as-prepared SLM samples after 14 days of immersion in (a-c) 0.01 M HNO_3 (pH = 2), (d-f) 0.1 M HNO_3 (pH = 1) and (g-i) 1 M HNO_3 (pH = 0) solutions.

Fig. 5.2.3 shows the corroded surfaces of the Al-12Si SLM heat-treated at 673 K (Figs. 5.2.3(a-c)) and cast (Figs. 5.2.3(d-f)) samples after 14 days of immersion in 1 M HNO_3. As shown in Fig. 5.2.2, the as-prepared SLM sample shows a porous cellular structure after corrosion resulting from the selective corrosion of Al. However, the SLM heat-treated samples undergo a microstructural transformation (see Section 4.1.3) from cellular to composite-like microstructure, consisting of Si particles dispersed in the Al matrix. The SLM sample annealed at 673 K shows an average Si particle size of ~ 0.656 ± 0.17 μm (Section 4.1.3). Figs. 5.2.3(a-c) show Si particles in the same size range (~ 0.65

µm). The Si particles are isolated and are weakly attached to the surface of the samples as a result of the dissolution of the surrounding Al matrix. Corrosion of the Al matrix is not uniform and proceeds via a multitude of local dissolution events leading to the formation of pitting-like features. Those pits are clearly visible in the low magnification image shown in Fig. 5.2.4. It can be observed that the pits are formed throughout the surface of the sample. However, the size distribution of the pits is non-uniform, displaying diameters of the pits ranging from 5 to 50 µm.
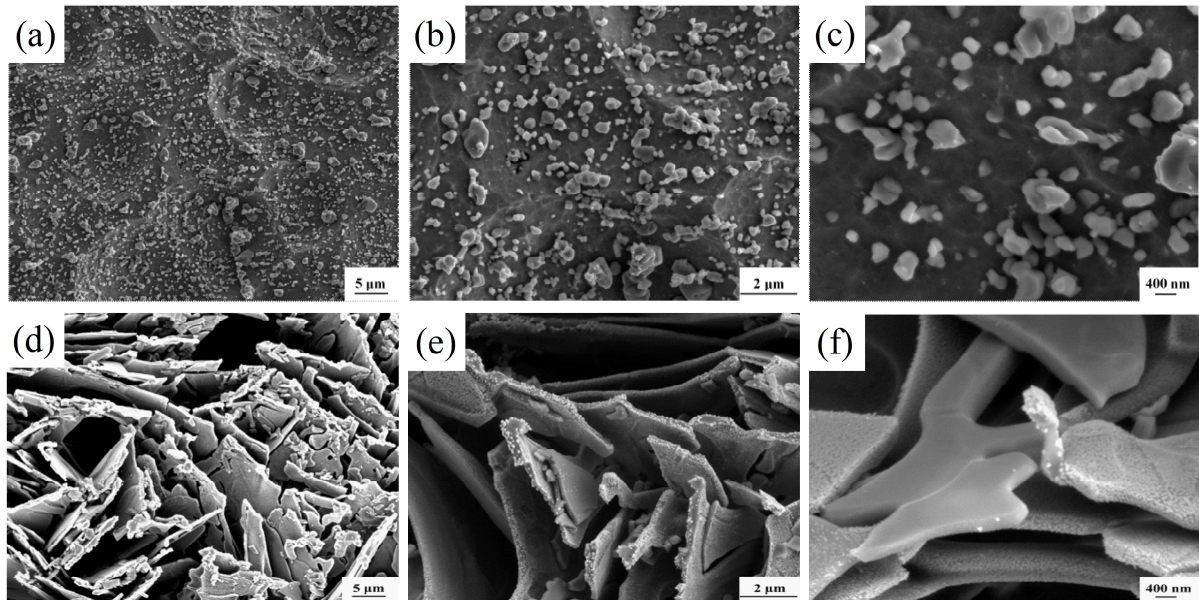
Fig. 5.2.3. Microstructure of the Al-12Si (a-c) SLM heat-treated at 673 K and (d-f) cast samples after 14 days of immersion in 1 M HNO$_3$ solution.
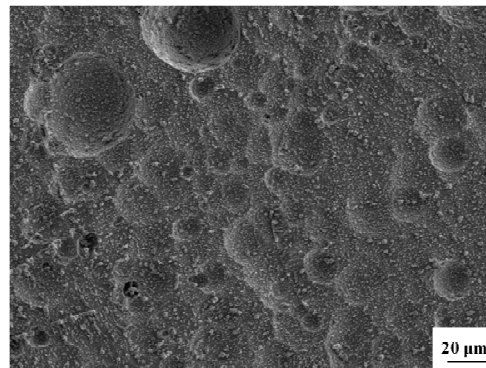
Fig. 5.2.4. Corroded surface of the Al-12Si SLM specimen annealed at 673 K after 14 days of immersion in 1 M HNO$_3$ solution.

The corroded surface of the cast sample (Fig. 5.2.3(d-f)) is in the form of an array of closely spaced Si platelets with length in the range 15 – 40 μm resulting from corrosion of Al from the eutectic microstructure. It is interesting to note that the corroded surface of the SLM, SLM heat-treated and cast samples are completely different. Therefore, in the following section the corrosion mechanism acting in these samples is analyzed.

5.2.2 Corrosion mechanism

In Al-based alloys, the corrosion is generally localized [JLi07b]. The dissolution mechanism of Al in HNO_3 is related to the following reactions [Far06a]:

$$Al + H_2O \quad \longleftrightarrow \quad AlOH_{aqs} + H^+ + e^- \qquad , \qquad (5.2.1)$$

$$AlOH_{aqs} + 5H_2O + H^+ \quad \longleftrightarrow \quad Al^{3+} \cdot 6H_2O + 2e^- \qquad , \qquad (5.2.2)$$

$$Al^{3+} + 6H_2O \quad \longleftrightarrow \quad [AlOH]^{2+} + H^+ \qquad , \qquad (5.2.3)$$

$$[AlOH]^{2+} + NO^{3-} \quad \longleftrightarrow \quad [AlOHNO3]^+ \qquad , \qquad (5.2.4)$$
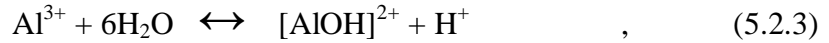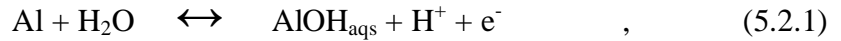
The rate-controlling step in the metal dissolution reaction is the reaction between the hydrate cation and the nitrate anion shown in Eq. 5.2.4 [Mus11a]. The soluble ions formed due to Eq. 5.2.4 increase the metal dissolution rate, which is a function of the HNO_3 concentration.

Fig. 5.2.5 shows the Pourbaix diagrams for Al and Si [Pou96a]. The concentrations of HNO_3 used in the present study (0.01, 0.1 and 1 M) correspond to pH values of 2, 1 and 0, respectively. At these pH levels, the Pourbaix diagrams suggest the dissolution of Al in the form of Al^{3+} ions (Fig. 5.2.5(a)). This dissolution reaction leads to the reaction shown in Eq. 5.2.3. On the contrary, the most favored state for Si is SiO_2, which may act as a passive film blocking further oxidation of the Si atoms (Fig. 5.2.5(b)). Hence, in the Al-Si system, the contact with HNO_3 leads to selective corrosion in the form of Al dissolution and to the formation of a passive SiO_2 layer. This explains why in in the present study the Al rich phase corrodes out, while the Si rich phase remains intact.
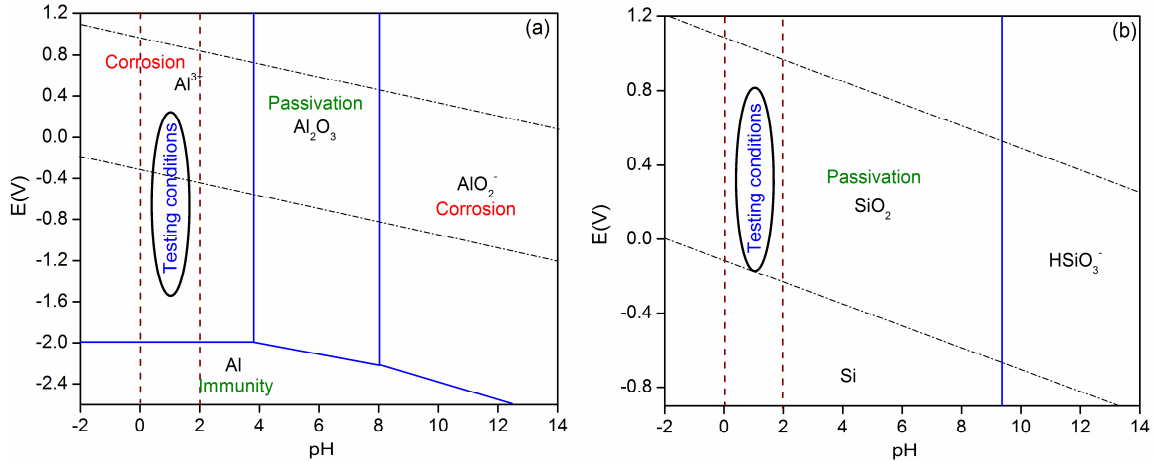
Fig. 5.2.5. Pourbaix diagrams for (a) Aluminum and (b) Silicon, showing the regions of corrosion, immunity and passivation (after [Pou96a]).

Fig. 5.2.6 shows again the weight-loss curve for the as-prepared SLM sample immersed in 0.1 M HNO$_3$ over the period of 14 days. As already observed in Fig. 5.2.1(a), the corrosion rate is not constant throughout the 14 days period. Instead, it shows a higher corrosion rate in the initial period of~ 3 days (corresponding to region – I in Fig. 5.2.6) and a reduced corrosion rate for the rest of the period (region – II). Similar behavior is observed for the cast samples and SLM specimens heat-treated at 473 and 573 K (Fig. 5.2.1(b)). In contrast, this behavior is not observed for the SLM samples heat-treated at 673 and 723 K.
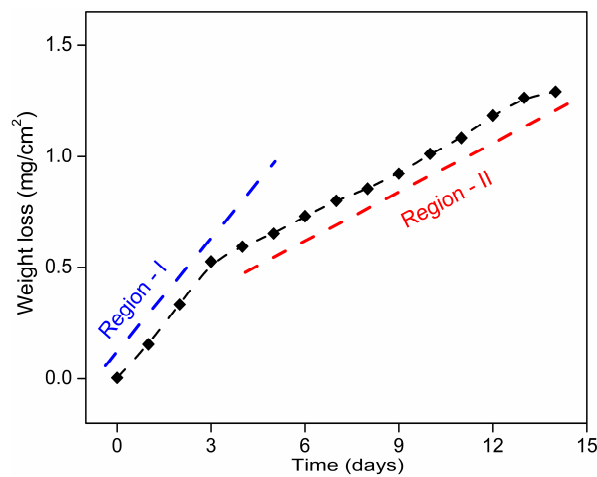
Fig. 5.2.6. Weight-loss curve for the as-prepared Al-12Si SLM samples for 0.1 M HNO$_3$, showing the different rates of corrosion as a function of the immersion time.

This behavior can be explained with the help of the schematic illustrations shown in Fig. 5.2.7. As a result of the rapid solidification during selective laser melting, the as-prepared SLM material has a cellular microstructure consisting of a supersaturated primary Al-rich phase with residual Si segregated at the cellular boundaries (see Section 4.1.1). In accordance with the Pourbaix diagrams presented above, the Al atoms from the Al-rich phase are expected to dissolve in the electrolyte as Al^{3+} ions, while the Si atoms are oxidized to SiO_2, which remains on the sample surface. As shown in Fig. 5.2.2, the cellular boundaries (now Si/SiO_2) are mechanically stable and remain attached to the sample surface. Hence, the continuous boundary network of Si prevails during the corrosion process (Fig. 5.2.7). This phenomenon is observed in the first 3 days of the corrosion process (region – I in Fig. 5.2.6).
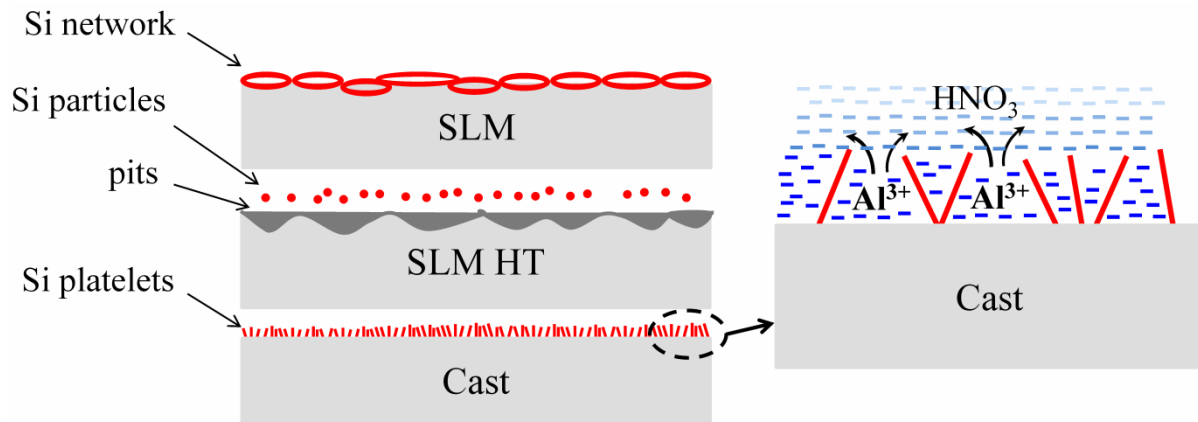
Fig. 5.2.7. Schematic illustrations showing the corrosion behavior in Al-12Si as-prepared SLM, heat-treated SLM and the cast samples under acidic environment.

Once that the first layer of the Al-rich phase is removed from the surface of the material, the presence of the continuous Si network hinders the access of the HNO_3 electrolyte to the subsequent layers. This restricted access may limit the transport rate of Al^{3+} away from the corroding interface and towards the bulk of the electrolyte, consequently decreasing the corrosion rate, as observed in region II. On the other hand, the heat-treated SLM samples, especially the materials annealed at 673 and 723 K, do not show a significant variation of the corrosion rate with the immersion time. In these samples, Si is present as isolated particles within the Al matrix (Section 4.1.3). Again, during corrosion in HNO_3, the

Al atoms are oxidized to Al^{3+} ions and are removed from the surface of the sample. Although the Si particles are not dissolved in the electrolyte due to passivation by SiO_2, they are no longer interconnected as in the as-prepared SLM material, and thus are easily detached from the surface once the surrounding Al matrix is corroded (Fig. 5.2.7). This process is continuous and, hence, corrosion takes place at a constant rate during the testing period, leading to pits throughout the samples surface. It is evident from Fig. 5.2.1(b) that the corrosion rate of the SLM samples increases with increasing the annealing temperature. According to Chapter 4, Si is gradually rejected from the supersaturated Al with increasing annealing temperature to form small Si particles and, at the same time, the Si cellular boundaries also transform into Si particles. The particulate morphology of free Si in the heat-treated samples explains well the increase of the corrosion rate with annealing temperature: as the annealing temperature increases, the amount of free Si in the form of isolated particles increases and their detachment due to the corrosion of the surrounding Al matrix contributes to the weight loss.

Contrary to the heat-treated SLM samples, the cast material shows a very similar weight-loss curve with respect to the as-prepared SLM samples. The cast samples display a eutectic microstructure (Fig. 4.1.2) with a larger amount of free Si and, consequently, with a smaller Si content in the Al-rich phase compared to the as-prepared SLM samples. This indicates that the connectivity of the free Si plays a more important role for affecting the corrosion rate than the solubility of Si in Al. Therefore, a similar two-stage mechanism as proposed for the as-prepared SLM material may be used to explain the corrosion features of the cast samples. In the region – I, the removal of Al takes place selectively from the surface of the sample. In the region – II, the access of HNO_3 to Al is restricted by the Si platelets (Fig. 5.2.7), leading to the observed decrease of corrosion rate.

Chapter 6: Friction welding of Al-12Si parts produced by SLM

SLM allows for the production of objects with intricate shapes and complex geometries that would be extremely difficult or impossible to fabricate through conventional subtractive manufacturing techniques [Wri06a]. However, the major drawback for the wide application of SLM as an industrial processing route is the limited size of the products. This is a direct consequence of the limited dimensions of the available building chambers, which allow for the production of samples with volumes of about 0.02 m^3 [Str13a]. A possible way to overcome this problem would be the use of the welding processes to join the small SLM objects to form parts with no dimensional limitations. The present chapter deals with the possibility of welding Al-12Si parts produced by SLM.

The yield strength of the Al-12Si alloy processed by SLM is four times higher than yield strength of a conventionally cast Al-12Si alloy. Such high-strength alloys cannot accommodate the stresses that arise during the fusion welding processes, which may lead to the formation of cracks [Kha10b]. To avoid such solidification related problems, solid-state welding can be utilized. This method does not present issues related to solidification cracking, liquation cracking, segregation and formation of brittle eutectics/intermetallics ([Kha10b], [Cro71a]). In addition, solid-state welding results in fine-grained microstructures with superior mechanical properties compared to the conventional fusion weld processes and in a narrow heat affected zone and low residual stresses in the weldment ([Kha10b], [Ven04a], [Kim05a]).

Among the solid-state joining processes, friction welding (FW) has drawn considerable attention due to economic considerations and high productivity [Kha10b]. In this process, heat is generated by the conversion of mechanical energy into thermal energy at the interfaces of the parts, rotated under pressure. Friction time and pressure, upset time and pressure, and rotation speed are the main parameters that govern the FW process. Compared with other welding techniques, friction welding displays advantages such as high materials saving, short joining time and possibility of making dissimilar joints ([Kat94a], [Maa07a], [Yil95a], [Shi10a], [Rot13a], [Ana09a]). Accordingly, this chapter focuses on the friction

welding of Al-12Si parts produced by SLM followed by the structural and microstructural characterizations. The mechanical properties of the welded samples are analyzed through hardness measurements and room temperature tensile tests followed by detailed fracture surface analysis. Factors leading to failure during the tensile tests are discussed and compared with the corresponding welded parts produced by casting.

6.1 Structural analysis

Fig. 6.1.1(a) shows a typical image of a friction welded Al–12Si joint with symmetrical and smooth flash at the joint, indicating adequate heat generation, plastic deformation and expulsion of oxide scales and other contaminants during the welding process ([SJi12a], [WLi08a]).
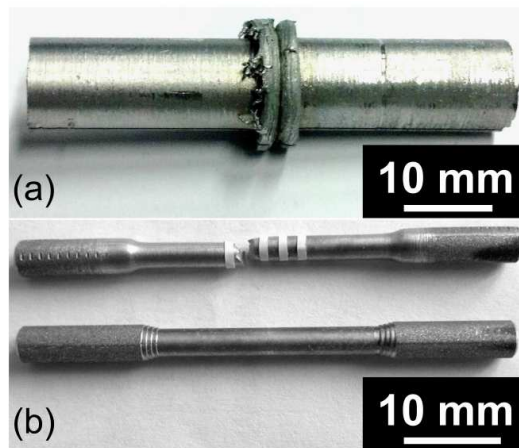
Fig. 6.1.1. (a) Typical image of a friction welded Al-12Si joint with symmetrical and smooth flash at the joint. (b) Examples of tensile specimens machined from the welded samples.

The XRD patterns of the base metal for the samples prepared by casting and SLM are shown in Fig. 6.1.2 along with the patterns of the weld zones. The diffraction peaks of Al and Si are observed in all cases with differences in their peak intensities and widths. The SLM–base metal shows a reversed intensity of the Al (111) and (200) peaks with respect to the same material produced by casting, indicating the presence of texture in the SLM sample (Section 4.1.1). The XRD pattern of the SLM–weld zone still shows texture of the Al (111)

and (200) peaks; however, this effect is much less pronounced than in the SLM–base metal. The intensity of the Si peaks increases and their width decreases in the SLM–weld zone compared to the SLM–base metal. This suggests that grain growth occurs in the weld zone. The XRD pattern of the cast–weld zone also shows similar texture of the Al (111) and (200) peaks as observed for the SLM–weld zone.
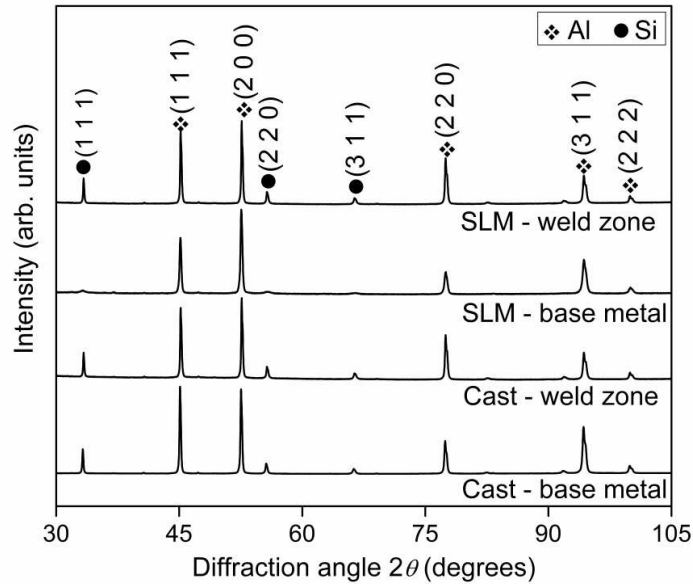
Fig. 6.1.2. XRD patterns ($\lambda = 0.17889$ nm) of the base metal and weld zone for the cast and SLM Al-12Si samples.

These observations are corroborated by Rietveld profile fitting analysis [Rie69a] carried out on the XRD patterns of the different samples. The lattice parameter of Al increases from 4.0508 nm for the SLM–base metal to 4.0522 nm for the SLM–weld zone. As a result, the amount of free residual Si increases from ~ 1 to ~ 10.5 wt.% after welding. The crystallite sizes of Al and Si are 118 and 8 nm for the SLM–base metal and 190 and 80 nm for the SLM–weld zone. On the contrary, the cast–base metal shows an Al lattice parameter of 4.0522 nm and an amount of free residual Si of ~ 10 wt.%,. The lattice parameter of Al and the amount of free Si do not significantly change in the cast–weld zone. The above results indicate that the weld zones of both SLM and cast samples show similar amount of free residual Si and texture.
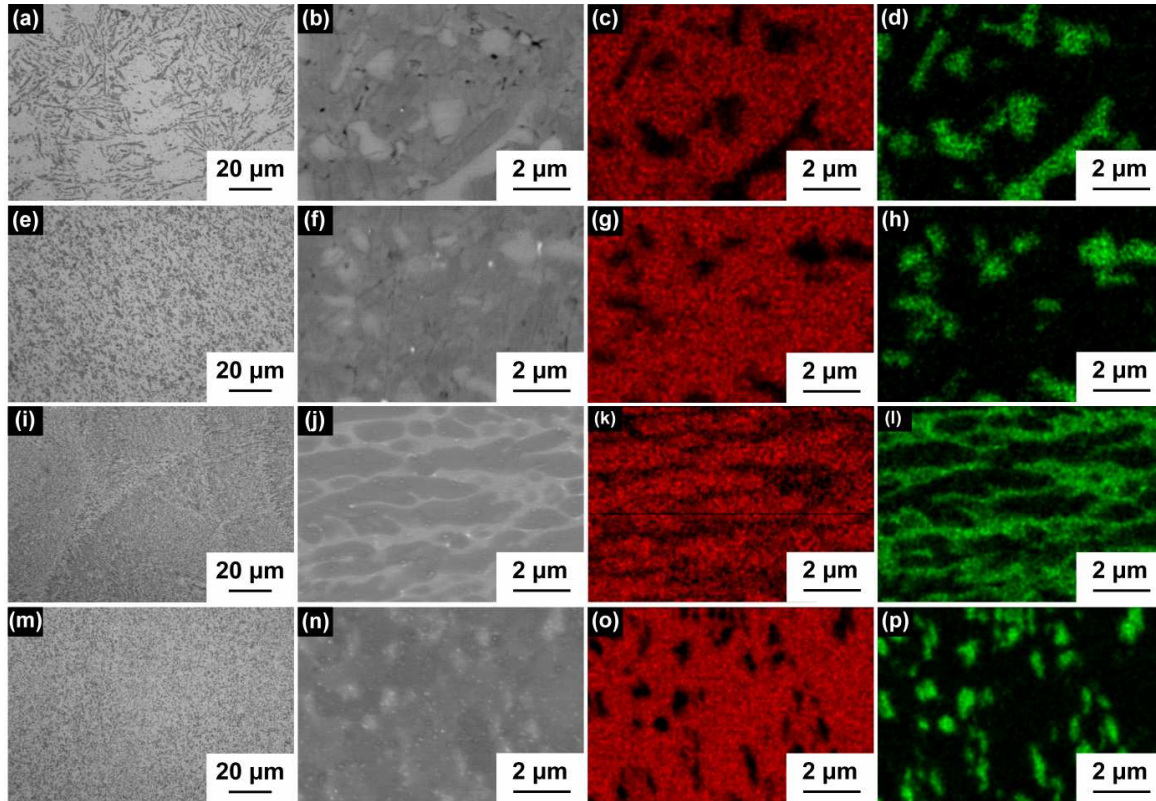
Fig. 6.1.3. OM and SEM micrographs, and EDX composition maps (red for Al and green for Si) for the Al-12Si samples: (a-d) cast–base metal, (e-h) cast–weld zone, (i-l) SLM–base metal and (m-p) SLM–weld zone.

The OM and SEM micrographs of the base metal and weld zone of the cast and SLM samples are presented in Fig. 6.1.3 along with the corresponding EDX composition maps (red for Al and green for Si). The cast–base metal displays a eutectic microstructure of Al and Si along with dispersed primary α-Al (Figs. 6.1.3(a) – 6.1.3(d)), characteristic of hypoeutectic compositions [Suá06a]. On the other hand, the weld zone shows a finely refined microstructure of Si particles uniformly dispersed in the Al matrix (Figs. 6.1.3(e) – 6.1.3(h)). Such a microstructure is characteristic for the weld zones processed by FW [Kha10a].

The SLM–base metal shows two types of morphologies (Figs. 6.1.3(i) – 6.1.3(l)): regions with circular cellular morphology which are separated by thin boundaries with elongated columnar morphology (Section 4.1.1). The weld zone of the SLM sample shows a noticeable change in the size and shape of the cells when compared with the base metal. The

elongated columnar morphology is absent and the microstructure consists of small Si particles uniformly distributed in the Al matrix (Figs. 6.1.3(m) – 6.1.3(p)).
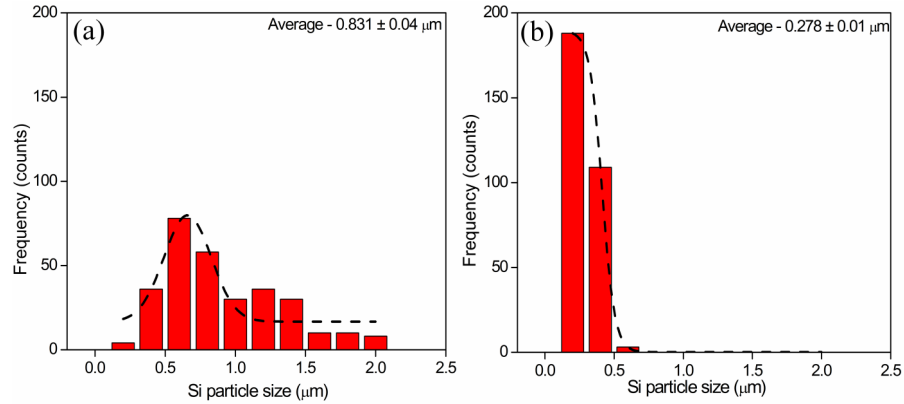
Fig. 6.1.4. Si particle size distribution in the weld zone of (a) cast and (b) SLM samples.

Both the weld zones of the cast and SLM samples show strong similarities in their morphology but they display different sizes of the Si particles. This is evident by analyzing the size distribution of the Si particles in the weld zones of the cast and SLM samples (Fig. 6.1.4). The cast–weld zone shows Si particles with size ranging between 0.1 and 2 µm and average size 0.831 ± 0.04 µm. On the other hand, the SLM–weld zone exhibits a narrower distribution of Si particles with size ranging between 0.1 µm and 0.6 µm. The average size of the Si particles is 0.278 ± 0.01 µm, therefore smaller than the size observed in the weld zone of the cast sample. The observation of such fine Si particles in the FW SLM sample may be attributed to the refined microstructure of the parent base metal.

6.2 Microhardness measurement

The Vickers microhardness profile along the weld interface for the FW cast and SLM samples is shown in Fig. 6.2.1. The difference in hardness along the weld interface (marked by a red dashed line in Fig. 6.2.1) can be clearly observed. The microhardness profiles are nearly symmetrical with respect to the weld interface for both FW cast and SLM samples. However, the mechanisms operating in the samples are different. In the case of the FW cast sample, the hardness at the weld interface is ~ 72 $HV_{0.01}$, which is significantly higher than

that characterizing the base metal ~ 58 $HV_{0.01}$). The hardness remains rather constant for approximately 0.5 – 0.75 mm on both sides of the weld interface. The hardness then drastically decreases at about 1 mm from the interface, reaching a steady state of ~ 58 $HV_{0.01}$. This is in accordance with what was observed for other FW Al-based alloys ([Kat94a], [Yil95b], [Shi00a]). On the contrary, the FW SLM samples show hardness of ~ 81 $HV_{0.01}$ at the weld interface, which is lower than the base metal (~ 95 $HV_{0.01}$). The hardness remains steady for almost 0.4 mm on both sides of the interface. Moving further away from the weld interface, the hardness increases gradually to reach ~ 95 $HV_{0.01}$.
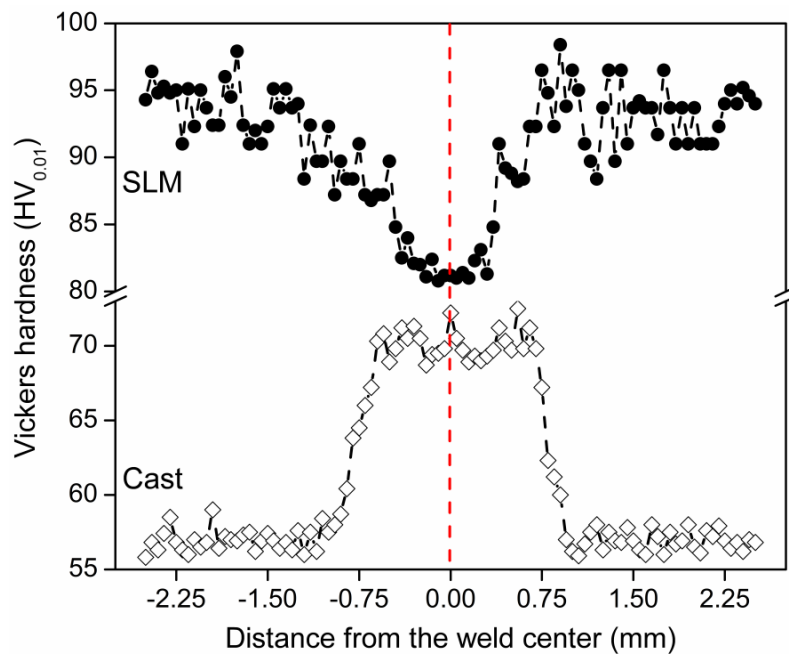
Fig. 6.2.1. Vickers microhardness profile measured across the weld interface of the Al-12Si cast and SLM samples.

The hardness of the SLM–weld zone is ~ 9 $HV_{0.01}$ higher than the hardness observed at the weld interface of the FW cast sample. This can be attributed to the dimensions of the Si particles in the weld zones, which are ~0.28 μm for the FW SLM sample and ~ 0.84 μm for the FW cast material. The hardness at the weld interface is normally higher than the base metal [Yil95a], as observed in the FW cast sample, due to the refinement of the microstructure in the weldment (Fig. 6.2.1). In contrast, the hardness of the FW SLM sample at the weld interface is lower than the base metal. A similar behavior has been reported by

Khalid Rafi et al. [Kha10b] for FW of AA7075-T6 alloy, where the hardness of the weld zone decreases due to dissolution or coarsening of the strengthening precipitates. In the present case, the high hardness of the SLM–base metal is due to the supersaturated Al matrix with a large content of Si (~ 11 wt.%). In addition, the Al and Si phases have a very fine crystallite size of 118 and 8 nm, respectively. In the weld zone, the amount of Si in Al decreases to ~ 1.5 wt.% with a relatively coarse crystallite size of Al and Si (190 and 90 nm). Moreover, the morphology of Si changes from a continuous Si network for the SLM–base metal to homogeneously distributed Si particles in the weldment. Such distinct changes in the microstructure result in the contrasting hardness profile with respect to the FW cast material.

6.3 Tensile properties

The mechanical properties of the FW materials have been investigated by room temperature tensile tests (Fig. 6.3.1). The tensile specimens were prepared form the welded samples ensuring that the center of the weldments corresponds to the center of the tensile bars (compare Figs. 6.1.1(a) and 6.1.1(b)). The FW cast sample shows higher yield strength than in the as-cast condition but reduced fracture strain (~ 2%). Moreover, the cast FW sample fails in the weld zone (not shown here), suggesting that the weld zone is harder and more brittle than the base metal, in agreement with the hardness data in Fig. 6.2.1. The yield strength of the FW SLM sample is ~ 215 MPa, which is ~ 45 MPa lower than in the as-SLM condition. However, the welded sample shows extended ductility with a fracture strain of about ~ 10% compared with the as-SLM material (~ 3%). The fracture of the FW SLM specimen occurs in the base metal and not in the weld zone, corroborating again the hardness results in Fig. 6.2.1.

Fig. 6.3.2 shows the fracture morphology of the FW cast and SLM samples after room temperature tensile tests. The fracture surface of the FW cast specimen (Figs. 6.3.2(a,b)) shows dimples in the Al phase and cleavage along the brittle Si particles (indicated by arrows in Figs. 6.3.2(a,b)). This is similar to the fracture surface of the as-cast material (Section 4.1.4). On the other hand, the fracture surface of the FW SLM sample (Figs. 6.3.2(c,d)) shows the presence of dimples with average size of ~ 0.46 ± 0.09 µm,

which is very similar to that observed for as-prepared SLM samples under similar testing conditions (Section 4.1.4).
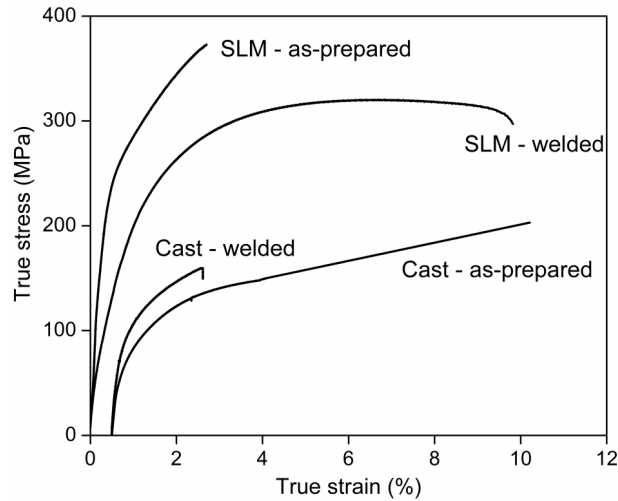
Fig. 6.3.1. Room temperature tensile curves of the cast and SLM specimens tested in the as-prepared and welded conditions.
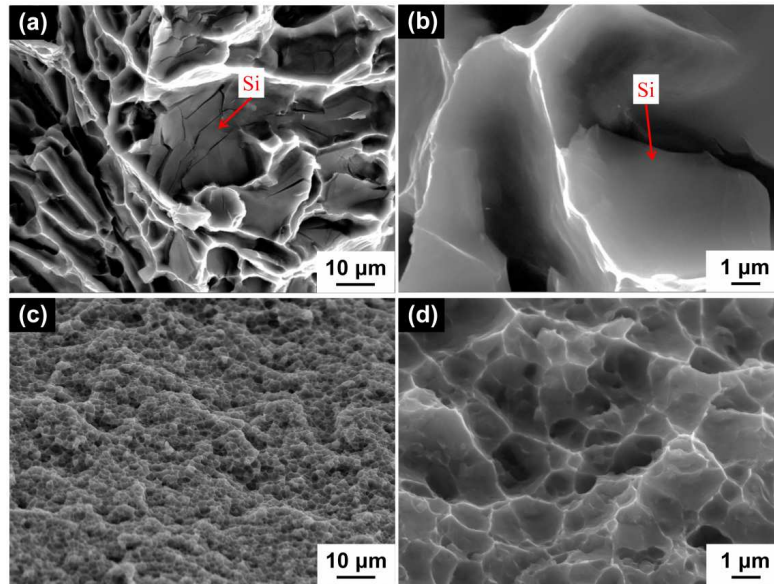
Fig. 6.3.2. Fracture morphology of the FW cast (a – b) and FW SLM (c – d) samples after room temperature tensile tests.

These findings demonstrate that solid-state friction welding can be successfully used to join materials produced by SLM and helps to significantly improve their ductility. This offers the possibility to overcome the problem of the limited dimensions of the SLM parts in order to produce objects with no dimensional limitations.

Chapter 7: Conclusions and outlook

In this work, Al-12Si samples with an extremely fine supersaturated Al-rich cellular structure along with residual Si at the cellular boundaries have been produced by SLM. The Al and Si phases show remarkably small crystallite sizes of about 118 and 8 nm. The as-prepared SLM samples display yield and tensile strengths of about 260 and 380 MPa, which are respectively four and two times higher than the corresponding values of the cast material. However, the fracture strain is only ~ 3 %; therefore, significantly reduced compared to the cast sample (~ 9.5 %). In order to clarify the mechanical behavior of the SLM parts, the effect of texture and microstructural features (morphology, size and distribution of the Al and Si phases) have been analyzed in detail.

The texture was varied by producing SLM samples with an inclination angle between specimens and substrate plate varying between 90 and 30°. Tensile tests reveal a yield strength ranging between 255 and 260 MPa, which indicates that the effect of texture on the strength of the samples is negligible. In order to evaluate the effect of the microstructure on the mechanical behavior of the samples, the SLM specimens were isothermally annealed at temperatures between 473 and 723 K. The microstructure becomes coarser with increasing the annealing temperature. Si is rejected from the supersaturated Al to form small Si particles. The size of the particles increases exponentially, whereas their number decreases. The evolution of the microstructure is not homogeneous throughout the samples: number and size of the Si particles in the hatch overlaps are constantly larger than in the track cores. This finally leads to a composite-type microstructure consisting of soft α-Al regions surrounded by areas with a higher density of larger Si particles.

The variation of the microstructure has a significant influence on the mechanical properties of the SLM parts. The yield strength decreases from 260 MPa for the as-prepared SLM samples to 95 MPa for the samples with the coarsest microstructure. In contrast, the fracture strain remarkably increases from ~ 3 to 15 %. This demonstrate that the mechanical behavior of the Al-12Si SLM samples can be tuned within a wide range of strength and ductility by properly varying their microstructure. In addition, the strength of the samples

was successfully described using the crystallite and the matrix ligament sizes, which are microstructural parameters describing different length scales of the material.

The high temperature tensile tests reveal that both the yield and ultimate strength of the samples annealed at SLM 573 K decrease with increasing the test temperature due to the softening of the Al matrix. However, no significant changes are observed for the ductility of the sample with increasing the test temperature.

The Al-12Si SLM specimens were produced with different hatch styles. This leads to different texture levels in these samples. In addition, the change in hatch style alters the microstructure due to the variation in the Si distribution and morphology, resulting in the variation of the tensile properties. The fracture surface shows different crack propagation paths for the single melt and checked board samples, suggesting that the hatch style is another variable that can be effectively utilized to tune the tensile properties of the Al-12Si samples.

The tribological properties of the SLM specimens were tested using sliding and fretting wear tests. In both the tests, the as-prepared SLM sample shows better wear resistance than the cast and SLM heat-treated samples. The sliding wear in the as-prepared SLM samples is due to the abrasive component and oxidation wear. In contrast, the SLM heat-treated samples show deep abrasive grooves with particle pull out and delamination, leading to accelerated wear rates. In addition, the present results show that Si particle size and the particle distribution plays a dictating role in tuning the hardness of the material and in turn the tribological properties.

The acidic corrosion tests of the Al-12Si as-prepared SLM samples show a two-stage corrosion behavior mechanism with increased corrosion rate for the initial three days. After three days the corrosion rate decreases because the access of the HNO_3 solution to the Al phase is restricted by the continuous Si skeleton. The weight-loss for the as-prepared Al-12Si SLM specimen is 5.72 ± 0.15 mg/cm^2 in 1 M HNO_3 solution after 14 days and it is similar to the corresponding Al-12Si cast sample. Even though both the cast and as-prepared SLM samples have different microstructure with different morphology of the Si phase, the

accesses of the HNO$_3$ solution to Al is restricted effectively by the Si phase, leading to similar corrosion rates. On the other hand, the corrosion rate of the SLM samples increases with increasing the annealing temperature. The SLM sample annealed to 723 K shows a weight-loss of 10.68 ± 0.26 mg/cm^2, which is twice the as-prepared specimen. This accelerated weight-loss is due to the presence of isolated Si particles to their removal from the surrounding Al matrix, indicating that the microstructure plays a key role in deciding the corrosion behavior of the SLM samples.

With the aim of increasing the application spectrum of the SLM parts, friction welding was used to join the Al-12Si SLM parts. Phase analysis reveals that the amount of free Si significantly increases in the SLM–weld zone compared with the base metal. This is accompanied by the increase of the crystallite size of the Al and Si phases. Microstructural investigations of the SLM–weld zone show a pronounced change in the dimension and shape of the cells when compared with the base metal: the columnar morphology characterizing the base metal is absent in the SLM–weld zone and the microstructure consists of small Si particles uniformly distributed in the Al matrix. Such a microstructure leads to a reduced hardness in the SLM–weld zone compared to the base metal. This is in contrast to the hardness profile of the corresponding friction welded cast material, which displays the typical behavior of friction welded Al-based alloys, where the hardness of the weld zone is significantly higher than the base metal.

The microstructural variations in the weld zone have also a remarkable effect on the mechanical properties of the materials. The tensile tests reveal that the yield strength of the welded SLM sample is ~ 215 MPa, which is ~ 45 MPa lower than in the as-SLM condition. However, the ductility increased from ~ 3% in the as-SLM condition to ~ 10% after friction welding. The cast samples display an opposite behavior: the friction welded cast sample shows higher yield strength (~ 50 MPa) than in the as-cast condition but reduced fracture strain (~ 2%) compared with the as-cast counterpart (~ 9.5%). These findings demonstrate that solid-state friction welding can be successfully used to join materials produced by SLM and helps to significantly improve their ductility. This offers the possibility to overcome the problem of the limited dimensions of the SLM parts in order to produce objects with no dimensional limitations.

The above results demonstrate the importance of the microstructure in deciding the mechanical, tribological and corrosion properties of the Al-12Si SLM material. Both the size and the distribution of the Si particles are very important and the properties of the samples can be tuned in a controlled way both in-situ (by varying the hatch style) and ex-situ (through annealing treatments). One can also consider changing the microstructure of the SLM samples in-situ by SLM processing at high temperatures. The knowledge gained from the present work can be effectively utilized to process other Al-alloys, including het-treatable alloys of immediate commercial interest like the 7xxx and 6xxx series. In addition, the controlled microstructure-property correlation of the SLM parts can be successfully used for the development of novel high-strength Al-based alloys for application in the aerospace and automotive sectors.

References

[Ali12a]   S.A. Alidokht, A. Abdollah-Zadeh, S. Soleymani, T. Saeid, H. Assadi, Evaluation of microstructure and wear behavior of friction stir processed cast aluminum alloy, Materials Characterization, 63 (2012) 90.

[Alu07a]   Aluminum Association, Improving sustainability in the transport sector through weight reduction and the application of aluminum, European Aluminium Association and International Aluminium Institute, (www.worldaluminium.org) (2007).

[Alu11a]   The aluminium automotive manual: Applications – power train, (http://www.alueurope.eu/wp-content/uploads/2011/11/AAM-Applications-Power-train-1-Pistons.pdf), European aluminium association (2011).

[Alu89a]   Aluminum alloys – contemporary research and applications, Academic Press Inc., London (1989).

[Ama12a]   K.N. Amato, S.M. Gaytan, L.E. Murr, E. Martinez, P.W. Shindo, J. Hernandez, S. Collins, F. Medina, Microstructures and mechanical behavior of Inconel 718 fabricated by selective laser melting, Acta Materialia, 60 (2012) 2229.

[Ana09a]   D. Ananthapadmanaban, V. Seshagiri Rao, N. Abraham, K. Prasad Rao, A study of mechanical properties of friction welded mild steel to stainless steel joints, Materials and Design, 30 (2009) 2642.

[Arc53a]   J.F. Archard, Contact and rubbing of flat surface, Journal of Applied Physics, 24 (1953) 981.

[Arm83a]   R.W. Armstrong, Yield, flow and fracture of polycrystals, Baker TN ed. Applied Science Publishers. London (1983).

[Ash01a]   M.F. Ashby, A.G. Evans, A.N. Fleck, L.J. Gibson, J.W. Hutchinson, H.N.G. Wadley, Metal Foams: A Design Guide; Butterworth-Heinemann: Boston, MA, USA (2001).

[ASM95a]   ASM Handbook, Properties and selection: nonferrous alloys and special-purpose materials, ASM International (1995).

[AST97a]   ASTM standards, ASTM D5706-97, Standard test method for determining extreme pressures properties of lubricating greases using a high-frequency, linear-oscillation test machine (1997).

[AST97b]   ASTM standards, ASTM D5707-97, Standard Test Method for Measuring Friction and Wear Properties of Lubricating Grease Using a High-Frequency, Linear-Oscillation (SRV) Test Machine (1997).

[AST10a]   ASTM standards, ASTM G99-05, Standard test method for wear testing with a pin-on-disc apparatus (2010).

[AST12a]   ASTM standards, ASTM F2792-12a, Standard terminology for additive manufacturing technologies (2012).

[Atk08a]   P. Atkins, L. Jones, Chemical properties: The quest for insight (4th ed.), W.H. Freeman and company (2008).

[Bar61a]   W. Bardsley, J.M. Callan, H.A. Chedzey, D.T.J. Hurle, Constitutional supercooling during crystal growth from stirred melts – II: Experimental: Gallium-doped Germanium, Solid-state electronics, 3 (1961) 142.

[Ben09a]   K.Y. Benyounis, O.M. Fakron, J.H. Abboud, Rapid solidification of M_2 high-speed steel by laser melting; Materials & Design, 30 (2009) 674.

[Bib05a]   R.J. Bibb, D. Eggbeer, Rapid manufacture of custom fitting surgical guides'. 6th National Conference on Rapid Design and Manufacture, Buckinghamshire (2005).

[Bib06a]   R.J. Bibb, D. Eggbeer, R. Williams, 'Rapid manufacture of removable partial denture frameworks, Rapid Prototyping Journal, 12 (2006) 95.

[Bir07a]   Y. Birol, Microstructural evolution during annealing of a rapidly solidified Al-12Si alloy, Journal of Alloys and Compounds, 439 (2007) 81.

[Boi01a]   K. Boivie, Limits of Loose Metal Powder Density in the Sinterstation, 12th Annual Solid Freeform Fabrication Symposium, 6-8 August, Austin, Texas, USA (2001).

[Bos73a]   S.K. Bose, R. Kumar, Structure of rapidly solidified aluminium-silicon alloys, Journal of Materials Science, 8 (1973) 1795.

[Bou02a]   D. Bourell, M. Wohlert, N. Harlan, S. Das, J. Beaman, Powder densification maps in selective laser melting, Advanced Engineering Materials, 4 (2002) 663.

[Bra12a]   E. Brandl, U. Heckenberger, V. Holzinger, D. Buchbinder, Investigation on the relationship between intermediate temperature embrittlement and intergranular precipitate in Ni(Bi) alloy, Materials & Design, 34 (2012) 159.

References

[Bri00a]   B.J. Briscoe, A. Chateauminois, T.C. Lindley, D. Parsonage, Contact damage of poly(methlymethacrylate) during complex microdisplacements, Wear, 240 (2000) 27.

[Bro05a]   W.K. Brooks, J. Todd, C.J. Sutcliffe, Automatic lattice geometry generation for rapid manufacture. 6th National Conference on Rapid Design and Manufacture, Buckinghamshire (2005).

[Caf10a]   http://caffeineabuse.blogspot.de/2010/05/rigging-piston-engine.html (2010)

[Cam10a]   S.L. Campanelli, N. Contuzzi, A. Angelastro, A.D. Ludovico, Capabilities and Performances of the Selective Laser Melting Process, New Trends in Technologies: Devices, Computer, Communication and Industrial Systems, Meng Joo Er (Ed.), ISBN: 978-953-307-212-8, InTech, DOI: 10.5772/10432. Available from: http://www.intechopen.com/books/new-trends-in-technologies--devices--computer--communication-and-industrial-systems/capabilities-and-performances-of-the-selective-laser-melting-process (2010).

[Che08a]   M. Chena, X. Meng-Burany, T.A. Perry, A.T. Alpas, Micromechanisms and mechanics of ultra-mild wear in Al-Si alloys, Acta Materialia, 56 (2008) 5605.

[Cho11a]   S-H. Choi, S-Y. Sung, H-J. Choi, Y-H. Sohn, B-S. Han, K-A. Lee, High Temperature Tensile Deformation Behavior of New Heat Resistant Aluminum Alloy, Materials Transactions, 52 (2011) 1661.

[Chl11a]   E. Chlebus, B. Kuźnicka, T. Kurzynowski, B. Dybała, Microstructure and mechanical behaviour of Ti—6Al—7Nb alloy produced by selective laser melting, Materials Characterization, 62 (2011) 488.

[Cla79a]   J. Clarke, A.D. Sarkar, Wear characteristics of as-cast binary aluminum silicon alloys, Wear, 54 (1979) 7.

[Col95a]   G.S. Cole, A.M. Sherman, Lightweight materials for automotive applications, Materials Characterization, 35 (1995) 3.

[Cro71a]   B. Crossland, Friction welding, Contemporary Physics, 12 (1971) 559.

[Dai13a]   D. Dai, D. Gu, Thermal behavior and densification mechanism during selective laser melting of copper matrix composites: Simulation and experiments, Materials and Design, In press, Accepted Manuscript (2013).

[Das89a]   S. Das, S.V. Prasad, T.R. Ramachandran, Microstructure and wear of cast (Al-Si alloy)-graphite composites, Wear, 133 (1989) 173.

References

[DGu09a]   D. Gu, Z. Wang, Y. Shen, Q. Li, Y. Li, In-situ TiC particle reinforced Ti–Al matrix composites: Powder preparation by mechanical alloying and Selective Laser Melting behavior, Applied Surface Science, 255 (2009) 9230.

[Dim05a]   D.E. Dimla, M. Camilotto, F. Miani, Design and optimisation of conformal cooling channels in injection moulding tools. Journal of Materials Processing Technology, 164 (2005) 1294.

[DOE12a]   Materials: Foundation for the Clean Energy Future: Energy, efficiency and renewable energy, U.S. Department of energy, http://energy.tms.org/docs/-pdfs/Materials_Foundation_for_Clean_Energy_Age_Press_Final.pdf (2012).

[Dot08a]   M. Dotcheva, H. Millward, D. Thomas, Investigation of Rapid Manufactured Cellular Structures for Injection Moulding Tools, Proceedings of 6th CIRP International Conference on Intelligent Computation in Manufacturing Engineering- CIRP ICME'08, Naples, Italy (2008) 369.

[Dot09a]   M. Dotcheva, D. Thomas, H. Millward, An evaluation of rapid manufactured cellular structures to enhance injection molding tool performance, International Journal of Materials Engineering and Technology, 1 (2009) 105.

[Dup13a]   Dupont industries, Vehicle weight reduction for optimal performance, http://www.dupont.com/industries/automotive/articles/lightweighting.html (2013).

[Dwi10a]   D.K. Dwivedi, Adhesive wear behavior of cast aluminum–silicon alloys: overview, Materials and Design, 31 (2010) 2517.

[Eji07a]   J.U. Ejiofor, R.G. Reddy, Developments in the processing and properties of particulate Al-Si composites, JOM, 49 (1997) 31.

[Ell02a]   K. Elleuch, S. Fouvry, Wear analysis of A357 aluminium alloy under fretting, Wear, 253 (2002) 662.

[Elm07a]   M. Elmadagli, T. Perry, A.T. Alpas, A parametric study of the relationship between microstructure and wear resistance of Al–Si alloys, Wear, 262 (2007) 79.

[Ema13a]   http://www.eos.info/additive_manufacturing (2013).

[ENE13a]   Building an American Economy to Last: American Competiveness in Manufacturing, http://energy.gov/articles/building-american-economy-last-american-competiveness-manufacturing (2013).

[Eva01a]   A.G. Evans, J.W. Hutchinson, N.A. Fleck, M.F. Ashby, H.N.G. Wadley, The topological design of multifunctional cellular metals, Progress in Materials Science, 46 (2001) 309.

[Fab11a]   http://www.ciri.org.nz/nzrma/technologies.html (2011).

[Far06a]   A.J. Farrell, B. Norton, D.M. Kennedy, Corrosive effects of salt hydrate phase change materials used with aluminium and copper, Journal of Materials Processing Technology, 175 (2006) 198.

[Fle13a]   G. Fletcher, Reducing weight in cars is a win-win for everyone, Postmedia News, http://driving.ca/auto-news/news/reducing-weight-in-cars-is-a-win-win-for-everyone-3/ (2013).

[Fle74a]   M.C. Flemings, Solidification processing, McGraw-Hill, New York (1974).

[Fra03a]   L.E. Fratila-Apachitei, J. Duszczyk, K. Katgerman, Vickers microhardness of AlSi(Cu) anodic oxide layers formed in H_2SO_4 at low temperature, Surface and Coatings Technology, 165 (2003) 309.

[Fre73a]   H. Fredriksson, M. Hillert, N. Lange, The modification of Aluminum-Silicon alloys by Sodium, Journal of The Institute of Metals, 101 (1973) 275.

[Fre06a]   H. Fredriksson, U. Åkerland, Materials Processing during Casting, John Wiley & Sons Ltd, West Sussex England (2006).

[Geb03a]   I.A. Gebhardt, Rapid Prototyping: Industrial Rapid Prototyping System: Prototyper: Solid Ground Curing – Cubital (2003).

[Ger84a]   R.M. German, Powder metallurgy science, Metal powder industries federation (1984).

[Ger89a]   R.M. German, Particle Packing Characteristics, Metal Powder Industry, Princeton, New Jersey (1989).

[Gia76a]   A.F. Giamei, H.E. Kraft, F.D. Lernkey, New trends in Materials Processing, ASM, Metalhhhhhs Park, OH (1976).

[Gor11a]   B. Gorny, T. Niendorf, J. Lackmann, M. Thoene, T. Troester, H.J. Maier, In situ characterization of the deformation and failure behavior of non-stochastic porous structures processed by selective laser melting, Materials Science and Engineering A, 528 (2011) 7962.

[Got04a]   H. Goto, K. Uchijo, Fretting wear of Al–Si alloy matrix composites, Wear, 256 (2004) 630.h

[Gro07a]   M.P. Groover, Theory of Metal Machining: Fundamentals of Modern Manufacturing (3rd ed.), John Wiley & Sons (2007).

[Gua09a]   Y.C. Guan, W. Zhou, Z.L. Li, H.Y. Zheng, Study on the solidification microstructure in AZ91D Mg alloy after laser surface melting, Applied Surface Sciences, 255 (2009) 8235.

[Hao13a]   L. Hao, D. Raymont, C. Yan, A. Hussein, P. Young, Design and Additive Manufacturing of Cellular Lattice Structures, College of Engineering, Mathematics and Physical Sciences, University of Exeter, Exeter EX4 4QF, Devon, United Kingdom (2013).

[Has87a]   A. Hasui, T. Matsui, On the effect of faying face condition on weldability in friction welding, Transactions of the Japan Welding Society, 18 (1987) 77.

[HHu74a]   H. Hu, Texture of metals, Texture, 1 (1974) 233.

[Hir04a]   J. Hirsch, Automotive trends in aluminium – the European perspective, Materials Forum, 28 (2004) 15.

[Hol14a]   N.J.H. Holroyd, G.M. Scamans, R.C. Newman, A.K. Vasudevan, Aluminum-Lithium Alloys: Processing, Properties and Applications – Chapter 14 – Corrosion and Stress Corrosion of Aluminum-Lithium Alloys (2014) 457.

[Hum13a]   G. Hummel, Development of a Lightweight Hydraulic Valve Manifold by Selective Laser Melting Technology Hydraulics System Engineer/Designated Certification Specialist, Airbus Operations GmbH (2013).

[Hut01a]   D.W. Hutmacher, T. Schantz, I. Zein, K.W. Ng, S.H. Teoh, K.C. Tan, Mechanical properties and cell cultural response of polycaprolactone scaffolds designed and fabricated via fused deposition modeling, Journal of Biomedical Materials Research, 55 (2001) 203.

[Ima13a]   Image J software - http://rsbweb.nih.gov/ij/

[Imm95a]   G.P. Immarigeon, R.T. Holt, A.K. Koul, L. Zhao, W. Wallace, J.C. Beddoes, Microstructural Characterization of Lightweight Structural Materials Transportation, Materials Characterization, 35 (1995) 41.

[Jac65a]   K.A. Jackson, J.D. Hunt, Transparent compounds that freeze like metals, Acta Meterialia, 13 (1965) 1212.

[Jac66a]   K.A. Jackson, J.D. Hunt, D.R. Uhlmann, T.P. Sewand III, On the origin of the equiaxed zone in castings, Transactions AMIE, 236 (1966) 149.

[Jac71a]   K.A. Jackson, Solidification, ASM, Metals Park, OH 1971.

[Jac92a]   P.F. Jacobs, Rapid prototyping & manufacturing, first edition, Society of manufacturing engineering, Dearborn, USA (1992).

[Jeo01a]   D.H. Jeong, F. Gonyalez, G. Palumbo, K.T. Aust, U. Erb, The effect of grain size on the wear properties of electrodeposited nanocrystalline nickel coatings, Scripta Materialia, 44 (2001) 493.

[Jeo03a]   D.H. Jeong, U. Erb, K.T. Aust, G. Palumbo, The relationship between hardness and abrasive wear resistance of electrodeposited nanocrystalline Ni-P coatings, Scripta Materialia, 48 (2003) 1067.

[JLi07a]   J.P. Li, C. Wilson, J.R. Wijn, C.A. Van Blitterswijk, K. De Groot, Fabrication of porous Ti6Al4V with designed structure by rapid prototyping technology, Key Engineering Materials, 330 (2007) 1293.

[JLi07b]   J.F. Li, Z.Q. Zheng, S.C. Li, W.J. Chen, W.D. Ren, X.S. Zhao, Simulation study on function mechanism of some precipitates in localized corrosion of Al alloys, Corrosion Science, 49 (2007) 2436.

[Jun13a]   W. Jun, Opportunities and applications of 3D additive manufacturing, http://www.simtech.astar.edu.sg/PECOI/media/3325/3D%20Additive%20Manu-facturing-PECOI-11%20Apr%202013-Printing.pdf (2013).

[Kam08a]   M. Kamiya, T. Yakou, T. Sasaki, Y. Nagatsuma, Effect of Si content on turning machinability of Al-Si binary alloy coatings, Materials Transactions, 49 (2008) 587.

[Kan12a]   J. Kang, F.C. Zhang, Deformation, fracture, and wear behaviors of C+N enhancing alloying austenitic steels, Materials Science and Engineering A, 558 (2012) 623.

[Kar98a]   N.P. Karapatis, J.P.S. Griethuysen, R. Glardon, Direct Rapid Tooling: A Review of Current Research, Rapid Prototyping Journal, 4 (1998) 77.

[Kat67a]   T.Z. Kattamis, U.T. Holmber, M.C. Flemings, Influence of coarsening on dendritic arm spacing and grain size of magnesium-zinc alloy, Journal of Institute of Metals, 55 (1967) 343.

[Kat94a]   K. Katoh, H. Tokisue, Properties of 6061 aluminium alloy friction welded joints, Welding International, 8 (1994) 863.

[Kem12a]   K. Kempen, L. Thijs, J.V. Humbeeck, J-P. Kruth, Mechanical Properties of AlSi10Mg Produced by Selective Laser Melting, Physics Procedia, 39 (2012) 439.

[Ken01a]   M. Kending, S. Jeaniaquet, R. Addison, J. Waldrop, Role of hexavalent chromium in the inhibition of corrosion of aluminum alloys, Surface and Coatings Technology, 140 (2001) 58.

[Kha10a]   M. Khan, Selective laser melting (SLM) of Gold (Au), PhD thesis, Loughborough University, Leicestershire, UK (2010).

[Kha10b]   H. Khalid Rafi, G.D. Janaki Ram, G. Phanikumar, K. Prasad Rao, Microstructure and tensile properties of friction welded aluminum alloy AA7075-T6, Materials and Design, 31 (2010) 2375.

[Kha10c]   K. Khaled, Electrochemical investigation and modeling of corrosion inhibition of aluminum in molar nitric acid using some sulphur-containing amines, Corrosion Science, 52 (2010) 2905.

[Khr74a]   M.M. Khruschov, Principles of abrasive wear, Wear, 28 (1974) 69.

[Kim05a]   M. Kimura, M. Kusaka, K. Seo, A. Fuji, Improving joint properties of friction welded joints of high tensile steel, Science and Technology of Welding and Joining, 10 (2005) 666.

[Kra12a]   D. Krätschmer, E. Roos, X. Schuler, K.-H. Herter, Proof of fatigue strength of nuclear components part II: Numerical fatigue analysis for transient stratification loading considering environmental effects, International Journal of Pressure Vessels and Piping, 92 (2012) 1.

[Kru05a]   J.P. Kruth, B. Vandenbroucke, J. Vaerenbergh, I. Naert, Rapid Manufacturing of Dental Prostheses by means of Selective Laser Sintering/Melting, in Proceedings of the AFPR, S4 (2005).

[Kru06a]   W. Kruf, B. Van de Vorst, H. Maalderink, N. Kamperman, Design for Rapid Manufacturing Functional SLS Parts, Proceedings of 5th CIRP International Conference on Intelligent Computation in Manufacturing Engineering- CIRP ICME'06, Ischia, Italy, (2006) 609.

[Kru08a]   J.P. Kruth, A.D. Ludovico, S.L. Campanelli, M. Rombouts, J. Van Vaerenbergh, Statistical optimization of selective laser melting of metal powders, Proceedings of 4th Intelligent Computation in Manufacturing Engineering, (2004) 643.

[Kum08a]   S. Kumar, M. Chakraborty, V. Subramanya Sarma, B.S. Murty, Tensile and wear behaviour of in situ Al–7Si/TiB$_2$ particulate composites, Wear, 265 (2008) 134.

References

[Lae00a]   J. Laeng, J.G. Stewart, F.W. Liou, Laser Metal Forming Processes for Rapid Prototyping - a review, International Journal of Production Research, 38 (2000) 3973.

[Lam06a]   Laminated Object Manufacturing, http://home.att.net/~castleisland/lom.htm (2006).

[Las10a]   H.R. Lashgari, S. Zangeneh, H. Shahmir, M. Saghafi, M. Emamy, Heat treatment effect on the microstructure, tensile properties and dry sliding wear behavior of A356–10%B4C cast composites, Materials and Design, 31 (2010) 4414.

[Law77a]   A. Lawley, Ovewview of powder atomization process and fundamentals, International Journal of Powder Metallurgy, 13 (1977) 169.

[Law78a]   A. Lawley, Preparation of metal powders, Annual Review of Materials Science, 8 (1978) 49.

[Lea99a]   A. Leatham, Spray Forming: Alloys, Products, and Markets, JOM, 51 (1999).

[Lee00a]   J.A. Lee, P.S. Chen, Aluminium - silicon alloy having improved properties at elevated temperatures and articles cast therefrom, US Patent No. 6399020.

[Lip10a]   J.I. Lipton, D. Arnold, F. Nigl, N. Lopez, D.L. Cohen, N. Noren, H. Lipson, Multi-Material Food Printing with Complex Internal Structure Suitable for Conventional Post-Processing, 21st Solid Freeform Fabrication Symposium (SFF'10), Austin, Texas, USA (2010).

[Liu91a]   Y. Liu, R. Asthana, P.A. Rohatgi, Map for wear mechanisms in aluminium alloys, Journal of Materials Science, 26 (1991) 99.

[LLu01a]   L. Lu, J. Fuh, Y.S. Wong, Laser-Induced Materials and Processes for Rapid Prototyping, Kluwer Academic Publishers, Boston, USA (2001).

[Löb11a]   L. Löber, D. Klemm, U. Kühn, J. Eckert, Rapid manufacturing of cellular structures of steel or titaniumaluminide, Materials Science Forum, 690 (2011) 103.

[Maa07a]   M. Maalekian, Friction welding – critical assessment of literature, Science and Technology of Welding and Joining, 12 (2007) 738.

[Maa08a]   M. Maalekian, E. Kozeschnik, H.P. Brantner, H. Cerjak, Comparative analysis of heat generation in friction welding of steel bars, Acta Materialia, 56 (2008) 2843.

[Mac96a]   C. Machover, the CAD/CAM Handbook, Beverly Beckert. McGraw-Hill Companies (1996).

[Mak12a]   A.V. Makarov, N.A. Pozdejeva, R.A. Savrai, A.S. Yurovskikh, I.Y. Malygina, Improvement of wear resistance of quenched structural steel by nanostructuring frictional treatment, Journal of Friction and Wear, 33 (2012) 433.

[Mal04a]   E. Malone, K. Rasa, D. Cohen, T. Isaacson, H. Lashley, H. Lipson, Freeform fabrication of zinc-air batteries and electrochemical assemblies, Rapid prototyping journal, 10 (2004) 58.

[Man07a]   A. Mandal, M. Chakraborty, B.S. Murty, Effect of TiB_2 particles on sliding wear behaviour of Al–4Cu alloy, Wear, 262 (2007) 160.

[Mar07a]   T.A. Markley, M. Forsyth, A.E. Hughes, Corrosion protection of AA2024-T3 using rare earth diphenyl phosphates, Electrochemica Acta, 52 (2007) 4024.

[Mar11a]   J.A.R. Marquez, C.M.B. Rodriguez, C.M. Herrera, E.R. Rosas, O.Z. Angel, O.T. Pozos, Effect of Surface Morphology of ZnO Electrodeposited on Photocatalytic Oxidation of Methylene Blue Dye. Part I: Analytical Study, International Journal of Electrochemical Science, 6 (2011) 4059.

[Maz00a]   J. Mazumder, D. Dutta, N. Kikuchi, A. Ghosh, Closed Loop Direct Metal Deposition: Art to Part, Optics and Lasers in Engineering, 34 (2000) 397.

[Mid96a]   C.J. Middleton, R. Timmins, R.D. Townsend, The integrity of materials in high temperature components; Performance and life assessment, International Journal of Pressure Vessels and Piping, 66 (1996) 33.

[Mil00a]   W.S. Miller, L. Zhuang, J. Bottema, A.J. Wittebrood, P. De Smet, A. Haszler, A. Vieregge, Recent development in aluminium alloys for the automotive industry, Materials Science and Engineering A, 280 (2000) 37.

[Mil98a]   Military Handbook, Metallic materials and elements for aerospace vehicle structures, Knovel Interactive Edition, U.S. Department of Defense, USA (1998).

[Moo74a]   M.A. Moore, The relationship between the abrasive wear resistance, hardness and microstructure of ferritic materials, Wear, 28 (1974) 59.

[Mor69a]   L.R. Morris, W.C. Winegard, The development of cells during the solidification of a dilute Pb-Sb alloy, Journal of Crystal Growth, 5 (1969) 361.

[Muk06a]   N.K. Mukhopadhyay, P. Paufler, Micro- and nanoindentation techniques for mechanical characterization of Materials, International Materials Reviews, 51 (2006) 209.

[Mul09a]   L. Mullen, R. Stamp, W. Brooks, E. Jones, C. Sutcliffe, Selective laser melting: A regular unit cell approach for the manufacture of porous, titanium, bone in-growth constructs, suitable for orthopedic applications, Journal of Biomedical Materials Research, 89b (2009) 325.

[Mul63a]   W.W. Mullins, R.F. Sekerka, Morphological stability of a particle growing by diffusion or heat flow, Journal of Applied Physics, 34 (1963) 323.

[Mum08a]   K.A. Mumtaz, P. Erasenthiran, N. Hopkinson, High density selective laser melting of Waspaloy, Journal of Materials Processing Technology, 195 (2008) 77.

[Mur84a]   J.L. Murry, A.J. McAlister, The Al-Si (Aluminum – Silicon) system, Bulletin of Alloy Phase Diagrams, 5 (1984) 74.

[Mus11a]   A.Y. Musa, A.B. Mohamad, A.A.H. Khadum, E.P. Chee, Galvanic corrosion of Aluminum Alloy (Al2024) and Copper in 1.0 M Nitric Acid, International Journal of Elevtrochemical Science, 6 (2011) 5052.

[Nan06a]   S. Nanthan, Structural change, Design Engineering (2006).

[New11a]   http://www.ciri.org.nz/nzrma/technologies.html (2011).

[Nie10a]   J-F. Nie, A. Morton, Improving the microstructures and mechanical properties of hypereutectic Al-Si alloys by spray forming technique, Materials Science forum, 654 (2010) 1416.

[Niu99a]   H.J. Niu, I.T.H. Chang, Selective Laser Sintering of Gas and Water Atomized High Speed Steel Powders, Scripta Materialia, 41 (1999) 25.

[Noo06a]   R.I. Noorani, Rapid prototyping: Principles and applications, John Wiley & Sons Inc. 0471730017, New Jersey, USA (2006).

[NYT12a]   A detail from a project to produce lighter, high-strength cars, NYTCREDIT: Steel market development institute, The New York Times, (2012).

[Pat09a]   H.W. Patrick, D. Timothy, Rapid prototyping: porous titanium alloy scaffoldsproduced by selective laser melting for bone tissue engineering, Tissue Engineering: Part C Methods 15 (2009) 115.

[Pat11a]   D.K. Pattanayak, A. Fukuda, T. Matsushita, M. Takemoto, S. Fujibayashi, K. Sasaki , N. Nishida, T. Nakamura, T. Kokubo, Bioactive Ti metal analogous

to human cancellous bone: Fabrication by selective laser melting and chemical treatments, Acta Biomaterialia 7 (2011) 1398.

[Pla60a]   T.S. Plaskett, W.C. Winegard, Cell to dendrite transition in tin base alloys, Canadian Journal of Physiology, 38 (1960) 1077.

[Pol95a]   I.J. Polmear, Light alloys metallurgy of light metals, Arnold: a division of Hooder Headlines PLC, London (1995).

[Pou96a]   M. Pourbaix, Atlas of electrochemical equilibria in aqueous solutions, Pargamon Press, Brussels (1996).

[Pow13a]   Power trains, A Motor magazine newsletter, http://www.motor.com-/newsletters/20130715/WebFiles/ID2_ChoicesMatter.html (2013).

[Pra11a]   K.G. Prashanth, S. Kumar, S. Scudino, B.S. Murty, J. Eckert, Fabrication and response of Al70Y16Ni10Co4 glass reinforced metal matrix composites, Materials and manufacturing processes, 26 (2011) 1242.

[Pra13a]   K.G. Prashanth, S. Scudino, H.J. Klauss, K.B. Surreddi, L. Loeber, Z. Wang, A.K. Chaubey, U. Kühn, J. Eckert, Microstructure and mechanical properties of Al-12Si produced by selective laser melting: Effect of heat treatment, Materials Science and Engineering A, 590 (2014) 153.

[Pra87a]   B.N. Pramila Bai, S.K. Biswas, Mechanism of wear in dry sliding of a hypoeutectic aluminum alloy, Lubrication Engineering, 43 (1987) 57.

[Pra98a]   B.K. Prasad, K. Venkateswarlu, O.P. Modi, A.K. Jha, S. Das, R. Dasgupta, A.H. Yegneswaran, Sliding wear behavior of some Al–Si alloys: role of shape and size of Si particles and test conditions, Metallurgical and Materials Transactions A, 29A (1998) 2747.

[Rab65a]   E. Rabinowicz, Friction and Wear of Materials, John Wiley and Sons, New York (1965).

[Rag13a]   N. Raghukiran, Ravi Kumar, Processing and dry sliding wear performance of spray deposited hyper-eutectic aluminum-silicon alloys, Journal of Materials and Processing Technology, 213 (2013) 401.

[Rag98a]   V. Raghavan, Physical metallurgy: Principles and practice, Prentice Hall of India Private Limited, New Delhi, India (1998).

[Reh06a]   O. Rehme, C. Emmelmenn, Rapid manufacturing lattice structures with selective laser melting,. Laser-based Micropackaging. San Jose, CA, USA (2006).

[Rie69a]   H.M. Rietveld, A profile refinement method for nuclear and magnetic structures, Journal of Applied Crystallography, 2 (1969) 65.

[RLi12a]   R. Li, Y. Shi, L. Wang, J. Liu, Y. Wang, The key metallurgical features of selective laser melting of stainless steel powder for building metallic part, Powder Metallurgy and Metal Ceramics, 50 (2012) 141.

[Rob12a]   I.A. Roberts, Investigation of residual stresses in the laser melting of metal powders in additive layer manufacturing, PhD thesis submitted to University of Wolverhampton (2012).

[Roi01a]   T. Roisnel, J. Rodriguez-Carvajal, WinPLOTR: A Windows tool for powder diffraction pattern analysis, Materials Science Forum, 378 (2001) 118.

[Rom06a]   M. Rombouts, Selective laser sintering / melting of iron based powders, PhD Thesis, Katholieke University Leuven, Belgium (2006).

[Roo90a]   L.E. Rooy, Introduction to aluminum and aluminum alloys, In: Properties and selection: nonferrous alloys and special-purpose materials, ASM International, (1990).

[Rot13a]   F. Rotundo, A. Marconi, A. Morri, A. Ceschini, Dissimilar linear friction welding between SiC particle reinforced aluminum composite and a monolithic aluminum alloy: Microstructural , tensile and fatigue properties, Materials Science and Engineering A, 559 (2013) 852.

[Roy08a]   S. Roy, B. Basu, Mechanical and Tribological characterization of human tooth, Materials Characterization, 59 (2008) 747.

[Ruf09a]   M. Ruffo, RM and the Medical World (M. Excell, Ed.) MWP, 153 (2009) 40.

[Rut53a]   J.W. Rutter, B. Chalmer, A prismatic substructure formed during solidification metals, Canadian Journal of Physiology, 31 (1953) 15.

[Sac00a]   E. Sachs, E. Wylonis, S. Allens, M. Cima, H. Guo, Production of Injection Moulding Tooling with Conformal Cooling Channels Using the Three Dimensional Printing Process, Polymer Engineering and Science, 40, (2000) 1232.

[Sae07a]   M. Saeid, F. Saeid, Effect of material structure machining characteristics of hypereutectic Al-Si alloy, Master's thesis, Faculty of Mechanical Engineering, University of Technology, Malaysia (2007).

[Sah12a]   M. Sahin, C. Misirli, Aluminium Alloys - New Trends in Fabrication and Applications, http://dx.doi.org/10.5772/51130.

[Sal13a]   E. Sallica-Leva, A.L. Jardini, J.B. Fogagnolo, Microstructure and mechanical behavior of porous Ti–6Al–4V parts obtained by selective laser melting, Journal of the Mechanical Behavior of Biomedical Materials, 26 (2013) 98.

[San06a]   E.C. Santos, M. Shiomi, K. Osaka, T. Laoui, Rapid manufacturing of metal components by laser forming, International Journal of Machine Tools and Manufacture, 46 (2006) 1459.

[Sch01a]   N. Schlorke-de Boer, Metallische Massivgläser auf Fe-Al-P-C-B-(Ga-) Basis und Verbundmaterialien mit Mg-Y-Cu-Glas-Matrix, Ph.D. Thesis, Technische Universität Dresden, Dresden, Germany (2001).

[Sch42a]   E. Scheil, Bemerkungen zur Schichtkristallbildung (Retrograde saturation curves), Zeitschrift fur Metallkunde, 34 (1942) 70.

[Scu09a]   S. Scudino, G. Liu, M. Sakaliyska, K.B. Surreddi, J. Eckert, Powder metallurgy of Al-based metal matrix composites reinforced with β-Al_3Mg_2 intermetallic particles: Analysis and modeling of mechanical properties, Acta Materialia, 57 (2009) 4529.

[Sea99a]   J.W. Sears, Direct Laser Powder Deposition - 'State of the Art'. ASTM/TMS Materials Week, Cincinnati, Ohio, US (1999).

[Sek65a]   R.F. Sekerka, A stability function for explicit evaluation of the mullins-sekerka interface stability criterion, Journal of Applied Physics, 36 (1965) 264.

[Sek67a]   R.F. Sekerka, Application of the time-dependent theory of interface stability to an isothermal phase transformation, Journal of the Physics and Chemical of Solids, 28 (1967) 983.

[Ser06a]   T. Sercombe, N. Jones, R. Day, A. Kop, Heat treatment of Ti-6AI-7Nb components produced by selective laser melting, Rapid Prototyping Journal, 14 (2008) 300.

[She79a]   J.S. Sheasby, Powder Metallurgy of Iron-Aluminum, International Journal of Powder Metallurgy and Powder Technology, 15 (1979) 301.

[Shi00a]   T. Shinoda, Y. Mizuno, J. Li, T. Saito, Friction welding phenomena of aluminium, Welding International, 14 (2000) 425.

[Shi04a]   M. Shiomi, K. Osakada, K. Nakamura, T. Yamashita, F. Abe, Residual Stress within Metallic Model Made by Selective Laser Melting, CIRP Annals - Manufacturing Technology, 53 (2004) 195.

[Shi09a]   I. Shishkovsky, Y. Morozov, I. Smurov, Nanostructural self-organization under selective laser sintering of exothermic powder mixtures, Applied Surface Science, 255 (2009) 5565.

[Shi10a]   H-S. Shin, J-S. Park, Y. Yokoyama, Dissimilar friction welding of tubular Zr-based bulk metallic glasses, Journal of Alloys and Compound, 504 (2010) S275.

[Shi12a]   I. Shishkovsky, I. Yadroitsev, I. Smurov, Direct Selective Laser Melting of Nitinol Powder, Physics Procedia 39 (2012) 447.

[Sie09a]   http://code80.net/afpr/content/association/commissions/normalisation/-SIEMENS-_normalisation_08-09-09.pdf, Siemens (2009).

[Sim04a]   A. Simchi, The Role of Particle Size on the Laser Sintering of Iron Powder, Metallurgical and Materials Transactions B, 35 (2004) 937.

[Sin03a]   S. Kou, Welding Metallurgy, Second Edition, Wiley Interscience, New Jersey (2003).

[SJi12a]   S-D. Ji, J-G. Liu, Y-M. Yue, Z. Lu, L. Fu, 3D numerical analysis of material flow behavior and flash formation of 45th steel in continuous drive friction welding, Transactions of Nonferrous Metals Society of China, 22 (2012) S528.

[SLM13a]   http://www.slm-kunststofftechnik.de/?page_id=4&lang=en (2013).

[Son09a]   H.W. Song, S.R. Guo, Z.Q. Hu, A coherent polycrystal model for the inverse Hall-Petch relation in nanocrystalline materials, Nanostructured Materials, 11 (2009) 203.

[Son13a]   G-L. Song, M. Liu, Corrosion and electrochemical evaluation of an Al-Si-Cu aluminum alloy in ethanol solutions, Corrosion Science, 72 (2013) 73.

[Sou11a]   N. Soumyajit, K.V.N.B Anand Karthik, Synthesis of Al-Si alloys and study of their mechanical properties, BTech thesis, Department of Metallurgical and Materials Engineering, National Institute of Technology, Rourkela, India (2011).

[Sri01a]   V.C. Srivastava, R.K. Mandal, S.N. Ojha, Microstructure and mechanical properties of Al-Si alloys produced by spray forming process, Materials Science and Engineering: A, 304 (2001) 555.

[Sri09a]   V.C. Srivastava, G.B. Rudrakshi, V. Uhlenwinkel, S.N. Ojha, Wear characteristics of spray formed Al–alloys and their composites, Journal of Materials Science, 44 (2009) 2288.

[Str13a]   H. Strauß, AM envelope, the potential of additive manufacturing for façade construction, PhD thesis, Delft University of Technology, Delft, Netherlands (2007).

[Suá06a]   B. Suárez-Peña, J. Asensio-Lozano, Microstructure and mechanical property developments in Al-12Si gravity die-castings after Ti and/or Sr additions, Materials Characterization, 57 (2006) 218.

[Sub92a]   C. Subramanian, Some considerations towards the design of a wear resistant aluminium alloy, Wear, 155 (1992) 193.

[Suh73a]   N.P. Suh, The delamination theory of wear, Wear, 25 (1973) 111.

[Sun13a]   J. Sun, Y. Yang, D. Wang, Parametric optimization of selective laser melting for forming Ti6Al4V samples by Taguchi method, Optics & Laser Technology, 49 (2013) 118.

[Sur01a]   C. Suryanarayana, Mechanical alloying and milling, Progress in Materials Science, 46 (2001) 1.

[Suw08a]   S. Suwas, N.P. Gurao, Crystallographic texture in materials, Journal of Indian Institute of Science, 88 (2008) 151.

[Syv00a]   T. Syvanen, J. Nyrhila, J. Kotila, J.E. Lind, Direct Metal Laser Sintering of Very Fine Metal Powder, In proceedings of 19th International Congress on Applications of Lasers and Electro-Optics (ICALEO), 2-5 October, Dearborn, Vol. 89, Michigan, USA (2000).

[Tak13a]   A. Takaichi, Suyalatu, T. Nakamoto, N. Joko, N. Nomura, Y. Tsutsumi, S. Migita, H. Doi, S. Kurosu, A. Chiba, N. Wakabayashi, Y. Igarashi, T. Hanawa, Microstructures and mechanical properties of Co−29Cr−6Mo alloy fabricated by selective laser melting process for dental applications, Journal of the Mechanical Behavior of Biomedical Materials, 21 (2013) 67.

[Tha01a]   S.K. Thakur, B.K. Dhindaw, The influence of interfacial characteristics between SiC_p and Mg/Al metal matrix on wear, coefficient of friction and microhardness, Wear, 247 (2001) 191.

[Thi10a]   L. Thijs, Frederik Verhaeghe, T. Craeghs, J.V. Humbeeck, J-P Kruth, A study of the microstructural evolution during selective laser melting of Ti–6Al–4V, Acta Materialia, 58 (2010) 3303.

[Thi13a]   L. Thijs, K. Kempen, J-P. Kruth, J.V. Humbeeck, Fine-structured aluminium products with controllable texture by selective laser melting of pre-alloyed AlSi10Mg powder, Acta Materialia, 61 (2013) 1809.

[Til53a]   W.A. Tilled, K.A. Jackson, J.W. Rutter, B. Chalmer, The redistribution of solute atoms during the solidification of metals, Acta Matellurgica, 1 (1953) 428.

[Tim99a]   G. Timmermans, L. Froyen, Fretting wear behaviour of hypereutectic P/M Al–Si in oil environment, Wear. 230 (1999) 105.

[Tho06a]   L. Thorsson, Laser Sintering of Gold Jewellery, Proceeding of 1st International Conference on Rapid Manufacturing, 5-6 July, Loughborough, UK (2006).

[Tip08a]   P.A. Tipler, G. Mosca, Physics for Scientists and Engineers (6th ed.), Worth Publishers, New York, NY (2008).

[Tob13a]   B. Tobin, Part 1II: Conformal cooling of mold cavities – where it works and where it dosen't, Plastics today, Modern Plastics and Injection Molding, (2013).

[Tod92a]   P. Todeschini, G. Champier, F.H. Samuel, Production of Al-(12-25) wt% Si alloys by rapid solidification: melt spinning versus centrifugal atomization, Journal of Materials Science, 27 (1992) 3539.

[Tol02a]   N. Tolochko, V. Savich, T. Laoui, L. Froyen, G. Onofrio, E. Signorelli, V.I. Titov, Dental Root Implants produced by the combined selective laser sintering/ melting of titanium powders'. Proceedings of the institute of Mechanical Engineers; Design and Applications. 216 (2002).

[Tor94a]   H. Torabian, J.P. Pathak, S.N. Tiwari, Wear characteristics of Al–Si alloys, Wear, 172 (1994) 49.

[Tso95a]   S. Tsopanos, C.J. Sutcliffe, I. Owen, The Manufacture of Cross-Flow Heat Exchangers by Selective Laser Melting: Enhanced, Compact and Ultra-Compact Heat Exchangers, Science and Technology, Hoboken, NJ, USA, Engineering Conferences International (2005).

[Und85a]   E.E. Underwood, Metals Handbook, ASM International, vol. 34, Metals Park, OH (1995).

[Uzu01a]   O. Uzun, T. Karaaslan, M. Keskin, Production and structure of rapidly solidified Al-Si alloys, Turkish Journal of Physics, 25 (2001) 455.

[Van04a]   G.F. Vander Voort, Metallography and Microstructures, ASM Handbook Volume 9, ASM International Materials Part, OH (2004).

[Van07a]   M. Van Elsen, Complexity of Selective Laser Melting: A New Optimisation Approach, PhD thesis, Katholieke Universiteit Leuven, Belgium (2007).

[Van07b]   B. Vandenbroucke, J-P. Kruth, Selective laser melting of biocompatible metals for rapid manufacturing of medical parts, Rapid prototyping journal, 13 (2007) 196.

[Van67a]   K.R. Van Horn, Aluminum: Vol I: Properties, physical metallurgy and phase diagrams, ASM International (1967).

[Ven04a]   T. Venugopal, K. Srinivasa Rao, K. Prasad Rao, Studies on friction stir welded AA 7075 aluminum alloy, Transactions Indian Institute of Metals, 57 (2004) 659.

[Vil12a]   T. Vilaro, C. Colin, J.D. Bartout, L. Naze, M. Sennour, Microstructural and mechanical approaches of the selective laser melting process applied to a nickel-base superalloy, Materials Science and Engineering A, 534 (2012) 446.

[Vra12a]   B. Vrancken, L. Thijs, J-P. Kruth, J.V. Humbeeck, Heat treatment of Ti6Al4V produced by Selective Laser Melting: Microstructure and mechanical properties, Journal of Alloys and Compound, 541 (2012) 177-185.

[Wan00a]   W. Wang, X. Bian, J. Qin, Study on atomic density changes in the liquid Al-Si alloys by X-ray diffraction method, Journal of Materials Science Letters, 19 (2000) 1583.

[Wan00b]   W. Wang, X. Bian, J. Qin, S.I. Syliusarenko, The atomic-structure changes in Al-16 pct Si alloy above the liquids, Metallurgical and Materials Transactions A, 31A (2000) 2163.

[Wan10a]   Y. Wang, Y. Shen, Z. Wang, J. Yang, N. Liu, W. Huang, Development of highly porous titanium scaffolds by selective laser melting, Materials Letters, 64 (2010) 674.

[Wan13a]   D. Wang, Y. Yang, R. Liu, D. Xiao, J. Sun, Study on the designing rules and processability of porous structure based on selective laser melting (SLM), Journal of Materials Processing Technology, 213 (2013) 1734.

[War09a]   P.H. Warnke, T. Douglas, P. Wollny, E. Sherry, M. Steiner, S. Galonska, S.T. Becker, I.N. Springer, J. Wiltfang, S. Sivananthan, Rapid prototyping: porous titanium alloy scaffolds produced by selective laser melting for bone tissue engineering, Tissue Eng Part C, 15 (2009) 115.

[WLi08a]   W.Y. Li, T.J. Ma, S.W. Yang, Q.Z. Xu, Y. Zhang, J.L. Li, H.L. Liao, Effect of friction time on flash shape and axial shortening of linear friction welded 45 steel, Materials Letters, 62 (2008) 293.

[WLi12a]   L. Wang, Q.S. Wei, P.J. Xue, Y.S. Shi, Fabricate Mould Insert with Conformal Cooling Channel Using Selective Laser Melting, Advanced Materials Research, 502 (2012) 67.

[Woh09a]   Wohlers report; State of the industry. Fort Collins, Wohlers associates (2009).

[Woh10a]   T. Wohlers, Additive Manufacturing: Part IV, Time compression (2010).

[Won07a]   M. Wong, S. Tsopanos, C. Sutcliffe, I. Owen, Selective laser melting of heat transfer devices, Rapid Prototyping Journal, 13 (2007) 291.

[Woo09a]   D. Wood, Additive layer manufacturing at Airbus – reality check or view into the future?, The TXT Magazine, 17 (2009) 23.

[Wri06a]   C.S. Wright, M. Youseffi, S.P. Akhtar, T.H.C. Childs, C. Hauser, P. Fox, J. Xie, Selective laser melting of prealloyed high alloy steel powder beds, Materials Science Forum, 514 (2006) 516.

[Xia12a]   N. Xiang, X-Z. Xin, J. Chen, B. Wei, Metal‑ceramic bond strength of Co‑Cr alloy fabricated by selective laser melting, Journal of Dentistry, 40 (2012) 453.

[Xin12b]   X.Z. Xin, N. Xiang, J. Chen, B. Wei, In vitro biocompatibility of Co‑Cr alloy fabricated by selective laser melting or traditional casting techniques, Materials Letters, 88 (2012) 101.

[XSu12a]   X. Su, Y. Yang, Research on track overlapping during Selective Laser Melting of powders, Journal of Materials Processing Technology, 212 (2012) 2074.

[XXu01a]   X. Xu, E. Sachs, S. Allen, The design of conformal cooling channels in injection molding tooling, Polymer Engineering and Science, 41 (2001) 1265.

[Yad09a]   I. Yadroitsev, I. Shishkovsky, P. Bertrand, I. Smurov, Manufacturing of fine-structured 3D porous filter elements by selective laser melting, Applied Surface Science, 255 (2009) 5523.

[Yad10a]   I. Yadroitsev, A. Gusarov, I. Yadroitsava, I. Smurov, Single track formation in selective laser melting of metal powders, Journal of Materials Processing Technology, 210 (2010) 1624.

[Yad11a]   I. Yadroitsev, I. Smurov, Surface morphology in Selective Laser Melting of Metal Powders, Physics Procedia, 12 (2011) 264.

[Yas11a]   E. Yasa, J-P. Kruth, Application of laser re-melting on selective laser melting parts, Advances in Production Engineering and Management, 6 (2011) 259.

[Yil95a]   B.S. Yilba, A.Z. Sahin, N. Kahraman, A.Z. Al-Garni, Friction welding of Steel-Al and Al-Cu materials, Journal of Materials Processing and Technology, 49 (1995) 431.

[Yil95b]   B.S. Yilba, A.Z. Sahin, A. Coban, B.J. Abdul Aleem, Investigation into the properties of friction-welded aluminum bars, Journal of Materials Processing Technology, 54 (1995) 76.

[Yoo11a]   Y. Yoon, I. Etsion, F.E. Talke, The evolution of fretting wear in a micro-spherical contact , Wear, 270 (2011) 567.

[Zha11a]   L.C. Zhang, D. Klemm, J. Eckert, Y.L. Hao, T.B. Sercombe, Manufacture by selective laser melting and mechanical behavior of a biomedical Ti–24Nb–4Zr–8Sn alloy, Scripta Materialia, 65 (2011) 21.

[Zha13a]   B. Zhang, J. Chen, C. Coddet , Microstructure and Transformation Behavior of in-situ Shape Memory Alloys by Selective Laser Melting Ti–Ni Mixed Powder, Journal of Materials Science & Technology, 29 (2013) 863.

[Zha97a]   J. Zhang, A.T. Alpas, Transition between mild and severe wear in aluminium alloys, Acta Materialia, 45 (1997) 513.

[Zhu07a]   H.H. Zhu, J.Y.H. Fuh, L. Lu, The Influence of Powder Apparent Density on the Density in Direct Laser-Sintered Metallic Parts, International Journal of Machine Tools and Manufacture, 47 (2007) 294.

[Zhu11a]   M.H. Zhu, Z.R. Zhou, On the mechanisms of various fretting wear modes, Tribology International, 44 (2011) 1378.

Acknowledgements

"The years of anxious searching in the dark, with their intense longing, their alternations of confidence and exhaustion and the final emergence into the light - only those who have experienced it can understand it." – Albert Einstein

As rightly quoted by the illustrious scientist Albert Einstein, PhD tenure has always been an adventure and a committed endeavor with a varied feeling of exhilaration, determination and sometimes exhausting. The transformation of the quest to ecstasy needs an amicable ambiance, encouragement, guidance, support and patience without which, I would not have been able to accomplish the doctoral dissertation.

First and foremost, it is my duty and great privilege to express my sincere thanks to Prof. J. Eckert providing me an opportunity to be a part of his research group at IFW Dresden, where I was and am exposed with the world-class facilities and surrounded by brilliant and dynamic people. I also express my gratitude for encouraging me to present my work at several national and international conferences and to work up my thesis in an accelerated pace.

I also feel utterly privileged in working with Dr. S. Scudino with his valuable suggestions, interests and his contribution in shaping up the present dissertation. His zeal, enthusiasm, creativeness have been a continuous source of inspiration throughout this exquisite journey.

My sincere thanks for the support, encouragement, help and for the nice time during the course of this thesis to Z. Wang, A.K. Chaubey, Prof. N.K. Mukhopadhyay, Dr. G.K. Rane, Dr. U. Kuehn, Dr. A. Gebert, Dr. M. Sakaliyska, L. Loeber, Dr. F.P. Gostin, H.J. Klauss, J.Y. Kim, Dr. H. Wendrock, Dr. T. Gemming, Dr. M. Stoica, Dr. D. Beitenschmidt, K. Zhuravleva, M.S. Khoshkhoo, Dr. S.M. Gorantala, Dr. W. Gruner, Dr. V. Hoffmann, A. Omar, R. Ummethala, P. Ma, Y.D. Jia, H.S. Sahabi, K. Kosiba, K. Song, B. Bartusch, H.

Versicherung

Hiermit versichere ich, daß ich die vorliegende Arbeit ohne unzulässige Hilfe Dritter und ohne Benutzung anderer als der angegeben Hilfsmittel angefertigt habe; die aus fremden Quellen direkt oder indirekt übernommenen Gedanken sind als solche kenntlich gemacht. Die Arbeit wurde bisher weder im Inland noch im Ausland in gleicher oder ähnlicher Form einer anderen Prüfungsbehörde vorgelegt.

Erklärung

Die vorliegende Arbeit wurde in Zeitraum April 2011 bis November 2013 am Institut für Metallische Werkstoffe des Institut für Festkörper- und Werkstoffforschung (IFW) Dresden unter der wissenschaftlichen Betreuung von Herrn Prof. Dr. Jürgen Eckert angefertigt.

Es haben zuvor keine erfolglosen Promotionsversuche stattgefunden.

Hiermit erkläre ich, daß ich die bestehende Prüfungsordnung der Fakultät Maschinenwesen TU Dresden (Fachrichtung Werkstoffwissenschaft) vom 1. Juli 2001 anerkenne.

Prashanth Konda Gokuldoss   Dresden, 21.11.2013